



INTEGRATED GPS/INS PRECISION
APPROACH LANDING WITH
M³AE INTERFERENCE AVOIDANCE

THESIS

Stephan H. Chastain
Captain, United States Air Force

AFIT/GE/ENG/99M-03

DEPARTMENT OF THE AIR FORCE
AIR UNIVERSITY
AIR FORCE INSTITUTE OF TECHNOLOGY

Wright-Patterson Air Force Base, Ohio

INTEGRATED GPS/INS PRECISION
APPROACH LANDING WITH
M³AE INTERFERENCE AVOIDANCE

THESIS

Stephan H. Chastain
Captain, United States Air Force

AFIT/GE/ENG/99M-03

Approved for public release; distribution unlimited

19990413 075

~~2008T70006T~~

The views expressed in this thesis are those of the author and do not reflect the official policy or position of the Department of Defense or the U. S. Government.

INTEGRATED GPS/INS PRECISION APPROACH LANDING
WITH M³AE INTERFERENCE AVOIDANCE

THESIS

Presented to the Faculty of the Graduate School of Engineering
of the Air Force Institute of Technology

In Partial Fulfillment of the
Requirements for the Degree of
Master of Science in Electrical Engineering

Stephan H. Chastain, B.S.E.E.

Captain, United States Air Force

March, 1999

Approved for public release; distribution unlimited

INTEGRATED GPS/INS PRECISION APPROACH LANDING
WITH M³AE INTERFERENCE AVOIDANCE

Stephan H. Chastain, B.S.E.E
Captain, United States Air Force

Approved:

Mikel M. Miller
Major Mikel M. Miller
Assistant Professor, Committee Chair

12 Mar 99
Date

Peter S. Maybeck
Dr. Peter S. Maybeck
Professor, Committee Member

12 Mar 99
Date

Preface

This work is builds upon the research efforts of many previous theses, primarily those of James L. Hirning, Cpt William J. Negast, Robert A. Gray, Cpt Ryan L. Britton, 2Lt Nathan A. White, and Maj Mikel M. Miller. Thanks goes to them for providing the solid foundation of the ideas expressed within. This work would not have been possible without them. A great deal of credit goes to Maj Mike Miller, for being my thesis advisor, keeping me focused on the right path to take. In the midst of research, whenever I had strayed and applied too much energy into solving problems that turned out to be only ancillary to the core purpose, he set me back on course (as GPS measurements can correct for INS drifts). Special thanks go to him for his perpetual encouragement and enthusiasm.

Dr. Peter S. Maybeck is credited in watching over the integrity of the concepts detailed in this work. He provided a wealth of knowledge and expertise in the field of stochastic modeling and Kalman filtering. Cpt John F. Raquet provided important details about the applications of GPS and was always accessible and willing to answer questions, no matter how simple. The labor of Donald E. Smith, to keep the computers running properly, has been invaluable, as all of the work done in this research depended upon computer simulations. Stan Musick is one of the authors of MSOFE, and was glad to help in working through some of the program's quirks.

Thanks also go to my colleagues here during my tour at AFIT. There are my fellow classmates of the Guidance & Control department: 2Lt Barry Vanek, Cpt Brian Young, 2Lt Jamey Sillence, Cpt Andy Proud, and 2Lt Ken Fisher; I think we spent more time in

the lab than all the other places combined. There are my other friends from the Communications department: Cpt Bill O'Connor, 2Lt Ricardo Mediavilla, FLT LT Andrew Gillman (RAAF), Cpt Andy Feltman, 2Lt Dan Petrovich, 2Lt Patrick Swackhammer; we had a chance to do some fun stuff in the area.

Finally, special thanks go to my aunt, uncle, and cousin, Donna, Doug, and John Mallamas, and my virtual brothers, Andrew Thomas, Tom Kirby, and Keith Lamm, for all the confidence and encouragement all the way from the "home front."

To all those who are making the journey through AFIT and read this, get a season pass to King's Island and have some fun on the weekends, and on those late nights in the lab, remember Young's Jersey Dairy stays open past midnight.

– Steve Chastain

Table of Contents

| | |
|--|-----|
| Preface..... | i |
| Table of Contents | iii |
| List of Figures | vi |
| List of Tables | vii |
| Abstract | ix |
| 1. Introduction | 1 |
| 1.1. Background | 1 |
| 1.1.1. Instrument Landing System..... | 2 |
| 1.1.2. Global Positioning System | 4 |
| 1.1.3. Inertial Navigation System..... | 7 |
| 1.1.4. Sensor Integration..... | 9 |
| 1.2. Problem Definition..... | 11 |
| 1.3. Previous Research..... | 11 |
| 1.4. Scope of the Problem | 12 |
| 1.5. Assumptions..... | 13 |
| 1.6. Summary | 14 |
| 2. Theory..... | 15 |
| 2.1. Overview..... | 15 |
| 2.2. Extended Kalman Filter | 16 |
| 2.2.1. System Dynamics Model Equation | 18 |
| 2.2.2. Measurement Model Equation..... | 19 |
| 2.2.3. System Model Linearization..... | 20 |
| 2.2.4. Extended Kalman Filter Equations..... | 22 |
| 2.2.4.1. Propagation Phase | 22 |
| 2.2.4.2. Update Phase..... | 23 |
| 2.3. Multiple Model Adaptive Estimation (MMAE) | 24 |
| 2.4. Modified MMAE (M^3 AE)..... | 30 |

| | |
|--|----|
| 2.4.1. Parameter Space Discretization | 32 |
| 2.4.2. Inter-Residual Distance Feedback (IRDF) | 36 |
| 2.5. Summary | 38 |
| 3. Methodology..... | 39 |
| 3.1. Overview | 39 |
| 3.2. System Description | 39 |
| 3.3. Inertial Navigation System Models..... | 41 |
| 3.3.1. INS Dynamics Truth Model | 43 |
| 3.3.2. INS Dynamics Filter Model | 44 |
| 3.3.3. INS Measurement Filter Model | 44 |
| 3.4. Radar Altimeter Measurement Model..... | 45 |
| 3.5. Global Positioning System Models..... | 46 |
| 3.5.1. GPS Truth Models..... | 47 |
| 3.5.1.1. GPS Dynamics Model..... | 47 |
| 3.5.1.2. GPS Measurement Model | 50 |
| 3.5.2. Differential GPS Truth Models | 51 |
| 3.5.2.1. DGPS Dynamics Model..... | 52 |
| 3.5.2.2. DGPS Measurement Model | 53 |
| 3.5.3. DGPS Filter Models | 54 |
| 3.5.4. GPS Pseudolite Models | 55 |
| 3.6. Integrated System Models..... | 55 |
| 3.7. Interference Models | 57 |
| 3.8. Simulation Software..... | 58 |
| 3.9. Parameter Estimation | 59 |
| 3.10. Summary | 61 |
| 4. Analysis of Results | 62 |
| 4.1. Flight Profile | 62 |
| 4.2. GPS Data..... | 63 |
| 4.3. Navigation System Configurations | 64 |
| 4.4. GPS RF Interference Scenarios..... | 64 |
| 4.5. PLS Comparison Criteria | 66 |
| 4.6. Nominal Interference Scenario | 69 |
| 4.6.1. Case I..... | 69 |

| | |
|--|-----|
| 4.6.2. Case II..... | 74 |
| 4.7. "Exponential" Noise Levels Scenarios | 77 |
| 4.7.1. Case III | 78 |
| 4.7.2. Case IV | 86 |
| 4.8. Increasing Noise Levels Scenarios..... | 91 |
| 4.8.1. Case V | 92 |
| 4.8.2. Case VI..... | 96 |
| 4.9. Decreasing Noise Levels Scenarios | 99 |
| 4.9.1. Case VII..... | 100 |
| 4.9.2. Case VIII..... | 103 |
| 4.10. Summary | 106 |
| 5. Conclusions and Recommendations..... | 107 |
| 5.1. Overview | 107 |
| 5.2. Conclusions | 107 |
| 5.3. Recommendations | 109 |
| Appendix A. Acronym List | 110 |
| Appendix B. Error States of the Truth and Filter Models | 111 |
| Appendix C. Truth Model System Dynamics and Process Noise Matrices | 120 |
| Appendix D. Filter Model Process and Measurement Noise Matrices..... | 125 |
| Bibliography..... | 127 |
| Vita..... | 133 |

List of Figures

| | |
|---|-----|
| Figure 1. Localizer Service Range | 3 |
| Figure 2. Glideslope Service Range..... | 3 |
| Figure 3. Differential GPS | 6 |
| Figure 4. Configuration using Tight Integration | 10 |
| Figure 5. Configuration using Loose Integration | 10 |
| Figure 6. M ³ AE Structure | 16 |
| Figure 7. MMAE Structure for Parameter Estimation | 26 |
| Figure 8. MMAE Structure | 31 |
| Figure 9. Navigation System Block Diagram | 41 |
| Figure 10. Actual Trajectory of the Simulated Landing Aircraft | 63 |
| Figure 11. GPS Interference Scenarios..... | 66 |
| Figure 12. Parameter / Estimated Probability Plot Legend..... | 68 |
| Figure 13. Position Error Plot Legend | 68 |
| Figure 14. Case I: Estimated Parameter and Elemental Filter Probabilities..... | 70 |
| Figure 15. Case I: State Estimator Position Errors | 72 |
| Figure 16. Case II: Estimated Parameter and Elemental Filter Probabilities..... | 75 |
| Figure 17. Case II: State Estimator Position Errors..... | 76 |
| Figure 18. Case III: Estimated Parameter and Elemental Filter Probabilities | 79 |
| Figure 19. Case III: Blended (MMAE) Position Errors..... | 82 |
| Figure 20. Case III: Elemental Filter ($a_1 = 1.0$) Position Errors | 83 |
| Figure 21. Case III: State Estimator Position Errors..... | 84 |
| Figure 22. Case IV: Blended (MMAE) Position Errors | 87 |
| Figure 23. Case IV: Elemental Filter ($a_1 = 1.0$) Position Errors..... | 88 |
| Figure 24. Case IV: State Estimator Position Errors | 90 |
| Figure 25. Case V: Estimated Parameter and Elemental Filter Probabilities | 93 |
| Figure 26. Case V: State Estimator Position Errors..... | 95 |
| Figure 27. Case VI: State Estimator Position Errors | 97 |
| Figure 28. Case VII: Estimated Parameter and Elemental Filter Probabilities..... | 101 |
| Figure 29. Case VII: State Estimator Position Errors | 102 |
| Figure 30. Case VIII: State Estimator Position Errors..... | 104 |

List of Tables

| | | |
|-----------|---|-----|
| Table 1. | FAA ILS Precision Approach Requirements (1σ)..... | 4 |
| Table 2. | Precision Values Available with GPS | 6 |
| Table 3. | Simulation Test Cases..... | 65 |
| Table 4. | FAA ILS Precision Approach Requirements ($\pm 1\sigma$) | 67 |
| Table 5. | Case I: East Position Error Standard Deviations | 73 |
| Table 6. | Case I: North Position Error Standard Deviations..... | 74 |
| Table 7. | Case I: Vertical Position Error Standard Deviations | 74 |
| Table 8. | Case II: East Position Error Standard Deviations..... | 77 |
| Table 9. | Case II: North Position Error Standard Deviations | 77 |
| Table 10. | Case II: Vertical Position Error Standard Deviations..... | 77 |
| Table 11. | Case III: East Position Error Standard Deviations | 85 |
| Table 12. | Case III: North Position Error Standard Deviations..... | 85 |
| Table 13. | Case III: Vertical Position Error Standard Deviations | 86 |
| Table 14. | Case IV: East Position Error Standard Deviations | 91 |
| Table 15. | Case IV: North Position Error Standard Deviations..... | 91 |
| Table 16. | Case IV: Vertical Position Error Standard Deviations | 91 |
| Table 17. | Increasing Noise Levels Scenario | 92 |
| Table 18. | Case V: East Position Error Standard Deviations | 96 |
| Table 19. | Case V: North Position Error Standard Deviations..... | 96 |
| Table 20. | Case V: Vertical Position Error Standard Deviations | 96 |
| Table 21. | Case VI: East Position Error Standard Deviations | 98 |
| Table 22. | Case VI: North Position Error Standard Deviations..... | 98 |
| Table 23. | Case VI: Vertical Position Error Standard Deviations | 98 |
| Table 24. | Decreasing Noise Levels Scenario | 99 |
| Table 25. | Case VII: East Position Error Standard Deviations..... | 103 |
| Table 26. | Case VII: North Position Error Standard Deviations | 103 |
| Table 27. | Case VII: Vertical Position Error Standard Deviations..... | 103 |
| Table 28. | Case VIII: East Position Error Standard Deviations | 105 |
| Table 29. | Case VIII: North Position Error Standard Deviations..... | 105 |

| | | |
|-----------|--|-----|
| Table 30. | Case VIII: Vertical Position Error Standard Deviations | 105 |
| Table 31. | ILS Precision Approach Categories Met for each Test Case | 106 |
| Table 32. | Original 93-State Truth Model for the INS: States 1 - 31 | 112 |
| Table 33. | Original 93-State Truth Model for the INS: States 32 - 63 | 113 |
| Table 34. | Original 93-State Truth Model for the INS: States 64 - 93 | 114 |
| Table 35. | Reduced-Order 39-State Truth Model for the INS: States 1 - 20 | 115 |
| Table 36. | Reduced-Order 39-State Truth Model for the INS: States 21 - 39 | 116 |
| Table 37. | 30-State Truth Model for GPS | 117 |
| Table 38. | 22-State Truth Model for Differential GPS..... | 118 |
| Table 39. | 13-State Filter Model (for all navigation components)..... | 119 |
| Table 40. | Elements of the System Dynamics Submatrix, F_{11} | 121 |
| Table 41. | Elements of the System Dynamics Submatrix, F_{12} | 122 |
| Table 42. | Elements of the Dynamics Submatrix, F_{13} | 122 |
| Table 43. | Elements of the Dynamics Submatrix, F_{14} | 123 |
| Table 44. | Elements of the Dynamics Submatrix, F_{22} | 123 |
| Table 45. | Elements of Process Noise Submatrix Q_{11} | 124 |
| Table 46. | Elements of Process Noise Submatrix Q_{22} | 124 |
| Table 47. | Process Noise Strength Values (Q) for Filter States (0.4 nmi/hr INS)..... | 125 |
| Table 48. | Process Noise Strength Values (Q) for Filter States (4.0 nmi/hr INS)..... | 126 |
| Table 49. | Measurement Noise Strengths Values (R) for the Truth and Filter States | 126 |

Abstract

Several past research efforts have developed methods to take advantage of Global Positioning System (GPS) positioning and apply it to a precision landing system (PLS). There have been proposals to phase out the current *Instrument Landing System* (ILS) in favor of a more cost-efficient and effective system. Accomplishments have been made in detailing a system implementing an INS aided with differential GPS, a GPS pseudolite, and a radar altimeter to handle the critical PLS requirements. This research applies the newly developed *Modified Multiple Model Adaptive Estimation* (M^3AE) architecture in an attempt to enhance the performance of a PLS in an environment involving GPS interference. The M^3AE uses Multiple Model Adaptive Estimation (MMAE) and Kalman filtering techniques to estimate the levels of interference and the navigation performance of the aircraft simultaneously. In addition, in the original development of M^3AE , the truth and filter model used were of the same order. This research serves as a demonstration of M^3AE applied to system where the truth model is of a higher order than the filter model.

Integrated GPS/INS Precision Approach Landing with M³AE Interference Avoidance

1. Introduction

The focus of this research is to examine an application of a newly developed method of simultaneous state and parameter estimation to the precision approach and landing problem [11, 22, 45]. The study involves a simulated aircraft navigation system using an inertial navigation system (INS) augmented with data from altimeters and Global Position System (GPS) receivers. It extends the efforts of previous analyses from the Air Force Institute of Technology (AFIT) entailing integrated aircraft navigation systems [7, 13, 34, 38, 56].

1.1. Background

There has been extensive research in aircraft automatic precision approach and landing systems [5, 7, 10, 11, 13, 18, 22, 45, 56]. These systems prove invaluable during periods of low visibility, or when a pilot is unfamiliar with the landing site. Landing safely involves many factors, including flying at the proper speed and attitude, knowing where the aircraft and the landing point are accurately, and having a clear view or indication of the landing point.

1.1.1. Instrument Landing System

The current system in use by the Department of Defense and civil aviation is the Instrument Landing System (ILS) [10]. This system is a highly directional guidance system that gives the pilot critical information pertaining to the aircraft's azimuth relative to the centerline of the runway, called the *localizer*, and the aircraft's approach elevation relative to the surface of the runway, called the *glideslope*. The modulated signals provide aircraft course and direction information to the pilot [47]. The system transmits two principal carrier signals, 108.10 MHz to 111.95 MHz for the localizer and 329.15 MHz to 335.00 MHz for the glideslope. The localizer beam can be received 35° from both sides of the runway centerline up to 10 nautical miles (nmi) away and 10° up to 18 nmi. The glideslope beam is 1.4° wide centered at an ideal glideslope of approximately 3° . This translates to approximately a 1,000 ft. drop in altitude for every 3 nmi traveled, a guideline many pilots use for a quick check [58]. In addition, this signal is normally usable up to 10 nmi away. Both carrier signals are modulated with a different frequency signal, depending on which side of the beam centerline the aircraft is. The two modulating frequencies are 90 Hz and 150 Hz. (Figures 1 and 2 illustrate how this is applied).

This system is in use extensively and satisfies the Federal Aviation Administration (FAA) Category III requirements for aircraft precision approaches [12]. However, due to the cost of maintaining the aging ILS structure, there is an active search for replacement systems. One alternative being actively pursued involves applying Global Positioning System (GPS) based systems as a low-cost, flexible substitute [5, 18, 45].

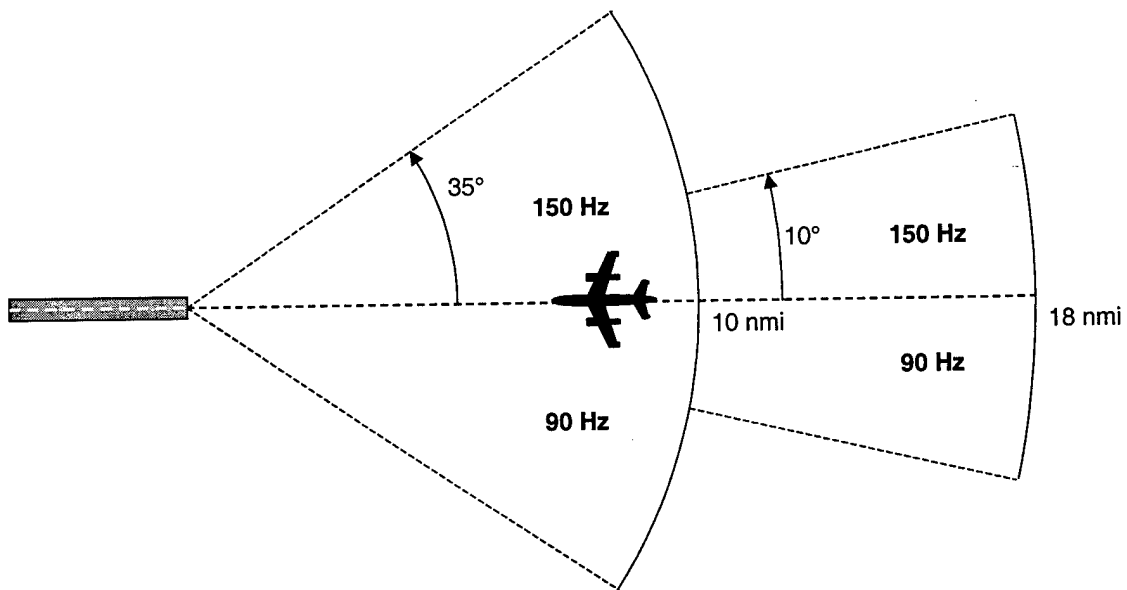


Figure 1. Localizer Service Range

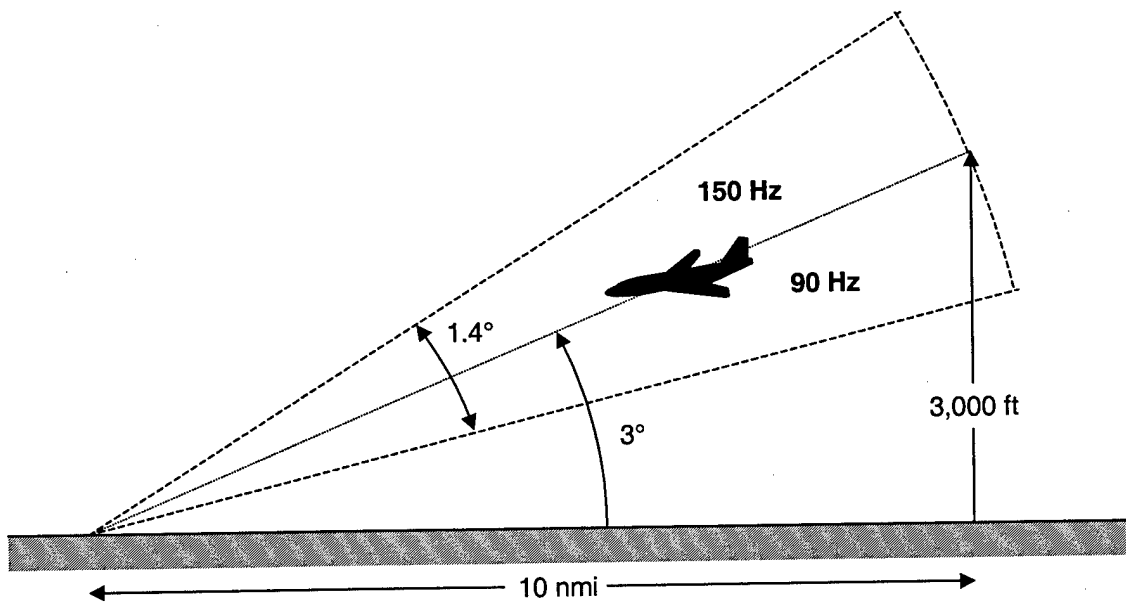


Figure 2. Glideslope Service Range

GPS is a well-established, reliable system for navigation and surveying, and is currently being used as a supplemental navigation aid for non-precision aircraft approaches.

1.1.2. Global Positioning System

The FAA is working closely with state aviation and industry officials to develop GPS-type procedures for all U.S. airports [5, 18, 45]. Several procedures, unique to GPS, have already been developed. One method uses differential GPS (DGPS) to provide error correction data to incoming aircraft that use GPS as a navigational aid [5, 18, 45].

Another advantage of GPS is its ability to provide the pilot more flexible landing approach options, unlike the ILS, which obliges landing aircraft to follow one prescribed approach pattern closely, limiting the pilot's choices.

Any alternative navigation system must still conform to the FAA precision landing requirements and must satisfy Category III performance before it can be considered as a replacement to ILS. Table 1 gives the constraint parameters for the different categories [7, 13].

Table 1. FAA ILS Precision Approach Requirements (1σ)

| Category | Horizontal Accuracy | Vertical Accuracy |
|-----------------|----------------------------|--------------------------|
| I | ± 28.1 ft | ± 6.8 ft |
| II | ± 8.6 ft | ± 2.8 ft |
| III | ± 6.8 ft | ± 1.0 ft |

Relying solely on a GPS-based system is inadequate. The GPS transmissions, which are universally available, are those of the standard positioning service (SPS). As a security measure, SPS can be degraded by introducing a random drift known as selective availability (SA) to reduce the precision available to users outside of the U. S. Armed Forces [37]. Currently SA is active, and, as shown in Table 2, the level of accuracy for GPS is unacceptable for even a Category I approach. However, even without SA, the precision available fails to meet any of the FAA criteria for vertical accuracy (see Table 2). This lack of precision, along with the unavailability of the precise positioning service (PPS) signal to the public has encouraged the development of other methods to decrease the error levels in SPS. One method that had gained popularity is the use of differential GPS (DGPS).

DGPS yields greater position accuracy by eliminating errors common to GPS receivers. The reference DGPS receiver is located at a surveyed spot, known with a high degree of accuracy, e.g., at an airport. When the GPS signals it receives are compared to those from another receiver, e.g., on board an aircraft, error corrections can be calculated and sent to the other receiver, improving the accuracy of its positioning; see Figure 3. The two receivers should be within 27 nmi (50 Km) to be effective [24]. While highly accurate, positioning using DGPS falls short of the required precision for FAA approaches, Table 2.

Centimeter-level precision can be achieved using another method known as carrier-phase GPS, which calculates the phase shift of the SPS carrier signal, L1, at 1,575.42 MHz. The wavelength of L1 is approximately 19 cm; the positioning accuracy is a fraction of this wavelength. However, determining the number of whole (integer) cycles

between the satellite and receiver becomes a problem. A momentary loss of the signal can disrupt the count of the whole cycles, resulting in *integer ambiguities* [4]. Currently, most carrier-phase uses have concentrated on surveying applications, since determining integer ambiguities is more difficult in a dynamic environment [41, 42].

Table 2. Precision Values Available with GPS

| GPS Method | Horizontal Accuracy | Vertical Accuracy |
|----------------|---------------------|-------------------|
| SPS with SA | ± 134.8 ft | ± 168.6 ft |
| SPS without SA | ± 33.5 ft | ± 42.0 ft |
| SPS using DGPS | ± 7.2 ft | ± 9.2 ft |

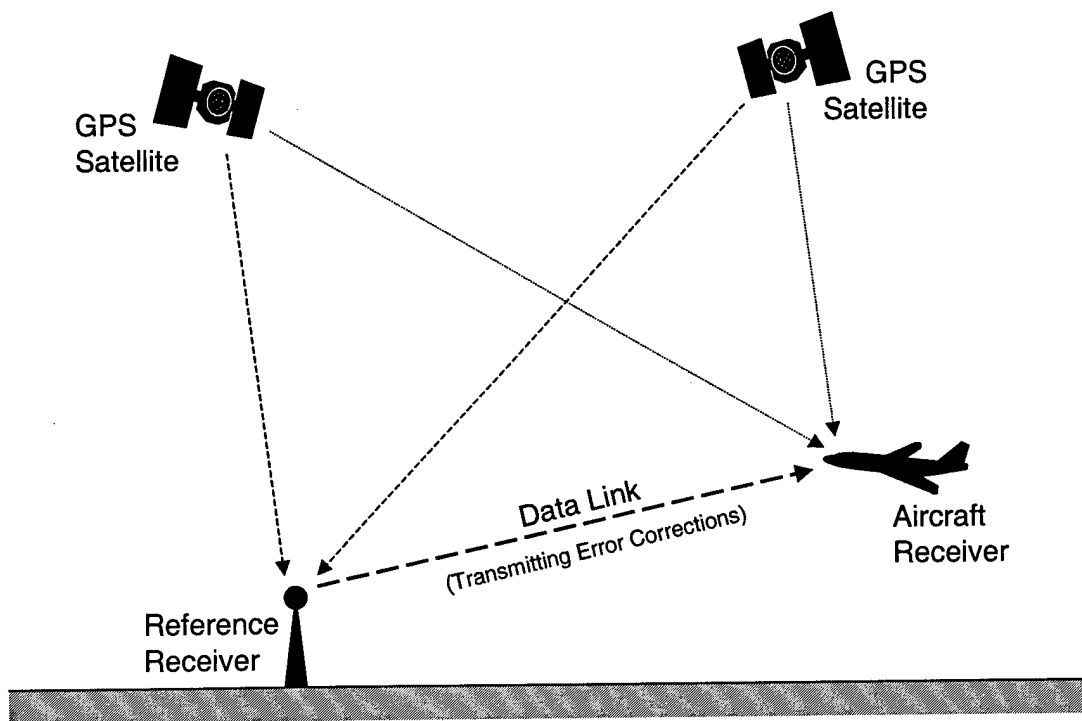


Figure 3. Differential GPS

1.1.3. Inertial Navigation System

Most aircraft use an inertial navigational system (INS) for their standard navigation aid. An INS is a self-contained “box” (it requires no outside information) that uses a system of gyros and accelerometers to sense specific forces as the aircraft’s position, velocity, and attitude changes. With a knowledge of the gravitational field, the INS integrates the specific forces over time to calculate its velocity and position with respect to a known reference frame. A significant drawback of an INS is that the readings in the vertical direction (relative to the earth) are unstable. This is usually corrected by the addition of a barometric altimeter to the INS. For better accuracy at lower altitudes, a radar altimeter can further improve the vertical position accuracy. Another problem is that INS-derived positions have errors that grow over time, resulting in a drift [27]. This can be corrected using ground-based navigation aids such as VHF Omnidirectional Range (VOR) and Tactical Air Navigation (TACAN).

GPS can serve as a replacement for these ground-based aids and adds flexibility in the flight path, as the aircraft does not have to follow a trajectory to stay in range of a VOR or TACAN system. As seen above, GPS also has a weakness in vertical positioning. This is due to the fact that the local horizon of a receiver limits the visibility of the GPS constellation. Only satellites above the horizon, or more commonly, above a user-selectable elevation mask angle (set to minimize ground clutter and atmospheric conditions) can be used to determine a navigation solution. One method to improve vertical GPS precision uses ground-based GPS transmitters, called *pseudolites*, to provide a GPS-like signal from below an aircraft’s horizon. Pseudolites require extremely low

power transmissions to mimic the -163 dB_w GPS signal power level while not saturating the L1 frequency with its own signal and blocking actual GPS satellite transmissions.

The low power level of GPS transmissions brings to light the problems of interference and noise. GPS spread spectrum provides some protection; still some interference has been experienced from users when receiving spurious emissions near the L1 band, such as second and third harmonics of UHF television stations, and even higher order harmonics from VOR and TACAN [40]. Also, there is the risk of someone deliberately broadcasting interference to deny any GPS signals to a receiver (“jamming”) or mimicking transmissions from a satellite to give erroneous information (“spoofing”).

Recall that an INS is a self-contained system that does not rely on outside navigational signals or beacon transmissions. Despite its inherent long-term drift characteristics, an INS provides velocity and position estimates with high degree of precision and low error standard deviation in the short-term. A great deal of work has been done integrating systems such as GPS receivers and one or more INSs (for failure redundancy), combining the benefits of GPS accuracy with the protection INS systems have against external noise [2, 4, 13, 14, 17, 19, 21, 23, 39, 44, 45, 50, 51, 56].

Integration of navigation aids can further improve the performance of the system. Due to the dependence on GPS, it would be useful to have a system that could determine the level of accuracy and reliability of GPS transmissions before computing a navigation solution.

1.1.4. Sensor Integration

An extended Kalman filter can combine the position, velocity, and attitude states output by the INS with measurements from a GPS receiver, barometric and radar altimeters, and a pseudolite to determine the best estimate of those states. The Kalman filter in this research uses tight integration to process the measurements. Tight integration incorporates raw measurements from all sensors, e.g., pseudoranges for GPS, into a central Kalman filter as shown in Figure 4. In contrast, loose integration provides each sensor (or a selected subset of sensors) with its own filter to process its measurements before incorporating the measurements into the central filter as shown by Figure 4. Although loose integration offers less complexity for each filter, tight integration is preferred in this case, as it requires the design and tuning of only a single filter and has better performance potential [20].

Furthermore, in cases where fewer than four GPS signals are available (the minimum to compute positions and velocities using GPS), the filter can still function properly [27]. If a separate filter is devoted to processing GPS measurements, as in loose integration, it cannot give an unambiguous estimate when there are fewer than four measurements available. The entire benefit of GPS is lost during those periods. When tight integration is implemented, all measurements are delivered to a single state estimation filter. When there are fewer than four GPS measurements available, the filter continues to function, deriving some advantage of having at least partial information from GPS.

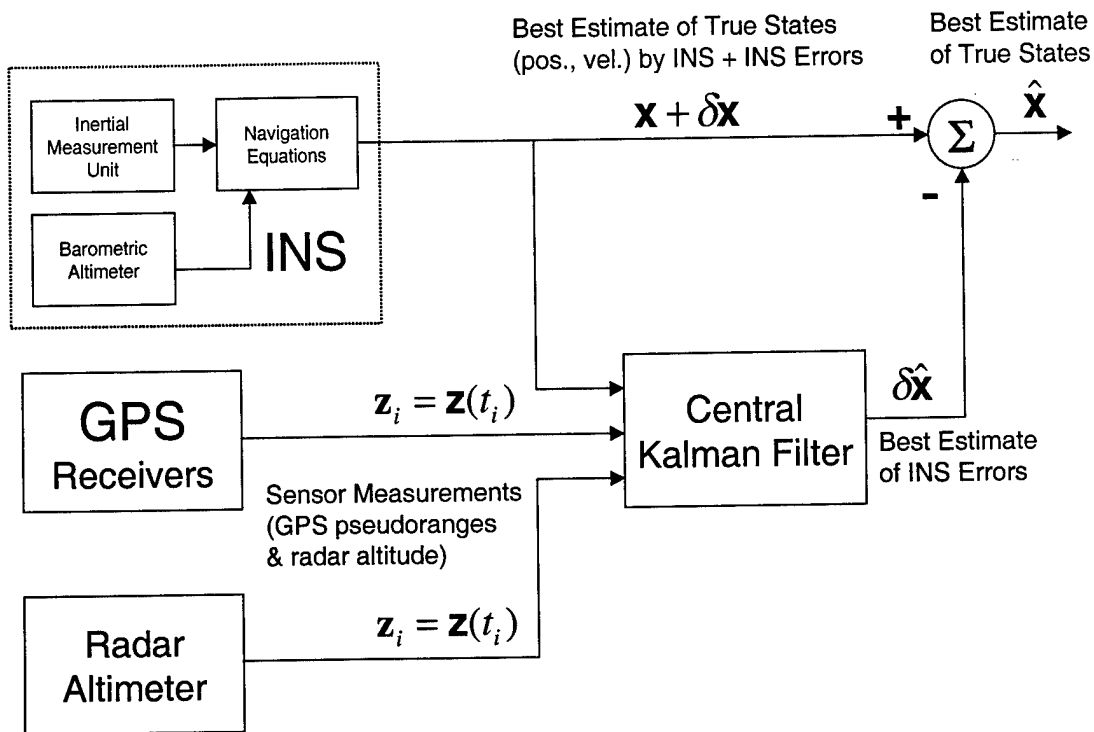


Figure 4. Configuration using Tight Integration

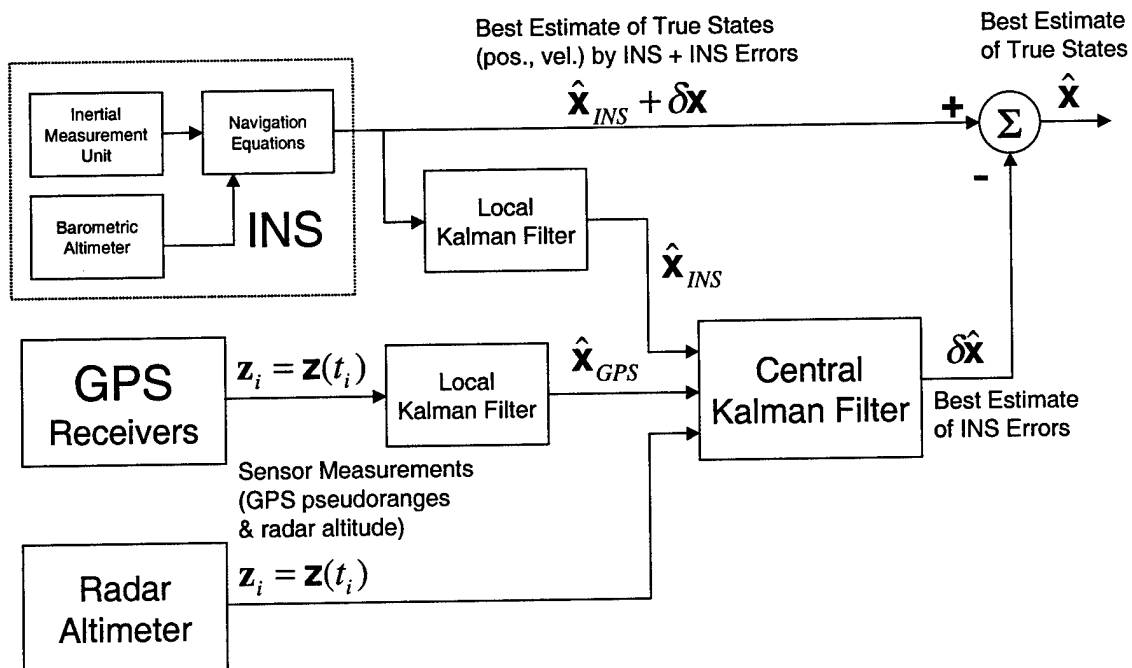


Figure 5. Configuration using Loose Integration

1.2. Problem Definition

The core of this work is to examine the application of the newly developed Modified Multiple Model Adaptive Estimation (M^3AE) algorithm [33] to an existing navigational system model using a GPS-aided INS in the presence of external interference. This algorithm is then applied to the precision landing problem to determine its suitability.

1.3. Previous Research

A great deal of research has been conducted to develop an adequate precision landing system (PLS) using GPS [5, 7, 11, 13, 18, 22, 45, 56]. One significant effort is the FAA's Local Area Augmentation System (LAAS), which is based upon a ground-based system broadcasting DGPS error corrections and utilizing airport pseudolites [5, 18]. Within AFIT, there have been two realms of research applicable to PLS. The first relates to the practical aspects of PLS, which include Johnson [23] and Negast [38] who focused on GPS/INS navigation systems. The work of Gray [13] applied the system to a PLS and showed that ILS Category II could be satisfied using a GPS-aided INS with radar altimeter and pseudolite measurements incorporated. Britton [7] follows this by using differential GPS (DGPS) measurements to show Category III could be met. White [56] investigated the performance a PLS in the presence of GPS interference and spoofing. White implemented Multiple Model Adaptive Estimation (MMAE) [31] techniques to adjust the navigational system's model to give dependable results. Advanced developments in more theoretical topics involving the M^3AE architecture expanded the capabilities of MMAE to handle the task of simultaneous estimation of interference levels and navigation performance [33, 55].

1.4. Scope of the Problem

The basis of this work is the expansion of the effort at AFIT towards investigating PLSs [56]. It will primarily be the application of the algorithm developed by Miller known as Modified MMAE (M^3 AE) [33] and to extend the work of White to simulate varying GPS interference levels for a GPS/INS PLS [33]. This research uses a computer-based simulation, *Multiple Model Simulation for Optimal Filter Evaluation* (MMSOFE) [39], to test the performance of a model of the PLS. The model of the PLS implemented at AFIT assumes the INS is the primary navigation aid.

Two configurations are investigated using various INS models with two different drift rates, combined with various combinations of other navigation aids to determine the effects on the overall performance of the system. The principal criteria by which to judge the performance are the FAA precision approach categories. All aircraft navigational computers can only use finite-order models of the system. To reflect this, an elaborate 96-state truth model is used to simulate “real-world” aircraft position, velocity, and attitude errors, and a reduced-order 13-state filter model serves as the aircraft’s on-board navigation filter model of sensor error characteristics. The difference between the states of the truth model and state estimates of the filter model will provide the error data to be weighed against the FAA categories. Monte Carlo analysis is conducted to tune each filter model for optimal performance and to determine whether the configuration is sufficient for a PLS. Monte Carlo analysis is conducted using MMSOFE, along with MPLOT. MPLOT is a software tool used in conjunction with MMSOFE that extracts the raw data from the files created by MMSOFE to provide usable data for plotting [36].

In addition, this work serves as an initial application of M^3AE techniques to a practical situation. The M^3AE concept has been verified using truth and filter models of the same order [33]. The capability of M^3AE using a more realistic and complete truth model and a reduced-order filter model in the simulation is accomplished.

1.5. Assumptions

As in all research, a number of assumptions must be made to define the limits of the corresponding results and conclusions. The most crucial elements are the models used to depict the behavior of navigation equipment in the real world. The 96-state truth model is assumed to represent how the system would perform in the real world, while the filter model serves as an example of how an operational navigation system would be implemented. The simulated flight profile and GPS satellite ephemeris data used are generated by a program called PROFGEN [35] designed specifically to create the proper files for use with MMSOFE [39].

The INS is assumed to have a barometric altimeter integrated with it, as this is commonly done to stabilize the INS's vertical readings. A feed-forward configuration is used with the INS, which means the INS receives no data to update its current position. Although a feedback configuration in which the INS could accept position updates from the navigation filter could yield better accuracy, if the measurements of a sensor were corrupted, the INS would be extrapolating its states based on an erroneous input which can further distort its results.

The presence of GPS interference is modeled as zero-mean white Gaussian noise (WGN) in the measurement models. This is the only interference to be taken into

account; the INS is considered to be unaffected by outside disturbances, and jamming of the radar altimeter is not examined. Pseudolites can be affected in the same manner as GPS satellite signals.

1.6. Summary

This work follows the progress of other studies concerning integrated GPS/INS navigation. The intent is to incorporate the recently developed theory behind simultaneous parameter and state estimation with M^3 AE into this path of study, PLS improvement. Chapter 2 presents the theory behind a critical tool of modern navigation systems, Kalman filtering. It then follows with a description of parameter and state estimation using MMAE, and provides an overview of the development behind M^3 AE. Chapter 3 presents the system models implemented in the simulations. The structure of the models for each navigation system component is described as well as the states and measurements modeled. Chapter 4 shows the results obtained through simulations and the corresponding analysis of the performance observed. Lastly, Chapter 5 gives a summary of conclusions based on this work and any recommendation for other paths of study.

2. Theory

2.1. Overview

The overall structure of the navigation system simulated in this work is based on a *modified MMAE* (M^3AE). Miller developed this method as a solution to the dilemma in simultaneously estimating both the states and the parameters of a system model accurately [33]. The structure of M^3AE is composed of two major parts: the MMAE, designed specifically for parameter estimation, and a single extended Kalman filter (EKF) tuned precisely for state estimation, once provided the parameter estimate from the MMAE.

The MMAE is composed of a bank of Kalman filters, each one based upon a different value of parameters. Both the MMAE and state estimator receive measurements from the external sensors. The MMAE uses these data to come up with a blended parameter estimate, which is passed on to the state estimator. The state estimator then has the best model available to render its estimate of the states, based on the incoming measurements. In this way, accurate state estimates can be obtained in an environment where some of the parameters of the model can change. The Kalman filter serves as the fundamental building block of an M^3AE ; thus, an explanation of the M^3AE begins from the most elementary component proceeding towards the overall structure.

This study uses Kalman filters to combine various sensor data (INS, GPS, etc.) to obtain an optimal estimate of the aircraft's position and velocity. Kalman filtering has been used considerably in navigation applications [19, 27].

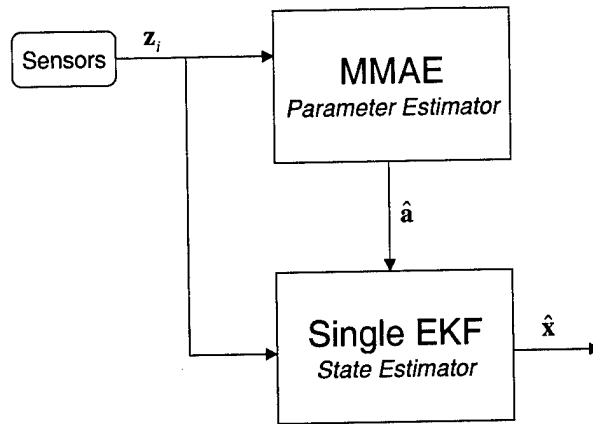


Figure 6. M³AE Structure

It is well suited for this due its ability to take into account levels of uncertainty of states and measurements within a system. Kalman filtering deals with systems that can be described by a set of linear, time-varying, stochastic differential equations [24, 30]. In a sampled-data environment, such as a computer, discrete difference equations can be used with some adaptation. The stochastic processes involved are represented by white Gaussian noise (WGN), usually zero-mean unless a bias is needed. “White” indicates that the value of the process at an instant of time is independent of all other values at any other time, i.e., “perfect” randomness. Gaussian functions are used since uncorrelated jointly Gaussian functions are also independent. The strength values can be adjusted to fit the level of uncertainty needed for the models.

2.2. Extended Kalman Filter

Originally, Kalman filters were designed to handle systems adequately described by linear models [30]. All models are approximations, and in many cases, linear models have deficiencies that are not negligible. This is often the case when the noise strengths,

i.e., levels of uncertainty, of the model are small values. Over time, the states of the filter can rely too heavily on the system model and become affected less by external measurements. This can result in model behavior that strays away from the actual real-world situation [31]. Several methods have been developed to counteract this. Some restrict the variance of the states from going below a certain value or have a built-in minimum threshold of uncertainty. Others limit the “memory” of the filter, such as in *Fagin age-weighting* where the effects of more recent measurements are magnified by increasing the assumed noise variance of earlier measurements exponentially backwards in time [31]. In cases where the linear model cannot sufficiently characterize the system, the filter equations can be adapted to handle non-linear equations. A *linearized* Kalman filter assumes that a nominal state trajectory (value of the state vector over time) exists and estimates the *perturbation* about the nominal value. The perturbation is defined as the first-order term of the Taylor series of the difference between the state vector and its nominal trajectory. This filter performs well unless the actual and nominal state trajectories differ significantly [31]. To compensate for this, *extended* Kalman filtering (EKF) relinearizes about the most recent state update. Thus, the filter computes a new nominal state trajectory after each update phase.

In the equations that follow, a certain type of notation is used, following a convention adopted by Maybeck [30, 31, 32]. Vector and matrix variables are distinguished from scalar variables through a boldface type. Boldface, lower-case letters are reserved for vectors and capital letters for matrices. Thus, a , b , c would be scalars, \mathbf{a} , \mathbf{b} , \mathbf{c} would be vectors, and \mathbf{A} , \mathbf{B} , \mathbf{C} would be matrices. Variables are further distinguished by typeface.

Roman type indicates a deterministic variable, e.g., **a**, **b**, **c**, while a *sans-serif* (Helvetica) type indicates a stochastic variable, e.g. **a**, **b**, **c**.

2.2.1. System Dynamics Model Equation

Consider the linear system dynamics model equation used for Kalman filtering

$$\dot{\mathbf{x}}(t) = \mathbf{F}(t)\mathbf{x}(t) + \mathbf{B}(t)\mathbf{u}(t) + \mathbf{G}(t)\mathbf{w}(t) \quad (1)$$

where $\mathbf{x}(t)$ is the state vector, $\mathbf{F}(t)$ is the system dynamics matrix, $\mathbf{u}(t)$ is a vector of deterministic control inputs with $\mathbf{B}(t)$ as a control input matrix, and $\mathbf{w}(t)$ is a vector of zero-mean WGN with $\mathbf{G}(t)$ as a noise input matrix. Note, $\mathbf{w}(t)$ is the hypothetical time derivative of a Brownian motion process $\beta(t)$

$$\mathbf{w}(t) = \frac{d\beta(t)}{dt} \quad (2)$$

which does not exist in the real world since $\mathbf{w}(t)$ has an equal power density over all possible frequencies (hence, the term “white”). However, if it is assumed that a finite band of frequencies (of concern to the problem) is used, then $\mathbf{w}(t)$ “appears” as a white noise process within that band. Also, since $\mathbf{w}(t)$ is a Gaussian process, two statistics, mean and (auto)covariance kernel, are sufficient to completely describe how it behaves:

$$E\{\mathbf{w}(t)\} = \mathbf{0} \quad (3)$$

$$E\{\mathbf{w}(t)\mathbf{w}^T(t + \tau)\} = \mathbf{Q}(t)\delta(\tau) \quad (4)$$

$\mathbf{Q}(t)$ is a square matrix that can be interpreted as the strength of the WGN, while $\delta(\tau)$ is the Dirac delta function, also known as the impulse function. With the addition of $\mathbf{w}(t)$, $\mathbf{x}(t)$ becomes a stochastic variable itself with these statistics:

$$E\{\mathbf{x}(t)\} = \hat{\mathbf{x}}(t) \quad (5)$$

$$E\{[\mathbf{x}(t) - \hat{\mathbf{x}}(t)][\mathbf{x}(t) - \hat{\mathbf{x}}(t)]^T\} = \mathbf{P}(t) \quad (6)$$

$\hat{\mathbf{x}}(t)$ is interpreted as the best estimate of the state vector at time t , and $\mathbf{P}(t)$ is its corresponding covariance or range of uncertainty.

When the system dynamics cannot be expressed as a set of linear equations, a non-linear function must be set up for the model:

$$\dot{\mathbf{x}}(t) = \mathbf{f}[\mathbf{x}(t), \mathbf{u}(t), t] + \mathbf{G}(t)\mathbf{w}(t) \quad (7)$$

where $\mathbf{f}[\mathbf{x}(t), \mathbf{u}(t), t]$ is the non-linear vector function in terms of the state and control vectors and time. Also, in this research, no deterministic control inputs are considered, thus $\mathbf{B}(t)$ and $\mathbf{u}(t)$ are zero and do not appear from this point on.

2.2.2. Measurement Model Equation

The linear discrete measurement model equation used for Kalman filtering is

$$\mathbf{z}(t_i) = \mathbf{H}(t_i)\mathbf{x}(t_i) + \mathbf{v}(t_i) \quad (8)$$

where $\mathbf{z}(t_i)$ is the measurement vector, $\mathbf{H}(t_i)$ is the measurement matrix, and $\mathbf{v}(t_i)$ is a vector of zero-mean, discrete-time WGN representing the uncertainty of the measurements, or the measurement noise. It is important to note this equation is a discrete-time process (t_i instead of t) since measurements are taken at specific instants of time. Here, the measurements are considered to be taken at regular time intervals. The measurement noise $\mathbf{v}(t_i)$ has the following statistics:

$$E\{\mathbf{v}(t_i)\} = \mathbf{0} \quad (9)$$

$$E\{\mathbf{v}(t_i)\mathbf{v}^T(t_j)\} = \begin{cases} \mathbf{R}(t_i) & i = j \\ \mathbf{0} & i \neq j \end{cases} \quad (10)$$

In this description, $\mathbf{R}(t_i)$ is a square, positive definite matrix interpreted as the covariance of the noise $\mathbf{v}(t_i)$. $\mathbf{R}(t_i)$ being positive definite implies that all measurements, i.e., elements of $\mathbf{v}(t_i)$, are corrupted by noise, and no linear combination of these measurements would be free from noise. In addition, it is assumed that the state and noise vectors, $\mathbf{x}(t)$, $\mathbf{w}(t)$, and $\mathbf{v}(t_i)$, are uncorrelated with each other, and being jointly Gaussian this means they are also independent of each other[30].

As above, when the measurement dynamics cannot be expressed as a set of linear equations, a non-linear function must be used:

$$\mathbf{z}(t_i) = \mathbf{h}[\mathbf{x}(t_i), t_i] + \mathbf{v}(t_i) \quad (11)$$

where $\mathbf{h}[\mathbf{x}(t), t]$ is the non-linear vector function in terms of the state vector and time.

2.2.3. System Model Linearization

Equations (7) and (11) describe the non-linear model of the system of which a Kalman filter determines the best estimate of the states $\hat{\mathbf{x}}(t)$ and the estimation error covariance $\mathbf{P}(t)$. A linear approximation must be made to create a linearized Kalman filter to apply to the model. A nominal state trajectory $\mathbf{x}_n(t) \forall t \in T$ (T is the entire period the filter operates) is computed with initial conditions of $\mathbf{x}_n(t_0) = \mathbf{x}_{n_0}$, where the noise-free system dynamics equation is defined by

$$\dot{\mathbf{x}}_n(t) = \mathbf{f}[\mathbf{x}_n(t), t] \quad (12)$$

where $\mathbf{f}[\bullet, \bullet]$ is the same as in Equation (7). Nominal, noise-free measurements are also considered with the corresponding measurement equation

$$\mathbf{z}_n(t_i) = \mathbf{h}[\mathbf{x}_n(t_i), t_i] \quad (13)$$

where $\mathbf{h}[\bullet, \bullet]$ is the same as in Equation (11).

As mentioned in the beginning of this section, a linearized Kalman filter estimates a perturbation to the nominal trajectory. The state perturbation is found by subtracting the nominal states from the original states. This yields a system dynamics equation of

$$[\dot{\mathbf{x}}(t) - \dot{\mathbf{x}}_n(t)] = \{\mathbf{f}[\mathbf{x}(t), t] - \mathbf{f}[\mathbf{x}_n(t), t]\} + \mathbf{G}(t)\mathbf{w}(t) \quad (14)$$

Now, a Taylor series expansion is performed on $\mathbf{f}[\mathbf{x}(t), t]$ about $\mathbf{x}_n(t) \forall t \in T$

$$\mathbf{f}[\mathbf{x}(t), t] = \sum_{k=0}^{\infty} \frac{\partial^k \mathbf{f}[\mathbf{x}(t), t]}{\partial \mathbf{x}^k} \bigg|_{\mathbf{x}(t)=\mathbf{x}_n(t)} [\mathbf{x}(t) - \mathbf{x}_n(t)]^k \quad (15)$$

A first-order approximation may be made by neglecting all the terms with powers greater than one ($k \geq 2$)

$$\mathbf{f}[\mathbf{x}(t), t] \approx \mathbf{f}[\mathbf{x}_n(t), t] + \frac{\partial \mathbf{f}[\mathbf{x}(t), t]}{\partial \mathbf{x}} \bigg|_{\mathbf{x}(t)=\mathbf{x}_n(t)} [\mathbf{x}(t) - \mathbf{x}_n(t)] \quad (16)$$

Let

$$\mathbf{F}[t; \mathbf{x}_n(t)] \equiv \frac{\partial \mathbf{f}[\mathbf{x}(t), t]}{\partial \mathbf{x}} \bigg|_{\mathbf{x}(t)=\mathbf{x}_n(t)} \quad (17)$$

The linearized (first-order approximation) perturbation $\delta \mathbf{x}(t) \equiv [\mathbf{x}(t) - \mathbf{x}_n(t)]$ is found by substituting Equations (16) and (17) into Equation (14)

$$\delta \dot{\mathbf{x}}(t) = \mathbf{F}[t; \mathbf{x}_n(t)] \delta \mathbf{x}(t) + \mathbf{G}(t)\mathbf{w}(t) \quad (18)$$

The same procedure is applied to the measurement equation, with a Taylor series expansion of $\mathbf{h}[\mathbf{x}(t_i), t]$ about $\mathbf{z}_n(t_i) \forall t_i \in T$ yielding

$$\delta \mathbf{z}(t_i) = \mathbf{H}[t; \mathbf{x}_n(t_i)] \delta \mathbf{x}(t) + \mathbf{v}(t) \quad (19)$$

At this point, the Kalman filter equations can be applied, resulting in the linearized Kalman filter. It should be noted that, unlike the basic Kalman filter, the best estimates of the perturbation states $\delta \hat{\mathbf{x}}(t)$ are first-order approximations and not truly optimal. In

order to get the estimates of the states themselves, the nominal state trajectory must be added

$$\hat{\mathbf{x}}(t) = \mathbf{x}_n(t) + \delta\hat{\mathbf{x}}(t) \quad (20)$$

2.2.4. Extended Kalman Filter Equations

In many cases, the effect of neglecting the higher order terms of the Taylor series can cause the accuracy of the filter's predictions to stray over time. This is caused when the nominal state trajectory deviates significantly from the actual trajectory. Extended Kalman filtering solves this by relinearizing about the most recent state estimate $\hat{\mathbf{x}}(t)$ instead of the initial nominal state trajectory $\mathbf{x}_n(t)$. Thus, a new nominal trajectory is created for each cycle of the filter. Each cycle of a Kalman filter has two phases: *propagation* and *update*. Each filter update occurs at regular intervals t_i ($i = 0, 1, 2, \dots$) and of instantaneous duration. The propagation phase takes place during the intervals between t_i and t_{i+1} . In the EKF equations below, the following notation convention is observed [30, 31, 32]:

$t|t_i$ indicates the value of a given variable at time t , conditioned on measurements

taken through time t_i (this also represents the relinearization taking place).

t_i^- indicates the value after the propagation phase, prior to the update phase

t_i^+ indicates the value after the update phase, prior to the next propagation phase

2.2.4.1. Propagation Phase

The values of the state estimate $\hat{\mathbf{x}}(t|t_i)$ and state covariance $\mathbf{P}(t|t_i)$ are propagated from t_i^+ to t_{i+1}^- through the following differential equations:

$$\dot{\mathbf{x}}(t|t_i) = \mathbf{f}[\hat{\mathbf{x}}(t|t_i), t] \quad (21)$$

$$\dot{\mathbf{P}}(t|t_i) = \mathbf{F}[t; \hat{\mathbf{x}}(t|t_i)]\mathbf{P}(t|t_i) + \mathbf{P}(t|t_i)\mathbf{F}^T[t; \hat{\mathbf{x}}(t|t_i)] + \mathbf{G}(t)\mathbf{Q}(t)\mathbf{G}^T(t) \quad (22)$$

where

$$\mathbf{F}[t; \hat{\mathbf{x}}(t|t_i)] \equiv \left. \frac{\partial \mathbf{f}[\mathbf{x}(t), t]}{\partial \mathbf{x}} \right|_{\mathbf{x}(t) = \hat{\mathbf{x}}(t|t_i)} \quad (23)$$

with these initial conditions:

$$\hat{\mathbf{x}}(t_i|t_i) = \hat{\mathbf{x}}(t_i^+) \quad (24)$$

$$\mathbf{P}(t_i|t_i) = \mathbf{P}(t_i^+) \quad (25)$$

2.2.4.2. Update Phase

After each propagation, the discrete-time measurements $\mathbf{z}_i = \mathbf{z}(t_i)$ are applied. The updated values of the state estimate $\hat{\mathbf{x}}(t_i)$ and state covariance $\mathbf{P}(t_i)$ are computed through the following equations:

$$\mathbf{K}(t_i) = \mathbf{P}(t_i^-)\mathbf{H}^T[t_i; \hat{\mathbf{x}}(t_i^-)]\{\mathbf{H}[t_i; \hat{\mathbf{x}}(t_i^-)]\mathbf{P}(t_i^-)\mathbf{H}^T[t_i; \hat{\mathbf{x}}(t_i^-)] + \mathbf{R}(t_i)\}^{-1} \quad (26)$$

$$\hat{\mathbf{x}}(t_i^+) = \hat{\mathbf{x}}(t_i^-) + \mathbf{K}(t_i)\{\mathbf{z}_i - \mathbf{h}[\hat{\mathbf{x}}(t_i^-), t_i]\} \quad (27)$$

$$\mathbf{P}(t_i^+) = \mathbf{P}(t_i^-) - \mathbf{K}(t_i)\mathbf{H}[t_i; \hat{\mathbf{x}}(t_i^-)]\mathbf{P}(t_i^-) \quad (28)$$

where

$$\mathbf{H}[t; \hat{\mathbf{x}}(t|t_i)] \equiv \left. \frac{\partial \mathbf{h}[\mathbf{x}(t), t]}{\partial \mathbf{x}} \right|_{\mathbf{x}(t) = \hat{\mathbf{x}}(t|t_i)} \quad (29)$$

and translating the values after the propagation phase as:

$$\hat{\mathbf{x}}(t_i^-) = \hat{\mathbf{x}}(t_i|t_{i-1}) \quad (30)$$

$$\mathbf{P}(t_i^-) = \mathbf{P}(t_i|t_{i-1}) \quad (31)$$

The values $\hat{\mathbf{x}}(t_i^+)$ and $\mathbf{P}(t_i^+)$ are then used to start the next propagation phase and to recalculate the nominal state trajectory.

The term $\{\mathbf{z}_i - \mathbf{h}[\hat{\mathbf{x}}(t_i^-), t_i]\}$ in Equation (27) is known as the measurement residual, and is represented by $\mathbf{r}(t_i)$. The value of $\mathbf{r}(t_i)$ represents the difference between the actual measurements taken $\mathbf{z}_i = \mathbf{z}(t_i)$ and the filter's prediction of the measurements $\hat{\mathbf{z}}(t_i) = \mathbf{h}[\hat{\mathbf{x}}(t_i^-), t_i]$ based on the best estimate of the state vector prior to receiving \mathbf{z}_i . The characteristics of $\mathbf{r}(t_i)$ show how well the filter model simulates the behavior in the real world. In a linear Kalman filter, for an accurate model, $\mathbf{r}(t_i)$ will appear white and Gaussian with a mean of zero and a covariance of

$$\mathbf{A}(t_i) = \mathbf{H}[t_i; \hat{\mathbf{x}}(t_i^-)]\mathbf{P}(t_i^-)\mathbf{H}^T[t_i; \hat{\mathbf{x}}(t_i^-)] + \mathbf{R}(t_i) \quad (32)$$

Note this term is embedded in the expression for $\mathbf{K}(t_i)$ in (26). For an extended Kalman filter, this description is good only to the first order.

2.3. Multiple Model Adaptive Estimation (MMAE)

As a Kalman filter runs, the algorithm generates its prediction of the states of the system model, $\hat{\mathbf{x}}(t)$, along with an estimation error covariance $\mathbf{P}(t)$. All of this depends on how well the model itself depicts the system's behavior in the real world. The structure of the model is based on the parameters describing the interrelations of the states. For this work, these are the system dynamics function $\mathbf{f}[\mathbf{x}(t), t]$, system noise input matrix $\mathbf{G}(t)$, measurement function $\mathbf{h}[\mathbf{x}(t), t]$, and the strength of the system dynamics noise $\mathbf{Q}(t)$ and covariance of the measurement noise $\mathbf{R}(t_i)$. The filter can encounter difficulties when any of these quantities change from values assumed by the filter. Thus, it would be beneficial to have a filter that could adapt to such changes. A

technique known as multiple model adaptive estimation (MMAE) handles changes in system characteristics through a parallel bank of K individual Kalman filters (where K is the number of possible parameter values \mathbf{a}_k taken into account), each calculating its own best estimate of the state vector $\hat{\mathbf{x}}_k(t_i)$ with $\mathbf{P}_k(t_i)$ ($k = 1, 2, \dots, K$). When the measurements \mathbf{z}_i are given to the filters, they generate a set of residuals $\mathbf{r}_k(t_i)$. These residuals are processed by a *hypothesis conditional probability computation* algorithm to quantify how well each filter matches the real world circumstances. This is expressed as a conditional probability, $p_k(t_i)$, by the recursive equation

$$p_k(t_i) = \frac{f_{\mathbf{z}(t_i)|\mathbf{a}, \mathbf{Z}(t_{i-1})}(\mathbf{z}_i|\mathbf{a}_k, \mathbf{Z}_{i-1}) p_k(t_{i-1})}{\sum_{j=1}^K f_{\mathbf{z}(t_i)|\mathbf{a}, \mathbf{Z}(t_{i-1})}(\mathbf{z}_i|\mathbf{a}_j, \mathbf{Z}_{i-1}) p_j(t_{i-1})} \quad (33)$$

where \mathbf{a}_k is the value of parameters associated with the k^{th} filter, \mathbf{Z}_{i-1} is the realization of the variable of $\mathbf{Z}(t_{i-1})$, which is in turn a vector of cumulative measurements from the initial time t_0 to t_{i-1} :

$$\mathbf{Z}(t_{i-1}) = \begin{bmatrix} \mathbf{z}(t_{i-1}) \\ \mathbf{z}(t_{i-2}) \\ \vdots \\ \mathbf{z}(t_0) \end{bmatrix} \quad (34)$$

and $f_{\mathbf{z}(t_i)|\mathbf{a}, \mathbf{Z}(t_{i-1})}(\mathbf{z}_i|\mathbf{a}_k, \mathbf{Z}_{i-1})$ is a Gaussian density function with a mean of $\mathbf{r}_k(t_i)$ and a covariance of $\mathbf{A}_k(t_i)$:

$$f_{\mathbf{z}(t_i)|\mathbf{a}, \mathbf{Z}(t_{i-1})}(\mathbf{z}_i|\mathbf{a}_k, \mathbf{Z}_{i-1}) = \beta_k \exp\left\{-\frac{1}{2} L_k(t_i)\right\} \quad (35)$$

where

$$\beta_k = \frac{1}{(2\pi)^{\frac{n}{2}} |\mathbf{A}_k(t_i)|^{\frac{1}{2}}} \quad (36)$$

and

$$L_k(t_i) = \mathbf{r}_k^T(t_i) \mathbf{A}_k^{-1} \mathbf{r}_k(t_i) \quad (37)$$

The quantity $\mathbf{r}_k(t_i)$ is an m -dimension vector, i.e., m scalar measurements are taken at each measurement update interval. These conditional probabilities are then multiplied by their corresponding state estimates, which are summed to produce a *blended estimate* of the state vector $\hat{\mathbf{x}}(t_i)$. Figure 7 shows a block diagram of the MMAE [31].

The conditional probability is best interpreted as $p_k(t_i) = \text{Prob}[\mathbf{a} = \mathbf{a}_k | \mathbf{Z}(t_i) = \mathbf{Z}_i]$, i.e., the probability that the parameter value \mathbf{a}_k is the correct one for the model, based on the measurements collected up to this point $\mathbf{Z}(t_i) = \mathbf{Z}_i$.

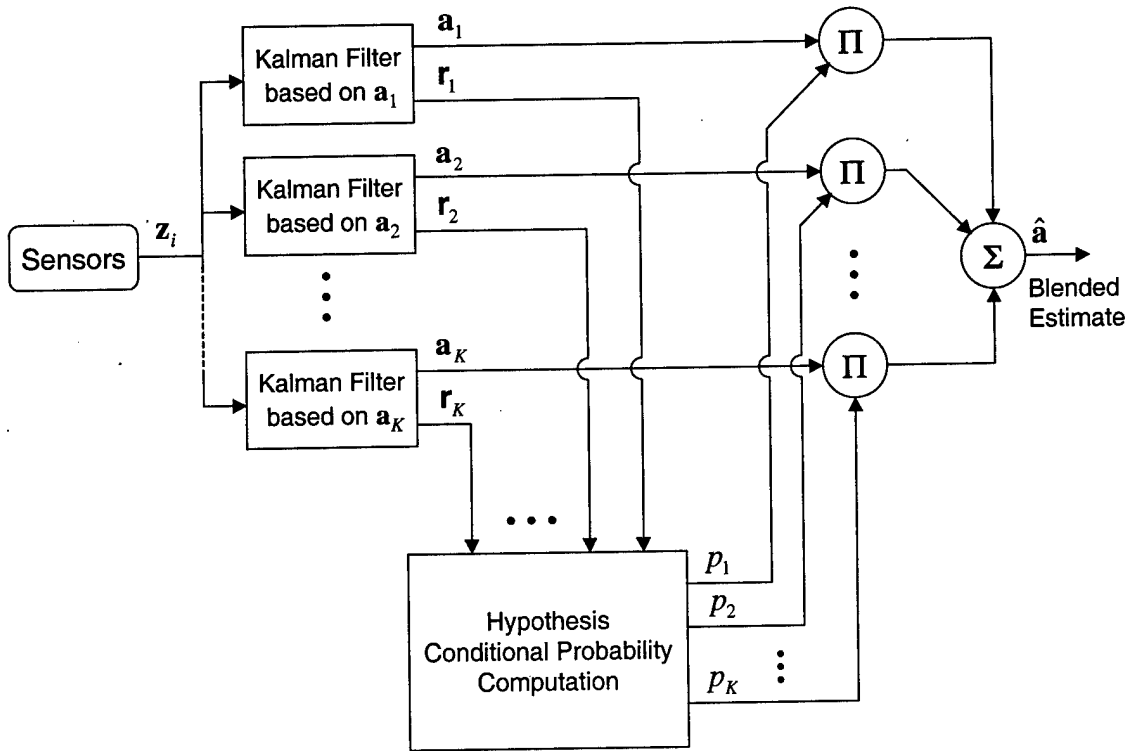


Figure 7. MMAE Structure for Parameter Estimation

The blended estimate is then the weighted mean of $\hat{\mathbf{x}}_k(t_i)$, $k = 1, 2, \dots, K$:

$$\hat{\mathbf{x}}(t_i) = E\{\mathbf{x}(t_i) | \mathbf{Z}(t_i) = \mathbf{Z}_i\} = \sum_{k=1}^K \hat{\mathbf{x}}_k(t_i) p_k(t_i) \quad (38)$$

The corresponding covariance $\mathbf{P}(t_i)$ of the blended solution is

$$\mathbf{P}(t_i) = \sum_{k=1}^K \{ \mathbf{P}_k(t_i) + [\hat{\mathbf{x}}_k(t_i) - \hat{\mathbf{x}}(t_i)][\hat{\mathbf{x}}_k(t_i) - \hat{\mathbf{x}}(t_i)]^T \} p_k(t_i) \quad (39)$$

The underlying concept of the MMAE is that values of the residuals determine which filter best represents the real-world system at the current time, i.e., the best filter has the smallest scaled residuals. These residuals are scaled by the inverse of the filter-computed residual covariance, as seen in Equation (37). The corresponding probability of that filter should increase over time and the other filters' probabilities should decrease, assuming the system environment remains constant. Prior to using the MMAE, each filter should be tuned (values of the dynamics pseudonoise strength matrix \mathbf{Q} adjusted) for its best performance by running the algorithms under the conditions of each of K parameter values being the best or "true" values in the real world. Thus, the k^{th} filter would be tuned for best performance when the "true" parameters are \mathbf{a}_k .

An inherent trade-off problem exists in an MMAE between state estimation ($\hat{\mathbf{x}}$) and parameter estimation ($\hat{\mathbf{a}}$). The problem is that the only way an MMAE can ascertain what the system parameters should be is through the measurements it receives. When an MMAE is designed to yield good state estimates (i.e., accurately predicting the system's actual states $\mathbf{x}(t_i)$ given all previous actual measurements \mathbf{Z}_{i-1} over a period of time) each filter is tuned individually to provide accurate state estimates for its own parameter value \mathbf{a}_k . If the filters are tuned conservatively, the residuals, $\mathbf{r}_k(t_i) = \mathbf{z}_i - \mathbf{h}[\hat{\mathbf{x}}_k(t_i^-), t_i]$, can appear similar to each other. If all the residuals tend to have nearly the same magnitude,

then the MMAE favors (assigns the highest probability to) the filter with the least value of $|\mathbf{A}_k|$, as shown by Equations (33) and (35) – (37). Although \mathbf{A}_k is used to represent the covariance of the residuals (assumed Gaussian), the value of $|\mathbf{A}_k|$ is independent of the residuals themselves and how well the k^{th} filter fits the parameter environment. The conditional probability of each filter $p_k(t_i)$ is dependent upon its residuals through $L_k(t_i)$ from Equation (37). If the scaled values of the residuals, $\mathbf{r}_k(t_i)$, are similar, then $L_1(t_i) \approx L_2(t_i) \approx \dots \approx L_K(t_i)$. This means that $p_k(t_i)$ is now highly dependent on $\beta_k(t_i)$ (2-32) which has as its only variable, $|\mathbf{A}_k(t_i)|$. A strong dependence on $|\mathbf{A}_k(t_i)|$ can distort the blending process since there will be one filter $j \in \{1, 2, \dots, K\}$, such that $|\mathbf{A}_j(t_i)| < |\mathbf{A}_k(t_i)| \forall k \neq j$. If the parameter environment does not change for a period, $p_j(t_i)$ will approach unity while all other $p_k(t_i)$ will approach zero. As this happens, one filter out of the bank becomes favored by having most of the probability weighting. This may be the “best” filter out of the choices available, though it may not have the best parameters out of the entire parameter space.

However, the performance of the algorithm relies upon significant differences between the residual characteristics of each elemental filter. Because of this, it is important to avoid adding too high levels of dynamics pseudonoise \mathbf{Q} during filter tuning. Although a conservative tuning philosophy is used to keep filter estimates from diverging considerably from the truth, conservative tuning tends to mask the differences between good and bad models [28, 33].

Another concern occurs when one of the elemental filters achieves a conditional probability of zero. Whenever this occurs, that filter’s probability remains zero

indefinitely due to the recursive nature of Equation (33). Thus, the filter is eliminated from the possible choices considered by the MMAE in the future. Even if the parameter conditions change such that the elemental filter that had zero-probability now represents the best model of the real-world system, that filter cannot have any probability weight assigned to it. One solution to prevent this from happening is to establish an artificial minimum threshold value that p_k can attain, i.e., $\min(p_k)$ [1, 31]. Consequently, this means no elemental filter can have $p_k = 1$ even if it is the exact match, though this should not produce any significant problems in determining a solution [31].

The advantage MMAE provides to Kalman filtering is that it handles situations where a single system model cannot sufficiently simulate the behavior of an actual system confronted with varying parameters. In addition to the states, the MMAE algorithm can be used to determine the best estimate of the parameters themselves $\hat{\mathbf{a}}(t_i)$ based on all the measurements collected $\mathbf{Z}(t_i) = \mathbf{Z}_i$. The blended estimate of the parameter set is calculated in the same manner as with the state vector:

$$\hat{\mathbf{a}}(t_i) = E\{\mathbf{a}(t_i) | \mathbf{Z}(t_i) = \mathbf{Z}_i\} = \sum_{k=1}^K \hat{\mathbf{a}}_k(t_i) p_k(t_i) \quad (40)$$

The conditional covariance of $\mathbf{a}(t_i)$ of the blended parameter estimate is

$$\begin{aligned} \mathbf{P}_a(t_i) &= E\{[\mathbf{a}(t_i) - \hat{\mathbf{a}}(t_i)][\mathbf{a}(t_i) - \hat{\mathbf{a}}(t_i)]^T | \mathbf{Z}(t_i) = \mathbf{Z}_i\} \\ &= \sum_{k=1}^K [\mathbf{a}_k(t_i) - \hat{\mathbf{a}}(t_i)][\mathbf{a}_k(t_i) - \hat{\mathbf{a}}(t_i)]^T p_k(t_i) \end{aligned} \quad (41)$$

When the filters are tuned for parameter estimation, it is done such that the residuals tend to have values sufficiently distant from each other. This helps to create a situation such that if the actual parameters do not exactly or closely match those of one of the filters, a blending of several filters will provide an accurate estimate of the parameters.

However, the method to make the residuals more distinct from each other entails applying smaller values of the Kalman filter gains $\mathbf{K}_k(t_i)$ to reduce the influence of the measurements \mathbf{z}_i . When the measurements have less influence, the filter tends to rely too heavily on the propagated state estimates $\hat{\mathbf{x}}(t_i^-)$. This means the actual state $\mathbf{x}(t_i)$ can be misrepresented over time. Therefore, new techniques have been developed to give accurate estimates of both the states and the parameters simultaneously [33].

2.4. Modified MMAE (M^3AE)

The M^3AE architecture combines MMAE and Kalman filter techniques for simultaneous state and parameter estimation. Under this architecture, an MMAE serves as the parameter estimator and is designed and tuned for estimating the system's uncertain parameters accurately. It is optimized for distinguishing among several possible hypothesized operating conditions dictating the parameters of the system. The separate single state estimator within the M^3AE algorithm is designed and tuned to provide accurate state estimation, conditioned on the measurements and knowledge of the parameters provided by the parameter estimator.

Several assumptions regarding the system must be accepted before an M^3AE can be applied to the model. Most importantly, the parameters to be estimated lie within a finite predefined parameter space. The elemental filters of the MMAE are then based on a subset of discrete parameter values chosen from the parameter space [31]. In addition, the variable parameters change more slowly than the system's states, thus estimates of these parameters can make use of any prior information available as to how they vary over time. As for designing an M^3AE architecture, Miller describes a straightforward

method to analyze, tune, and predict the system's performance before conducting a full-scale Monte Carlo analysis. Figure 8 shows a flowchart of the performance analysis tool.

First, a discretized parameter set is established using an algorithm designed by Sheldon to determine the parameters of each elemental filter of the MMAE [48, 33]. If appropriate, inter-residual distance feedback (IRDF) techniques developed by Lund [28] are applied to make each elemental filter appear more distinct from one another. Next, the state estimation Kalman filter is designed using techniques described by Maybeck [30, 31]. It is important to note that the MMAE will provide the values of the variable parameters to the state estimator based on the incoming measurements. Then, the MMAE and state estimator are coded in a software simulation. A single Monte Carlo run

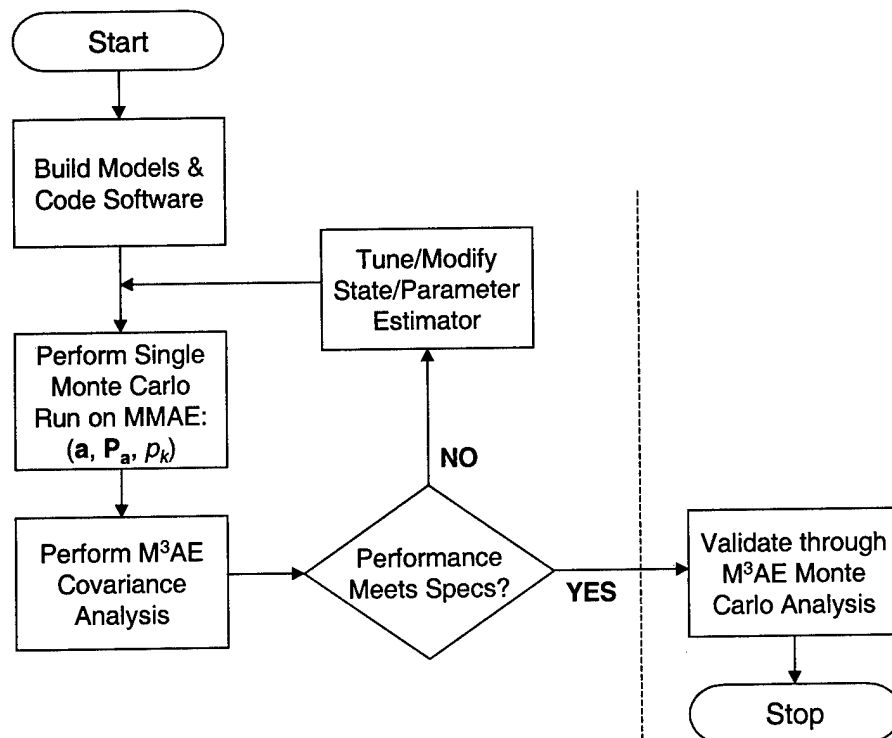


Figure 8. MMAE Structure

is performed on the MMAE to generate the values of the parameter estimate, $\hat{\mathbf{a}}(t_i)$, its covariance determined by the elemental filters, $\mathbf{P}_a(t_i)$, and the probabilities associated with each elemental filter $p_k(t_i)$. Finally, an approximate covariance analysis is conducted to verify if the design's performance meets the desired specifications. If so, a thorough Monte Carlo analysis is conducted on the M³AE. If not, the MMAE and the state estimator are modified iteratively to solve the discrepancies.

2.4.1. Parameter Space Discretization

The M³AE's MMAE is designed for accurate parameter estimation. When designing the MMAE for parameter estimation, a parameter space must be defined. The parameter space is the range of values the uncertain parameter to be estimated can assume. Once this is determined, the next issue is the placement of the elemental filters to span the space. In the past, several *ad hoc* methods were used to determine the placement or *discretization* of the parameter space, e.g., equal spacing, exponential spacing, etc. [15, 16, 31, 46, 49]. Sheldon[48, 49] thought a more systematic design approach was required, thus he developed a method to assign the placement of the filters optimally. His method involves minimizing a cost function, C , which is the average of the mean-squared estimation error taken over the parameter space:

$$C = \frac{\int_{\mathbf{R}} E\{[\mathbf{a}(t) - \hat{\mathbf{a}}(t)]^T \mathbf{W}[\mathbf{a}(t) - \hat{\mathbf{a}}(t)]\} d\mathbf{a}}{\int_{\mathbf{R}} d\mathbf{a}} \quad (42)$$

where

$$\int_{\mathbf{R}} d\mathbf{a} \equiv \int_{\mathbf{R}_N} \dots \int_{\mathbf{R}_2} \int_{\mathbf{R}_1} da_1 da_2 \dots da_N \quad (43)$$

$$\mathbf{a} = \begin{bmatrix} a_1 \\ a_2 \\ \vdots \\ a_N \end{bmatrix} \quad (44)$$

and \mathbf{W} is a weighting matrix chosen by the designer to emphasize specific states, N is the number of scalar parameters (dimension of \mathbf{a}), and \mathfrak{X} is the bounded region of the parameter space within which the parameters can take on values.

The parameter space discretization and placement of the elemental filters is accomplished before implementing the MMAE. This entails deciding which parameters can change, what the appropriate parameter spaces are, and where the elemental filters should be placed within the parameter space. Sheldon developed a five-step algorithm to minimize a cost function over a parameter space numerically. The first three steps consist of constructing the truth and filter models to represent the system, deciding the number of filters to be used, and determining the cost function (parameter, state, or control, but in the M³AE, the MMAE is only used for parameter estimation) of the parameter set to be employed. The fourth step is the core of the process. The basic purpose is to apply a numerical integration technique to evaluate the value of the cost function, C , over the parameter space \mathfrak{X} . Assuming the parameter set remains constant for a given problem, only the numerator of Equation (42) needs to be evaluated, and with \mathbf{W} often chosen as a diagonal matrix, it can be expressed as:

$$\int_{\mathfrak{X}} E\{[\mathbf{a}(t) - \hat{\mathbf{a}}(t)]^T \mathbf{W}[\mathbf{a}(t) - \hat{\mathbf{a}}(t)]\} d\mathbf{a} = \int_{\mathfrak{X}} \text{tr}\left(\mathbf{W} E\{[\mathbf{a}(t) - \hat{\mathbf{a}}(t)][\mathbf{a}(t) - \hat{\mathbf{a}}(t)]^T\}\right) d\mathbf{a} \quad (45)$$

where $\text{tr}(\bullet)$ is the trace of a square matrix (sum of its diagonal elements). For numerical integration, \mathfrak{X} is divided into a number of discrete intervals. At one point of each integration interval, a value for $\hat{\mathbf{a}}(t_i)$ is calculated in the following manner:

Sheldon defines a transformation matrix \mathbf{T} that converts true states (indicated by the subscript T) $\mathbf{x}_T(t_i)$ to filter states (no subscript T) $\mathbf{x}(t_i)$ in this way:

$$\mathbf{x}(t_i) = \mathbf{T}\mathbf{x}_T(t_i) \quad (46)$$

where $\mathbf{x}(t_i)$ is defined by the discrete-time system equation:

$$\mathbf{x}(t_{i+1}) = \Phi(t_{i+1}, t_i)\mathbf{x}(t_i) + \mathbf{G}_d(t_i)\mathbf{w}_d(t_i) \quad (47)$$

$$\Phi(t_{i+1}, t_i) = e^{\mathbf{F}(t_i)(t_{i+1}-t_i)} \quad (48)$$

and

$$\mathbf{G}_d(t_i)\mathbf{w}_d(t_i) = \int_{t_i}^{t_{i+1}} \Phi(t_{i+1}, \tau)\mathbf{G}(\tau)d\beta(\tau) \quad (49)$$

and $\mathbf{w}_d(t_i)$ is zero-mean WGN with strength (covariance) of $\mathbf{Q}_d(t_i)$:

$$\mathbf{Q}_d(t_i) = \int_{t_i}^{t_{i+1}} \Phi(t_{i+1}, \tau)\mathbf{G}(\tau)\mathbf{Q}(\tau)\mathbf{G}^T(\tau)\Phi^T(t_{i+1}, \tau)d\tau \quad (50)$$

The following equation is then solved iteratively, where the subscript, k , denotes the k^{th} filter corresponding to \mathbf{a}_k ($k = 1, 2, \dots, K$) (\mathbf{T} , as a subscript, still denotes the truth model):

$$\Gamma_k(n+1) = \mathbf{Y}\Gamma_k(n)\mathbf{Y}^T + \mathbf{G}_0\mathbf{Q}_0\mathbf{G}_0^T \quad (51)$$

where

$$\mathbf{Y} = \begin{bmatrix} \Phi_k(\mathbf{I} - \mathbf{K}_k\mathbf{H}_k) & (\Phi_k\mathbf{T} - \mathbf{T}\Phi_T) - \Phi_k\mathbf{K}_k(\mathbf{H}_k\mathbf{T} - \mathbf{H}_T) \\ \mathbf{0} & \Phi_T \end{bmatrix} \quad (52)$$

$$\mathbf{G}_0 = \begin{bmatrix} -\mathbf{T}\mathbf{G}_{dT} & \Phi_k\mathbf{K}_k \\ \mathbf{G}_{dT} & \mathbf{0} \end{bmatrix} \quad (53)$$

$$\mathbf{Q}_0 = \begin{bmatrix} \mathbf{Q}_{dT} & \mathbf{0} \\ \mathbf{0} & \mathbf{R}_T \end{bmatrix} \quad (54)$$

The iteration ends when $\Gamma_k(n)$ approaches a steady-state value, i.e., $\lim_{n \rightarrow \infty} \Gamma_k(n)$, (or practically when $\Gamma_k(n+1) \approx \Gamma_k(n)$), and is represented as Γ_k^∞ . The proximity of the k^{th} filter is defined as [49]:

$$\ell_k \equiv \ln|\mathbf{A}_k| + \text{tr} \left\{ \mathbf{A}_k^{-1} \left[\begin{bmatrix} \mathbf{H}_k & \mathbf{H}_k \mathbf{T} - \mathbf{H}_T \end{bmatrix} \Gamma_k^\infty \begin{bmatrix} \mathbf{H}_k & \mathbf{H}_k \mathbf{T} - \mathbf{H}_T \end{bmatrix}^T + \mathbf{R}_T \right] \right\} \quad (55)$$

If the MMAE has sufficient conditions to converge in the *Baram-sense* [3], it will converge toward the j^{th} filter governed by:

$$\ell_j = \min \{ \ell_k | k = 1, 2, \dots, K \} \quad (56)$$

Then the parameter is given by

$$\begin{aligned} \hat{\mathbf{a}}(t_i) &= \sum_{k=1}^K \mathbf{a}_k p_k(t_i) \\ &= \{ [1 - K p_{\min}] \mathbf{a}_j(t_i) \} + \sum_{k=1}^K \mathbf{a}_k(t_i^+) p_{\min} \end{aligned} \quad (57)$$

where p_{\min} is the pre-defined minimum conditional probability a filter can attain, and \mathbf{a}_j is the value of $\mathbf{a}(t_i)$ according to the j^{th} filter.

The fifth step is to use the values of $\hat{\mathbf{a}}(t_i)$ computed above in a vector minimization of $C(\mathbf{a})$. This yields the optimal values of \mathbf{a}_k for each filter.

This procedure applies to steady-state, constant-gain (i.e., $\mathbf{K}(t_i)$ does not vary over time) Kalman filter. This is adequate for time-invariant systems with stationary noise. In cases involving astable or unstable system model, the Kalman filters of the MMAE do not achieve a steady-state condition. This motivates the use of a *finite horizon*, the selecting of a period where the system parameters can be considered time-invariant [33]. This research uses an INS with time-varying parameters in its system dynamics matrix and an inherent instability in estimating vertical positions (a common trait of INSs).

Thus, a finite horizon is implemented in the software in the iterative solution of the Equation (51).

2.4.2. Inter-Residual Distance Feedback (IRDF)

Another concern in parameter estimation is to keep the values of $L_k(t_i)$ sufficiently distinct to avoid overdependence on $|\mathbf{A}_k(t_i)|$. To accomplish this, Lund [28, 29, 33] defines a quadratic term $J_{kj}(t_i)$ as the squared distance measure of the difference between residual $\mathbf{r}_k(t_i)$ and residual $\mathbf{r}_j(t_i)$:

$$J_{kj}(t_i) = \mathbf{r}_{kj}^T(t_i) \mathbf{\Psi}_{kj} \mathbf{r}_{kj}(t_i) \quad (58)$$

where $\mathbf{r}_{kj}(t_i) = \mathbf{r}_k(t_i) - \mathbf{r}_j(t_i)$, $j \neq k$, is the inter-residual distance between the k^{th} filter and the j^{th} filter, and $\mathbf{\Psi}_{kj}$ is a positive definite scaling matrix. The plan is to maintain $J_{kj}(t_i)$ above a specific limit value $J_0(t_i) > 0$ by adjusting the filter gains. A common method to accomplish this involves adjusting the filter gains by varying the dynamics noise strengths \mathbf{Q}_k *downward*. In the continuous-time method developed by Lund, \mathbf{Q}_k is replaced by

$$\mathbf{Q}'_k(t) = \eta(t) \mathbf{Q}_k(t), \quad \eta(t) \in [\eta_{\min}, 1] \quad (59)$$

Assuming \mathbf{Q}_k represents the dynamics noise for the k^{th} filter tuned for best estimation when its assumed parameter value is true, the modulating parameter $\eta(t)$ has an upper limit of 1, since $\eta(t) > 1$ would decrease the distinguishability of the residuals [28, 29, 33]. A lower limit $\eta_{\min} \geq 0$ is set to maintain the stability of the filter. In addition, Lund defines the continuous-time derivative of $\eta(t)$ as:

$$\frac{d}{dt} \eta(t) = \begin{cases} \xi[J_{kj}(t) - J_0(t)], & \text{Cond. 1} \\ 0, & \text{Cond. 2} \end{cases} \quad (60)$$

where

$$\begin{aligned} \text{Cond. 1: } & \eta(t) \in [\eta_{\min}, 1] \\ \text{Cond. 2: } & \eta(t) = \eta_{\min} \text{ AND } \xi[J_{kj}(t) - J_0(t)] < 0 \text{ OR} \\ & \eta(t) = 1 \text{ AND } \xi[J_{kj}(t) - J_0(t)] > 0 \end{aligned} \quad (61)$$

The constant ξ provides proper attenuation of the noise modified by $\eta(t)$. *Ad hoc* methods are used to determine the values of ξ , η_{\min} , and J_0 . Lund suggests choosing ξ such that $1/\xi$ is greater than the largest time constant of the elemental filters, and $\eta_{\min} = 0$ if the system maintains its stability [28, 29]. For J_0 , one *ad hoc* method involves performing a sample run before applying the IRDF techniques [29, 33]. An initial value for J_0 is chosen based on the actual values of J_{kj} observed, e.g., the mean value of J_{kj} . These values are then “tuned” in further simulations to verify the system performs within its requirements. However, there is a shortcoming in this method in that the modulated system noise strength $\mathbf{Q}'_k(t)$, being a function of time, is computed in real-time and cannot be determined in advance.

As a way around this, Lund recommends modulating the quantity $\mathbf{K}_k(t)\mathbf{r}_k(t)$ instead of $\mathbf{Q}_k(t)$ to simplify this for linear models:

$$\mathbf{K}'_k(t)\mathbf{r}_k(t) = \eta(t)\mathbf{K}_k(t)\mathbf{r}_k(t), \quad \eta(t) \in [\eta_{\min}, 1] \quad (62)$$

The primary benefit of this is that the Kalman filter gains $\mathbf{K}_k(t)$ can be precomputed and only $\eta(t)$ is computed in real-time [29, 33]. In addition, modulating $\mathbf{K}_k(t)$ yields quicker adaptation responses than with $\mathbf{Q}_k(t)$, which relies on the filter state covariance $\mathbf{P}_k(t)$ equations transient effects to subside before the filter gains can be changed [29, 33]. Conversely, Lund states this approach has less benefit for extended Kalman filter and other higher order filters where their filter gains are computed in the process. In this

research effort, the MMAE filters implemented have reasonably distant values when the parameter space is discretized by means of Sheldon's algorithm. Also, many of the terms of the system dynamics noise matrix Q for the truth model and tuned filter model are very small or zero. For these reasons, IRDF was not pursued in this work, although it may be of significant interest to other potential research areas [29, 33].

2.5. Summary

The theory and approaches described in this chapter are intended to provide insight into the methods used to implement system models for test simulations. Due to the extent Kalman filtering is applied to navigation problems, a good understanding of its workings can be invaluable in designing such systems. One of the motivations for this work is to apply the newly developed M^3AE techniques [33] to an actual problem, thus improving the capabilities of parameter estimation (prediction of the system's working environment), and state estimation (prediction of the values of concern, such as altitude). In this work, state estimation in the face of changing parameters for the precision landing problem is the core matter.

3. Methodology

3.1. Overview

The fundamental elements of this type of research effort are the application and implementation of accurate system models and simulations for the problem at hand. This chapter presents a comprehensive description of the truth and filter models, integration methods, and simulation techniques employed. An overall description of the system is provided at the start. Next, the truth and filter models are developed for each navigation subsystem, including a complete description of their roles. Finally, the approaches to perform simulations of the problem are outlined. The next chapter then gives a breakdown of the results of the simulations.

3.2. System Description

The navigation system to be examined consists of several elements. The basis for the system is the M³AE. Its role here is to provide the best estimates of the *error states* of the INS rather than the true states. *True states* are the actual values of position, velocity, attitude, etc. This should not be confused with the *truth* model, which is a system model that is assumed to depict the *actual* behavior of the states, *true* or *error*. Error states are distinguished from true states in that they are the correction values of position, velocity, etc. that should be subtracted from the states output from the INS to provide the best navigation estimates. This is necessary, since the INS, in the configuration being considered, does not have its states reinitialized to reflect an update on the actual position of the aircraft according to the measurement devices. Before the entire system is first

activated, the initial states of the INS are carefully calibrated to reflect the craft's current position, and the M^3 AE error states are assumed to be zero. After activation, the state estimator predicts how far INS readings deviate from the actual (true) position, attitude, and velocity of the craft, hence the term *error* states.

To compute its best estimate of these error states, the M^3 AE receives information from several sources. These consist of the INS with altitude estimation (*vertical channel*) aiding from a barometric altimeter, pseudoranges from four GPS satellites and one pseudolite, and relative altitude from a radar altimeter. The GPS signals and altimeter readings are considered as measurement values for the M^3 AE. The truth model uses 62 error states to describe how these systems function in the real world [7, 13, 38, 56]. Then, the reduced-order filter model's performance is compared to the truth model's performance. The filter model tracks 13 error states, representing the navigation system on board the aircraft. Figure 9 shows a layout of the relationships between subsystems. For the purposes of simulation, a flight profile trajectory was generated in advance by the program PROFGEN. The GPS satellite data used are from a file recorded 4 May 1991 [13].

The simulations compare the performance of the 13-state reduced-order filter to the 62-state truth model. The (error) states of the filter model are a proper subset of those of the truth model, and were chosen to be those having the greatest influence over the desired navigation data output of the complete system [38]. The truth model makes use of 39 states representing the INS and 23 states for the GPS data. From this group of states, 11 INS states and 2 GPS states were selected to be implemented into the filter model.

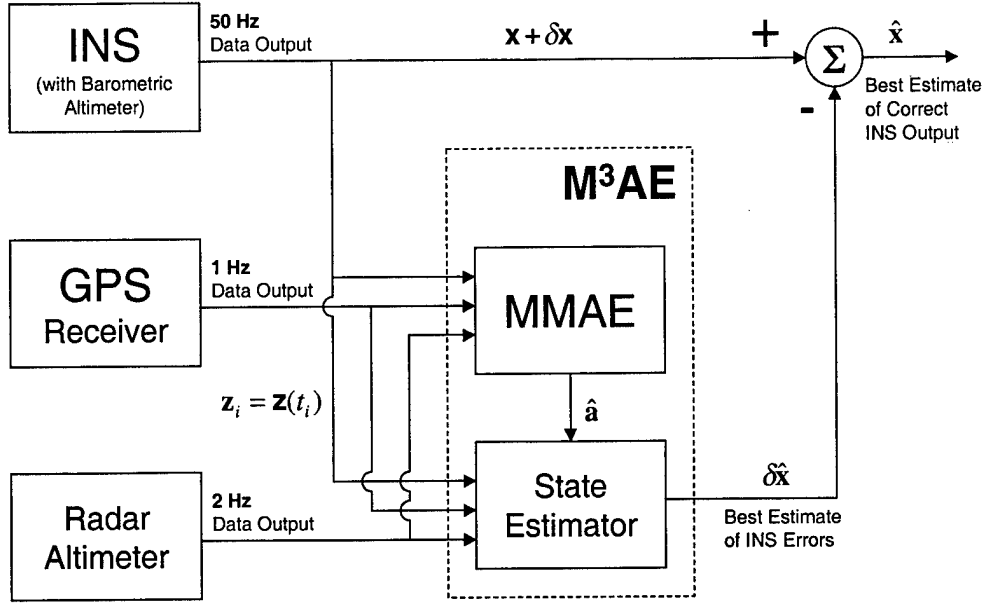


Figure 9. Navigation System Block Diagram

3.3. Inertial Navigation System Models

The INS model used in this work is based on the Litton LN-93 *strapdown, wander-azimuth* INS using accelerometers and ring-laser gyroscopes (RLG) to detect the changes in the motion and orientation of the aircraft. Readings from these instruments are translated into the various states of the model including position, velocity, and attitude. Litton developed a sophisticated error state model using 93 states to describe the characteristics of the LN-93 INS [26]. This error state model provides an accurate depiction of the actual performance characteristics of the INS and has been used in several research projects at the Air Force Institute of Technology (AFIT) [7, 13, 38, 56, 57]. The error state model has been implemented into the MMSOFE program [39, 36] to conduct the Monte Carlo simulations.

The error states of the LN-93 $\delta\mathbf{x}$ can be expressed as a 93-state vector that can be separated into six categories or “subvectors”.

$$\delta\mathbf{x} = [\delta\mathbf{x}_1^T \quad \delta\mathbf{x}_2^T \quad \delta\mathbf{x}_3^T \quad \delta\mathbf{x}_4^T \quad \delta\mathbf{x}_5^T \quad \delta\mathbf{x}_6^T]^T \quad (63)$$

$\delta\mathbf{x}_1$ has 13 elements representing the commonly used nine Pinson error states: position, velocity, and attitude in three dimensions; and four errors in the vertical channel of the INS [43].

$\delta\mathbf{x}_2$ has 16 elements representing the exponentially time-correlated errors of the gyros, accelerometers, and barometric altimeter, and “trend” states, all of which are treated as first-order Gauss-Markov processes.

$\delta\mathbf{x}_3$ has 18 elements representing gyroscopic bias errors, which are treated as random constants.

$\delta\mathbf{x}_4$ has 22 elements representing accelerometer bias errors, which are treated as random constants.

$\delta\mathbf{x}_5$ has six elements representing accelerometer and initial thermal transients, all of which are treated as first-order Gauss-Markov processes.

$\delta\mathbf{x}_6$ has 18 elements representing gyroscopic compliance errors, treated as biases.

The differential system equation for the INS truth model is

$$\delta\dot{\mathbf{x}} = \mathbf{F}\delta\mathbf{x} + \mathbf{G}\mathbf{w}$$

$$\begin{bmatrix} \delta\dot{\mathbf{x}}_1 \\ \delta\dot{\mathbf{x}}_2 \\ \delta\dot{\mathbf{x}}_3 \\ \delta\dot{\mathbf{x}}_4 \\ \delta\dot{\mathbf{x}}_5 \\ \delta\dot{\mathbf{x}}_6 \end{bmatrix} = \begin{bmatrix} \mathbf{F}_{11} & \mathbf{F}_{12} & \mathbf{F}_{13} & \mathbf{F}_{14} & \mathbf{F}_{15} & \mathbf{F}_{16} \\ \mathbf{0} & \mathbf{F}_{22} & \mathbf{0} & \mathbf{0} & \mathbf{0} & \mathbf{0} \\ \mathbf{0} & \mathbf{0} & \mathbf{0} & \mathbf{0} & \mathbf{0} & \mathbf{0} \\ \mathbf{0} & \mathbf{0} & \mathbf{0} & \mathbf{0} & \mathbf{0} & \mathbf{0} \\ \mathbf{0} & \mathbf{0} & \mathbf{0} & \mathbf{0} & \mathbf{F}_{55} & \mathbf{0} \\ \mathbf{0} & \mathbf{0} & \mathbf{0} & \mathbf{0} & \mathbf{0} & \mathbf{0} \end{bmatrix} \begin{bmatrix} \delta\mathbf{x}_1 \\ \delta\mathbf{x}_2 \\ \delta\mathbf{x}_3 \\ \delta\mathbf{x}_4 \\ \delta\mathbf{x}_5 \\ \delta\mathbf{x}_6 \end{bmatrix} + \mathbf{I}_{6 \times 6} \begin{bmatrix} \mathbf{w}_1 \\ \mathbf{w}_2 \\ \mathbf{0} \\ \mathbf{0} \\ \mathbf{0} \\ \mathbf{0} \end{bmatrix} \quad (64)$$

A complete description of the submatrices within \mathbf{F} is given in Appendix B.

3.3.1. INS Dynamics Truth Model

Although this 93-state model provides the most accurate depiction of the behavior of the LN-93 INS, there is a considerable computational burden involved by implementing this model directly. The work of Negast provides a reduced-order version of this and demonstrates it retains sufficient fidelity to the original for the types of simulations conducted here [38]. The reduced-order model, which is incorporated into this work, is:

$$\begin{bmatrix} \delta\dot{\mathbf{x}}_1 \\ \delta\dot{\mathbf{x}}_2 \\ \delta\dot{\mathbf{x}}_3 \\ \delta\dot{\mathbf{x}}_4 \end{bmatrix} = \begin{bmatrix} \mathbf{F}_{11} & \mathbf{F}_{12} & \mathbf{F}_{13} & \mathbf{F}_{14} \\ \mathbf{0} & \mathbf{F}_{22} & \mathbf{0} & \mathbf{0} \\ \mathbf{0} & \mathbf{0} & \mathbf{0} & \mathbf{0} \\ \mathbf{0} & \mathbf{0} & \mathbf{0} & \mathbf{0} \end{bmatrix} \begin{bmatrix} \delta\mathbf{x}_1 \\ \delta\mathbf{x}_2 \\ \delta\mathbf{x}_3 \\ \delta\mathbf{x}_4 \end{bmatrix} + \begin{bmatrix} \mathbf{w}_1 \\ \mathbf{w}_2 \\ \mathbf{0} \\ \mathbf{0} \end{bmatrix} \quad (65)$$

The states of this model are a validated subset of 93-state vector, though they are not the first 39 states of that vector. Thus, the submatrices within this equation are different from those in the previous equation since the error state subvectors do not correspond exactly to those above. The relationship between the states of the two models is provided in Appendix B.

3.3.2. INS Dynamics Filter Model

The model representing a typical implementation in a navigation computer installed on an aircraft would tend to be less complex than the full-scale truth model. Processing full-order models requires extensive computing capacity. Therefore, reduced-order models economize the limited computation resources normally available on board an aircraft and provide quick processing of results in real time. This encourages the development of a further reduced-order filter model. The filter model for the INS used in this research consists of 11 states: three position alignment errors, three velocity biases, three attitude alignment errors (related to the nine Pinson error states) [43], and two states for vertical channel stabilization. Since the ultimate goal is to obtain the most current and accurate information about the position and velocity of the craft, the states selected are those having the greatest influence on these quantities. All of these states are elements of $\delta\mathbf{x}_1$. Thus, the elements of the system dynamics matrix form a subset of the elements of \mathbf{F}_{11} . To compensate for the omission of states, the values of the strength of the dynamics noise matrix $\mathbf{Q}(t)$, where $E\{\mathbf{w}(t)\mathbf{w}^T(t + \tau)\} = \mathbf{Q}(t)\delta(\tau)$, $\tau = 0$, are tuned, i.e., adjusted, so that the behavior of the filter equation closely resembles that of the truth model. Appendix B gives a further description of these states and Appendix C lists the tuning values.

3.3.3. INS Measurement Filter Model

The measurement device directly incorporated into the INS is the barometric altimeter. The barometric altimeter provides signals to counteract the inherent instability of the vertical channel, i.e. altitude determination, of the INS. Since the M³AE uses error

states, the value of the true altitude (unknown) must be eliminated by taking the difference between the altitude predicted by the INS h_{INS} and the reading of the barometric altimeter h_{Bar} . The value of INS-predicted altitude h_{INS} is considered to be the sum of the true altitude h_T and the INS error in altitude above the reference ellipsoid of the earth (WGS-84 [9]), δh . The reference ellipsoid is used since barometric altimeters are calibrated to measure altitude above mean sea level, and not the actual terrain. The barometric altimeter reading is viewed as the sum of the true altitude h_T , the time-correlated error in the altitude reading δh_B , and a random noise in the measurement v_{Bar} , an element of the measurement noise vector \mathbf{v} . By taking the difference of the two altitude readings, the value of the true altitude is eliminated, thus:

$$\begin{aligned}\delta z_{Bar} &= h_{INS} - h_{Bar} \\ &= [h_T + \delta h] - [h_T + \delta h_B - v_{Bar}] \\ &= \delta h - \delta h_B + v_{Bar}\end{aligned}\tag{66}$$

The random noise v_{Bar} is considered to be zero-mean, discrete-time WGN, thus it can take on a positive or negative sign. The sign of v_{Bar} was chosen to yield a positive one in the final form of the equation to emphasize the *addition* of measurement noise. Two states from the filter model appear in this equation: the INS error in altitude above the reference ellipsoid δh and the time-correlated barometric altimeter error δh_B .

3.4. Radar Altimeter Measurement Model

Accurate and precise knowledge of altitude is vital to flying and landing an aircraft safely. Thus, an additional instrument, a radar altimeter, is commonly included on aircraft to determine altitude further. The radar altimeter readings h_{Rad} are modeled as merely the sum of the true altitude h_T and zero-mean WGN in the measurement v_{Rad} (note

the sign convention). The measurement error is calculated in the same manner as with the barometric altimeter:

$$\begin{aligned}
 \delta z_{Rad} &= h_{INS} - h_{Rad} \\
 &= [h_T + \delta h] - [h_T - v_{Rad}] \\
 &= \delta h + v_{Rad}
 \end{aligned} \tag{67}$$

Unlike the INS and barometric altimeter measurements, there are no time-correlated components associated with the radar altimeter measurements. However, the radar altimeter is sensitive to the relative altitude of the aircraft. Radar altimeters give better readings when closer to the surface terrain, “above ground level” (AGL), than at higher altitudes. Thus, radar altimeters are used regularly only when the relative altitude drops below 3,000 ft AGL. The precision dependence of the radar altimeter is reflected in the covariance of the measurement noise R_{Rad} as a function of the true AGL altitude h_{AGL} . This value is the same in both the truth and filter models and is given by [13]:

$$R_{Rad} = (0.01^2 h_{AGL}^2 + 0.25) \text{ ft}^2 \tag{68}$$

The quantity R_{Rad} is a diagonal element of the measurement noise matrix \mathbf{R} .

3.5. Global Positioning System Models

GPS is made up of a constellation of satellites sitting in six orbital planes revolving about the earth in an approximately 12-hour orbit. The constellation consists of a minimum of 24 satellites with several on-orbit spares. The satellites of GPS are designed to serve as a radionavigation system to provide three-dimensional positioning information with respect to the earth. Each GPS satellite or space vehicle (SV) broadcasts information about its own position in orbit at a specific time. GPS receivers on earth search for, acquire, and track signals broadcast from four or more SVs and process them

to determine their position relative to the earth. Since the position is calculated in three dimensions, at least four signals are needed to produce an unambiguous solution for position. The signal from each SV contains information identifying which satellite it is, what its position is according to its own ephemeris, what time this signal was broadcast, and other data specific to the SV. The key to using GPS signals for positioning is to determine the difference in time between when the SV sent the signal and when the receiver picked up the signal. Based on the predetermined velocity of radio frequency (RF) transmissions, this difference in time can be translated into a distance between the receiver and the satellite. This quantity is known as the *pseudorange*. A pseudorange differs from the true range between the receiver and SV in that it has several errors embedded into it due to timing inaccuracies and RF propagation delays. These errors are taken into account when determining a positioning solution for the receiver.

3.5.1. GPS Truth Models

The pseudoranges calculated from the receiver to each GPS satellite are subject to three primary categories of errors: errors due the receiver's internal clock, errors due to atmospheric effects, and errors due to each SV's equipment. Each error has the effect of increasing or decreasing the apparent pseudorange between the receiver and the transmitting satellite. Therefore, these errors have been studied widely and models have been constructed to describe and simulate their behavior accurately [25].

3.5.1.1. GPS Dynamics Model

The GPS truth model developed has been used with success by several research efforts at AFIT [7, 13, 38, 56, 57]. The 30 states used by the model are listed in

Appendix B. The first errors considered are the most significant, which involve the internal clock of the receiver. Although each SV in the GPS constellation possesses a high-accuracy atomic clock on-board, most receivers use less expensive clocks that do not keep time to the same degree. The difference between the time the receiver clock indicates and the actual time is represented by user's receiver clock bias δR_{Uclk} and clock drift rate δD_{Uclk} . The system dynamics equation relating these is:

$$\begin{bmatrix} \delta \dot{R}_{Uclk} \\ \delta \dot{D}_{Uclk} \end{bmatrix} = \begin{bmatrix} 0 & 1 \\ 0 & 0 \end{bmatrix} \begin{bmatrix} \delta R_{Uclk} \\ \delta D_{Uclk} \end{bmatrix} \quad (69)$$

The initial values of the state estimates and corresponding values of covariance were chosen to be consistent with past studies at AFIT [7, 13, 38, 56]:

$$\begin{bmatrix} \delta \hat{R}_{Uclk}(t_0) \\ \delta \hat{D}_{Uclk}(t_0) \end{bmatrix} = \begin{bmatrix} 0 \\ 0 \end{bmatrix} \quad (70)$$

$$\mathbf{P}_{Uclk}(t_0) = \begin{bmatrix} 9.0 \times 10^{14} \text{ ft}^2 & 0 \\ 0 & 9.0 \times 10^{10} \frac{\text{ft}^2}{\text{sec}^2} \end{bmatrix} \quad (71)$$

These errors are the same with respect to each satellite since they are produced by the receiver equipment. The next errors considered are associated with a particular satellite, denoted by the subscript $j \in \{1, 2, 3, 4\}$. Another error associated with GPS receivers is the multi-path error, δR_{MPj} , which is caused by stray signals reflected by surfaces near the receiver's location.

In addition, GPS signals, being RF, are subject to atmospheric interference delaying the transmission. There are two atmospheric errors modeled: the tropospheric delay δR_{tropj} and the ionospheric delay δR_{ionj} . The three errors cited above are all treated as first-order Markov processes with zero-mean WGN as shown by:

$$\begin{bmatrix} \delta \dot{R}_{MPj} \\ \delta \dot{R}_{tropj} \\ \delta \dot{R}_{ionj} \end{bmatrix} = \begin{bmatrix} -1 & 0 & 0 \\ 0 & -\frac{1}{500} & 0 \\ 0 & 0 & -\frac{1}{1,500} \end{bmatrix} \begin{bmatrix} \delta R_{MPj} \\ \delta R_{tropj} \\ \delta R_{ionj} \end{bmatrix} + \begin{bmatrix} \mathbf{w}_{MPj} \\ \mathbf{w}_{tropj} \\ \mathbf{w}_{ionj} \end{bmatrix} \quad (72)$$

with initial state covariances given by:

$$\mathbf{P}_{MP/Atm}(t_0) = \begin{bmatrix} 0.25 & 0 & 0 \\ 0 & 1.0 & 0 \\ 0 & 0 & 3.0 \end{bmatrix} \text{ft}^2 \quad (73)$$

and dynamics noise characteristics given by:

$$E\{\mathbf{w}_{GPS}(t)\} = \mathbf{0} \quad (74)$$

$$E\{\mathbf{w}_{GPS}(t)\mathbf{w}_{GPS}^T(t+\tau)\} = \mathbf{Q}_{GPS}\delta(\tau) = \begin{bmatrix} 0.5 & 0 & 0 \\ 0 & 0.004 & 0 \\ 0 & 0 & 0.004 \end{bmatrix} \frac{\text{ft}^2}{\text{sec}^2} \delta(\tau) \quad (75)$$

Although each GPS SV has a high-accuracy clock on-board, its time may not be set exactly. This introduces another error term known as the satellite clock bias δR_{Sclkj} . The last errors taken into account are the line-of-sight satellite position errors, δx_{SVj} , δy_{SVj} , and δz_{SVj} . These four errors are modeled thus:

$$\begin{bmatrix} \delta \dot{R}_{Sclkj} \\ \delta \dot{x}_{SVj} \\ \delta \dot{y}_{SVj} \\ \delta \dot{z}_{SVj} \end{bmatrix} = \mathbf{0}_{4 \times 4} \begin{bmatrix} \delta R_{Sclkj} \\ \delta x_{SVj} \\ \delta y_{SVj} \\ \delta z_{SVj} \end{bmatrix} \quad (76)$$

with initial state covariances given by:

$$\mathbf{P}_{Sclk/LOS}(t_0) = 25 \text{ft}^2 \mathbf{I}_{4 \times 4} \quad (77)$$

The full 30-state system dynamics equation is formed by taking the user's receiver clock equations and augmenting them with four versions of Equations (72) and (76), for each j^{th} satellite. Appendix B provides a description for the 30 states.

3.5.1.2. GPS Measurement Model

The principal measurements for a GPS receiver are the pseudoranges ρ_{GPSj} to each satellite. This can be expressed as the sum of the true range ρ_{Tj} plus all the errors described above and measurement noise v_{PRj} :

$$\rho_{GPSj} = \rho_{Tj} + \delta R_{MPj} + \delta R_{tropj} + \delta R_{ionj} + \delta R_{Sclkj} + \delta R_{Uclk} + v_{PRj} \quad (78)$$

The true range is always an unknown quantity, thus a measurement difference is calculated to eliminate it. This is carried out by computing the position of the craft (user's receiver) as indicated by the INS ρ_U and the satellite's position according to its ephemeris ρ_S . The difference, INS range, is given by:

$$\rho_{INS} = |\rho_U - \rho_S| = \left| \begin{bmatrix} x_U \\ y_U \\ z_U \end{bmatrix}^{ECEF} - \begin{bmatrix} x_S \\ y_S \\ z_S \end{bmatrix}^{ECEF} \right| \quad (79)$$

where *ECEF* indicates that all elements are expressed in the Earth-Centered, Earth-Fixed (ECEF) coordinate reference frame. The quantity ρ_{INS} also can be expressed as:

$$\rho_{INS} = \sqrt{(x_U - x_S)^2 + (y_U - y_S)^2 + (z_U - z_S)^2} \quad (80)$$

This equation for ρ_{INS} is a non-linear function of the craft and satellite positions. To create a linear expression from this, a Taylor series expansion is calculated about a nominal value of both positions with the terms greater than first-order neglected.

This yields the equation:

$$\rho_{INS} = \rho_T + \left(\frac{\partial \rho_{INS}(\rho_S, \rho_U)}{\partial \rho_S} \right)_{(\rho_S, \rho_U)_{nom}} \delta \rho_S + \left(\frac{\partial \rho_{INS}(\rho_S, \rho_U)}{\partial \rho_U} \right)_{(\rho_S, \rho_U)_{nom}} \delta \rho_U \quad (81)$$

Substituting Equation (80) into Equation (81) and evaluating the partial derivatives produces:

$$\begin{aligned}\rho_{INS} = \rho_T - & \left(\frac{x_S - x_U}{|R_{INS}|} \right) \delta x_U - \left(\frac{y_S - y_U}{|R_{INS}|} \right) \delta y_U - \left(\frac{z_S - z_U}{|R_{INS}|} \right) \delta z_U \\ & + \left(\frac{x_S - x_U}{|R_{INS}|} \right) \delta x_S + \left(\frac{y_S - y_U}{|R_{INS}|} \right) \delta y_S + \left(\frac{z_S - z_U}{|R_{INS}|} \right) \delta z_S\end{aligned}\quad (82)$$

The measurement difference equation is formed by taking the difference between Equation (82) and Equation (78) for each satellite:

$$\begin{aligned}\delta z_{PRj} = \rho_{INSj} - \rho_{GPSj} \\ = - \left(\frac{x_S - x_U}{|R_{INS}|} \right) \delta x_U - \left(\frac{y_S - y_U}{|R_{INS}|} \right) \delta y_U - \left(\frac{z_S - z_U}{|R_{INS}|} \right) \delta z_U \\ + \left(\frac{x_S - x_U}{|R_{INS}|} \right) \delta x_S + \left(\frac{y_S - y_U}{|R_{INS}|} \right) \delta y_S + \left(\frac{z_S - z_U}{|R_{INS}|} \right) \delta z_S \\ - \delta R_{MPj} - \delta R_{tropj} - \delta R_{ionj} - \delta R_{Sclkj} - \delta R_{Uclk} + v_{PRj}\end{aligned}\quad (83)$$

Thus, the values of the receiver position errors, δx_U , δy_U , and δz_U , can be derived from the first three states, $\delta \theta_x$, $\delta \theta_y$, and $\delta \theta_z$, of the truth or filter model through an orthogonal transformation [7, 13].

3.5.2. Differential GPS Truth Models

As seen in the previous section, GPS pseudorange data contain errors from many different sources. A commonly used technique to eliminate some of these errors is known as *Differential GPS* (DGPS). To apply this technique, two GPS receivers are required. The first receiver, known as the reference receiver, is located at a site whose position is well surveyed and known to a high degree of accuracy. The reference receiver is usually equipped with a high-accuracy clock to diminish the receiver clock bias and drift. By comparing its GPS-computed position with its surveyed position, the reference receiver can obtain a precise estimate of the errors in the pseudoranges to each visible

satellite. For example, certain errors, such as the error in the position of the SV and satellite clock bias, are common between receivers that are relatively close by (within approximately 100 nmi). These errors then may be calibrated and transmitted to another remote receiver, e.g., on-board an aircraft, in the vicinity of the reference receiver. The transmitted error data provide differential corrections for the use by the remote receiver to remove them from its pseudorange calculation. Using DGPS, the truth model can be reduced to 26 states by disregarding the satellite clock biases δR_{Sclkj} for each satellite. In addition, there is difficulty in consistently characterizing the multi-path error, δR_{MPj} , since it is highly dependent upon the location of the receiver. Therefore, for the simulations performed in this research, δR_{MPj} is lumped into the measurement noise, v . Thus, the final DGPS truth model used consists of 22 states.

3.5.2.1. DGPS Dynamics Model

The system dynamics equation for the receiver clock bias and drift remains unchanged as in Equations (69), (70), and (71). Grouping the remaining atmospheric and satellite position errors, the system dynamics equation becomes:

$$\begin{bmatrix} \delta \dot{R}_{tropj} \\ \delta \dot{R}_{ionj} \\ \delta \dot{x}_{svj} \\ \delta \dot{y}_{svj} \\ \delta \dot{z}_{svj} \end{bmatrix} = \begin{bmatrix} -\frac{1}{500} & 0 & 0 & 0 & 0 \\ 0 & -\frac{1}{1,500} & 0 & 0 & 0 \\ 0 & 0 & 0 & 0 & 0 \\ 0 & 0 & 0 & 0 & 0 \\ 0 & 0 & 0 & 0 & 0 \end{bmatrix} \begin{bmatrix} \delta R_{tropj} \\ \delta R_{ionj} \\ \delta x_{svj} \\ \delta y_{svj} \\ \delta z_{svj} \end{bmatrix} + \begin{bmatrix} w_{tropj} \\ w_{ionj} \\ 0 \\ 0 \\ 0 \end{bmatrix} \quad (84)$$

with initial state covariances given by:

$$\mathbf{P}_{DGPS}(t_0) = \begin{bmatrix} 1.0 & 0 & 0 & 0 & 0 \\ 0 & 1.0 & 0 & 0 & 0 \\ 0 & 0 & 0.35 & 0 & 0 \\ 0 & 0 & 0 & 0.35 & 0 \\ 0 & 0 & 0 & 0 & 0.35 \end{bmatrix} \text{ft}^2 \quad (85)$$

and dynamics noise characteristics given by:

$$E\{\mathbf{w}_{DGPS}(t)\} = \mathbf{0} \quad (86)$$

$$E\{\mathbf{w}_{DGPS}(t)\mathbf{w}_{DGPS}^T(t+\tau)\} = \mathbf{Q}_{DGPS}\delta(\tau) = \begin{bmatrix} 0.001 & 0 & 0 & 0 & 0 \\ 0 & 0.0004 & 0 & 0 & 0 \\ 0 & 0 & 0 & 0 & 0 \\ 0 & 0 & 0 & 0 & 0 \\ 0 & 0 & 0 & 0 & 0 \end{bmatrix} \frac{\text{ft}^2}{\text{sec}^2} \delta(\tau) \quad (87)$$

3.5.2.2. DGPS Measurement Model

The DGPS pseudorange measurement equation is identical in form to Equation (78)

less the range errors due to multi-path and satellite clock bias:

$$\rho_{DGPSj} = \rho_{Tj} + \delta R_{tropj} + \delta R_{ionj} + \delta R_{Uclk} - v_{PRj} \quad (88)$$

The DGPS measurement difference equation is formed in the same manner as previously seen. In this case, the difference between Equation (82) and Equation (88) is taken for each satellite:

$$\begin{aligned} \delta z_{PRj} &= \rho_{INSj} - \rho_{DGPSj} \\ &= -\left(\frac{x_S - x_U}{|R_{INS}|}\right)\delta x_U - \left(\frac{y_S - y_U}{|R_{INS}|}\right)\delta y_U - \left(\frac{z_S - z_U}{|R_{INS}|}\right)\delta z_U \\ &\quad + \left(\frac{x_S - x_U}{|R_{INS}|}\right)\delta x_S + \left(\frac{y_S - y_U}{|R_{INS}|}\right)\delta y_S + \left(\frac{z_S - z_U}{|R_{INS}|}\right)\delta z_S \\ &\quad - \delta R_{tropj} - \delta R_{ionj} - \delta R_{Uclk} + v_{PRj} \end{aligned} \quad (89)$$

3.5.3. DGPS Filter Models

The simulations conducted in this work utilize DGPS to take advantage of the higher accuracy. Of all the errors discussed, the predominant errors are the receiver clock bias δR_{Uclk} and clock drift $\delta \dot{R}_{Uclk}$. The other errors are combined and modeled as zero-mean WGN resulting in this system dynamics equation:

$$\begin{bmatrix} \delta \dot{R}_{Uclk} \\ \delta \dot{D}_{Uclk} \end{bmatrix} = \begin{bmatrix} 0 & 1 \\ 0 & 0 \end{bmatrix} \begin{bmatrix} \delta R_{Uclk} \\ \delta D_{Uclk} \end{bmatrix} + \begin{bmatrix} w_{Uclk} \\ w_{Uclk} \end{bmatrix} \quad (90)$$

with an initial covariance given by:

$$\mathbf{P}_{Uclk}(t_0) = \begin{bmatrix} 9.0 \times 10^{14} \text{ ft}^2 & 0 \\ 0 & 9.0 \times 10^{10} \frac{\text{ft}^2}{\text{sec}^2} \end{bmatrix} \quad (91)$$

To get the filter model to emulate the behavior of the truth model, the elements of the dynamics noise matrix $\mathbf{Q}(t)$ are tuned in the filter. These tuning values are listed in Appendix C.

The measurement equation for the filter is similar to the other filter equations except several states are omitted: the multi-path effects, atmospheric effects, satellite clock biases, and satellite position errors from the ephemerides. With only the error in the craft's (receiver's) position and receiver clock bias and drift remaining, the filter measurement equation works out to be:

$$\begin{aligned} \delta z_{PRj} &= \rho_{INSj} - \rho_{DGPSj} \\ &= -\left(\frac{x_S - x_U}{|R_{INS}|}\right) \delta x_U - \left(\frac{y_S - y_U}{|R_{INS}|}\right) \delta y_U - \left(\frac{z_S - z_U}{|R_{INS}|}\right) \delta z_U - \delta R_{Uclk} + v \end{aligned} \quad (92)$$

The strength of the measurement noise is adjusted to compensate for the eliminated states. The four diagonal elements of the measurement noise matrix \mathbf{R} pertaining to the pseudorange measurements $R_{PRj}, j \in \{1, 2, 3, 4\}$ are tuned for optimal performance.

3.5.4. GPS Pseudolite Models

The pseudorange measurements for the ground-based pseudolite are treated as if they were received from a fifth GPS satellite ($j = 5$), with three exceptions pertaining to the truth model:

1. The atmospheric effects on pseudolite transmissions are caused only by the troposphere, since the pseudolite is on the ground. Thus, there is no ionospheric delay error term δR_{ion5} present, only a tropospheric term δR_{trop5} .
2. The pseudolite is assumed to be located at a surveyed site, eliminating the uncertainty in the satellite position from its ephemeris: δx_{SV5} , δy_{SV5} , δz_{SV5} .
3. The pseudolite is equipped with a high-accuracy clock, thus clock bias δR_{clk5} may be ignored.

Otherwise, for the filter model, there are no differences between a satellite measurement and a pseudolite measurement that need to be taken into account.

3.6. Integrated System Models

The models implemented into the simulations are a combination of those described above. The state vector of the entire system is constructed so the first 13 states of the truth state vector form the filter state vector. The remaining states for the truth model are augmented afterwards, in the following format:

$$\delta \mathbf{x}_{Truth} = \begin{bmatrix} \delta \mathbf{x}_{INS\ Filter} \\ \delta \mathbf{x}_{DGPS\ Filter} \\ \delta \mathbf{x}_{INS\ Other} \\ \delta \mathbf{x}_{DGPS\ Other} \end{bmatrix} \begin{array}{l} 11\ INS\ Filter\ States \\ 2\ DGPS\ Filter\ States \\ Other\ 28\ INS\ States \\ Other\ 21\ DGPS\ States \end{array} \quad (93)$$

The elements of the system dynamics matrix \mathbf{F} and the dynamics noise strength matrix \mathbf{Q} are arranged to maintain the state relationship so the system dynamics equation for the truth model in terms of the filter model is:

$$\begin{bmatrix} \delta \dot{\mathbf{x}}_{Filter} \\ \delta \dot{\mathbf{x}}_{Other} \end{bmatrix} = \begin{bmatrix} \mathbf{F}_{Filter} & \mathbf{F}_{Other(1,2)} \\ \mathbf{F}_{Other(2,1)} & \mathbf{F}_{Other(2,2)} \end{bmatrix} \begin{bmatrix} \delta \mathbf{x}_{Filter} \\ \delta \mathbf{x}_{Other} \end{bmatrix} + \begin{bmatrix} \mathbf{w}_{Filter} \\ \mathbf{w}_{Other} \end{bmatrix} \quad (94)$$

and the noise strength is:

$$E\{\mathbf{w}_{Truth}(t)\mathbf{w}_{Truth}^T(t+\tau)\} = \mathbf{Q}_{Truth}(t)\delta(\tau) = \begin{bmatrix} \mathbf{Q}_{Filter} & \mathbf{0} \\ \mathbf{0} & \mathbf{Q}_{Other} \end{bmatrix} \delta(\tau) \quad (95)$$

All of the dynamics noise for each state is considered to be independent of (uncorrelated with) each other. Therefore, all of the matrices representing the strength of the dynamics noise, \mathbf{Q}_{Truth} , \mathbf{Q}_{Filter} , and \mathbf{Q}_{Other} , are diagonal.

The measurement vector, $\delta \mathbf{z} = [\delta z_{Bar} \ \delta z_{PR1} \ \cdots \ \delta z_{PR4} \ \delta z_{Rad} \ \delta z_{PR5}]^T$, remains the same for both the truth model and the filter since there is no reduction in the number of measurement sources from the truth model to the filter. Conversely, the measurement noise covariance matrix, \mathbf{R} , does have different values between the truth model and the filter to reflect the reduction of states from the truth model to the filter. In addition, the measurement matrix, \mathbf{H} , is structured to fit the state vector convention. Thus, the measurement equation for the truth model in terms of the filter is:

$$\delta \mathbf{z} = \begin{bmatrix} \mathbf{H}_{Filter} & \mathbf{H}_{Other} \end{bmatrix} \begin{bmatrix} \delta \mathbf{x}_{Filter} \\ \delta \mathbf{x}_{Other} \end{bmatrix} + \mathbf{v} \quad (96)$$

and a measurement noise strength of:

$$E\{\mathbf{v}(t_i)\mathbf{v}^T(t_j)\} = \mathbf{R}(t_i)\delta_{ij} = \begin{bmatrix} R_{Bar} & 0 & 0 & \cdots & 0 & 0 \\ 0 & R_{PR1} & 0 & \cdots & 0 & 0 \\ 0 & 0 & \ddots & \ddots & \vdots & \vdots \\ \vdots & \vdots & \ddots & R_{PR4} & 0 & 0 \\ 0 & 0 & \cdots & 0 & R_{Rad} & 0 \\ 0 & 0 & \cdots & 0 & 0 & R_{PR5} \end{bmatrix} \delta_{ij} \quad (97)$$

where δ_{ij} is the Kronecker delta function.

3.7. Interference Models

The environment in which an aircraft travels is filled with many sources of RF signals, especially near the ground. Although GPS is a highly accurate system for determining positions with respect to the earth, it processes RF signals with a very low carrier-to-noise ratio, -163 dB_W [25]. These signals may be subjected to interference from various sources ranging from unintentional spurious emissions to malicious disruption on or near the GPS frequency band. In these simulations, this is reflected by an increase in the elements of the measurement noise matrix $\mathbf{R}(t_i)$ related to the pseudorange measurements. This variation in $\mathbf{R}(t_i)$ represents a change in the parameter structure of the system $\mathbf{a}(t_i)$. Accounting for this change while generating the appropriate state estimates is the role of the M³AE. The variable elements $R_{PRj}(t_i)$ of $\mathbf{R}(t_i)$ will have a finite range, i.e., parameter space, since beyond a certain level of interference, GPS signal are effectively unusable. The MMAE is designed to have filters spanning this finite parameter space, and to be optimized for estimating the actual value of $\mathbf{R}(t_i)$ based on the measurements available up to the time in question, $\mathbf{Z}(t_i) = [\mathbf{z}^T(t_i) \ \mathbf{z}^T(t_{i-1}) \ \cdots \ \mathbf{z}^T(t_0)]^T$. No changes in the measurement noise for the altimeters, $R_{Bar}(t_i)$ and $R_{Rad}(t_i)$, are taken in

account. The barometric altimeter is affected only by the atmospheric pressure and the radar altimeter has a narrow field of reception directed downward. In addition, the INS is a self-contained piece of equipment influenced only by the linear and angular accelerations of the craft. With a feed-forward configuration in place, the only measurement the INS receives is from the barometric altimeter incorporated within itself.

3.8. Simulation Software

The FORTRAN-based software, Multimode Simulation for Optimal Filter Evaluation (MSOFE), is a program constructed for conducting simulations of systems that employ Kalman filtering [36]. The structure of MSOFE allows it to be directly applied to a variety of problems requiring optimal state estimation with a minimal amount of software refitting. The program has two principal simulation modes for assisting in evaluating the performance of the system:

1. *Monte Carlo simulation* generates multiple-sample time histories of a system's truth states, filter states, and filter estimation errors, including non-linear effects, using linear or extended Kalman filtering.
2. *Covariance simulation* generates time histories of the second-order statistics, i.e., values of covariance, of a system's truth states, filter states, and filter estimation errors using only linear or linearized models.

The two modes are complementary. Covariance simulation can generate the performance statistics of a filter in a single pass. Monte Carlo simulation requires multiple sample runs before meaningful statistics can be computed for a scenario.

Conversely, Monte Carlo simulation can handle non-linear processes, which the covariance mode cannot.

An extension of MSOFE, Multiple Model Simulation for Optimal Filter Evaluation (MMSOFE), developed by Nielsen [39], supports the analysis of systems using multiple model adaptive estimation. MMSOFE is a modified version of MSOFE using similar core code with modifications reflecting the use of multiple Kalman filters. It is designed to conduct the propagation and update of several filters simultaneously. While performing the filter operations, it performs the calculations for hypothesis conditional probability and appropriate blending for MMAE and other multiple model algorithms. In this work, MMSOFE is used in the Monte Carlo mode for all simulations.

3.9. Parameter Estimation

The navigation system models are implemented using the M^3 AE architecture with an MMAE consisting of five elemental filters, delivering parameter updates to a state estimator. Five was chosen to give a finer discretization of the parameter space than in the previous research by White [56], but to keep the simulation time needed to a manageable level. The estimated parameter is the GPS pseudorange measurement noise strength, $R_{PRj}, j \in \{1, 2, 3, 4, 5\}$. This noise is assumed to affect all pseudorange measurements uniformly, thus $R_{PRi} = R_{PRj} \forall i \neq j$. Although the values of R_{PR} (j subscript dropped for simplicity) are meant to portray an increase in the strength of the RF interference noise on the GPS L1 frequency, it is not an accurate representation of an increase in the noise *power*. Still, varying R_{PR} serves to demonstrate a meaningful change in a parameter.

The greatest admissible value of pseudorange measurement noise variance is set as 2,000 times the nominal value of R_{PR} without RF interference (R_{PRO}) [56]. Any value greater than this is assumed to render GPS signals useless. Thus, the finite parameter space, \aleph , can be defined to encompass the real numbers from 1 to 2,000 and the estimated parameter vector, \mathbf{a} , is actually a scalar quantity, $a \in \aleph$. The value of a can be treated then as a multiplier to R_{PRO} , which in past research at AFIT was taken to be 9 (ft²) [38]. With \aleph and a defined, the placement of the elemental MMAE filters can be determined. Using the algorithm developed by Sheldon [48] described in Section 2.4.1., the values of a (instead of \mathbf{a} , since this quantity is not stochastic) for each of the five filters was calculated as follows:

$$\begin{aligned} a_1 &= 1.0 \\ a_2 &= 214.4 \\ a_3 &= 610.7 \\ a_4 &= 1,064.3 \\ a_5 &= 1,629.4 \end{aligned}$$

In addition, a constrained optimization was implemented into the enhanced Sheldon algorithm to fix one of the filters to the nominal parameter level, a_1 .

During each Monte Carlo run, three programs are used. First, the program MMSOFE runs the MMAE filters to calculate its best estimate of the pseudorange measurement noise strength factor, $\hat{a}(t_i) = E\{a(t_i) | \mathbf{Z}(t_i) = \mathbf{Z}_i\}$, at each time interval over the entire flight trajectory in question. This value of \hat{a} is then appended to the flight trajectory data using the program APPEND and passed on to the state estimator to be incorporated into its measurement noise matrix, \mathbf{R} , by letting $R_{PRj} = \hat{a}R_{PRO}$. Next, the state estimator calculates its best estimate of the states, $\hat{\mathbf{x}}$, from which the best estimate of the error in the aircraft's position is calculated at each time interval. Like the MMAE, the state

estimator is implemented into MMSOFE (a variation called SMSOFE) with certain variations, e.g., the number of filters is set to one. SMSOFE has the same basic structure as MMSOFE, except it has only one filter that accepts a parameter update generated by the MMAE (implemented in MMSOFE). After SMSOFE is run, the error in the aircraft's position (east, north, and vertical directions) over the trajectory is recorded. Ten Monte Carlo runs are performed to obtain sufficient data for a meaningful analysis. Finally, these data are processed using programs written in Matlab[®] [52] to create plots of the errors over the time of the trajectory.

3.10. Summary

The models described in this chapter are employed for simulating an integrated GPS/INS aircraft navigation system augmented with a radar altimeter and a signal available from a GPS pseudolite. A reduced-order filter model is constructed using a subset of the states from the system truth model. This is done to model the difference between the predictions an on-board navigation computer (filter model) would make of the position of the aircraft against actual behavior of the craft (truth model). In Chapter 4, the performance of the system is analyzed through various levels of interference to determine its suitability for a PLS.

4. Analysis of Results

This chapter covers the simulations conducted and provides interpretations of the results. Eight test cases are presented, depicting two navigation system configurations and four GPS interference scenarios. The M³AE algorithm is implemented for each case, where the MMAE is set up to determine the variable parameter in the presence of interference and the state estimator provides the best estimate of the position of the aircraft.

4.1. Flight Profile

The simulations were performed using the MMSOFE program working with a flight trajectory created by PROFGEN [35]. The flight profile created represents a KC-135 (Boeing 707) aircraft flying for 3,912.5 seconds from take-off to landing touch-down at runway 23R (heading 232°) at Patterson Field, Wright-Patterson AFB. The portion of the flight profile examined is the period just before landing, from 3,810 to 3,910 seconds, when the aircraft is on its 3° descent glideslope with a steady velocity of 132 knots [13]. The local terrain is assumed to be “flat”, at an altitude of 825 ft from mean sea level (MSL). The coordinates of the flight path are shown in Figure 10.

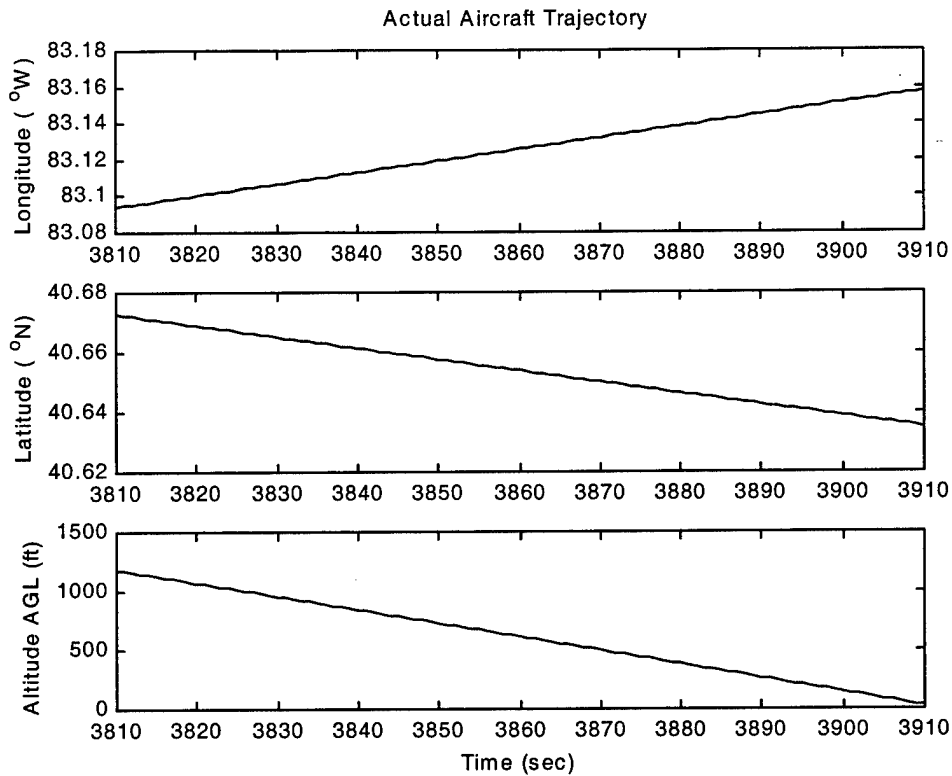


Figure 10. Actual Trajectory of the Simulated Landing Aircraft

4.2. GPS Data

To determine the pseudorange measurements, actual GPS almanac data were incorporated into the simulations. The almanac data were obtained from the Coast Guard Bulletin Board Services (CGBBS). A program called SEM3.6 [13] processed this information to select the four best GPS satellites of those visible, based on the best geometry, i.e., geometric dilution-of-position (GDOP). An arbitrary take-off time and date, 04:00 UTC (08:00 EDT), 21 May 1994, and a mask angle of 5° above the horizon, were used to determine which GPS satellites would be visible for the flight trajectory.

4.3. Navigation System Configurations

The navigation systems modeled in this study follows the work of previous [7, 13, 38, 56] and current [53, 57] research at AFIT. The core of the system is an INS with a barometric altimeter built-in for vertical channel aiding. To compare the effects of the quality of the INS used, two models were used, an INS with a drift rate of 0.4 nmi/hr (CEP) vs. a lower quality INS with a drift rate of 4.0 nmi/hr (CEP). The positioning ability of the INS is enhanced with pseudorange measurements provided by a GPS receiver. The receiver accepts signals from the four best GPS satellites visible and from a ground-based GPS pseudolite. The pseudolite is included to improve the vertical positioning of GPS. This is reflected in a lower (better) value of GDOP; 2.63 without the pseudolite vs. 2.50 using the pseudolite [25]. Finally, a radar altimeter is incorporated to improve altitude readings further; this is a navigation aid found in most military and commercial aircraft for use in landing.

4.4. GPS RF Interference Scenarios

The navigation systems modeled in this study follows the work of previous research by Gray, Britton, and White. Gray examined different combinations of navigation aids, first introducing different qualities of INS: 0.4 nmi/hr, 2.0 nmi/hr, and 4.0 nmi/hr drift rates. Britton followed this by incorporating DGPS in place of ordinary GPS pseudorange measurements. White applied RF interference and GPS spoofing to some of the past test cases to assess the performance of an MMAE to provide accurate state estimates.

The simulations performed for this effort use four different schemes of RF interference to examine the performance of the M³AE design described in previous chapters. The first has no interference to establish a nominal reference. The second uses the same scheme applied by White in his research, which consists of varying the parameter, a , at different levels spaced as shown in the top plot of Figure 11. The third scheme attempts to portray a situation where the interference increases as the aircraft approaches the touch-down point. Here, the source is assumed to be in the flight path of the aircraft. The value of a is increased in inverse proportion to the square of the distance to the interference source. In the fourth scheme, the value of a is decreased in the same manner to depict flying away from an RF interference source. The four RF interference scenarios are combined with the two navigation configurations to form eight test cases. Table 3 summarizes the test cases and Figure 11 shows the RF interference schemes where the parameter a varies.

Table 3. Simulation Test Cases

| Case | Drift Rating of INS Used | RF Interference Scheme |
|-------------|---------------------------------|-------------------------------|
| I | 0.4 nmi/hr | Nominal |
| II | 4.0 nmi/hr | Nominal |
| III | 0.4 nmi/hr | White's ("Exponential") |
| IV | 4.0 nmi/hr | White's ("Exponential") |
| V | 0.4 nmi/hr | Increasing |
| VI | 4.0 nmi/hr | Increasing |
| VII | 0.4 nmi/hr | Decreasing |
| VIII | 4.0 nmi/hr | Decreasing |

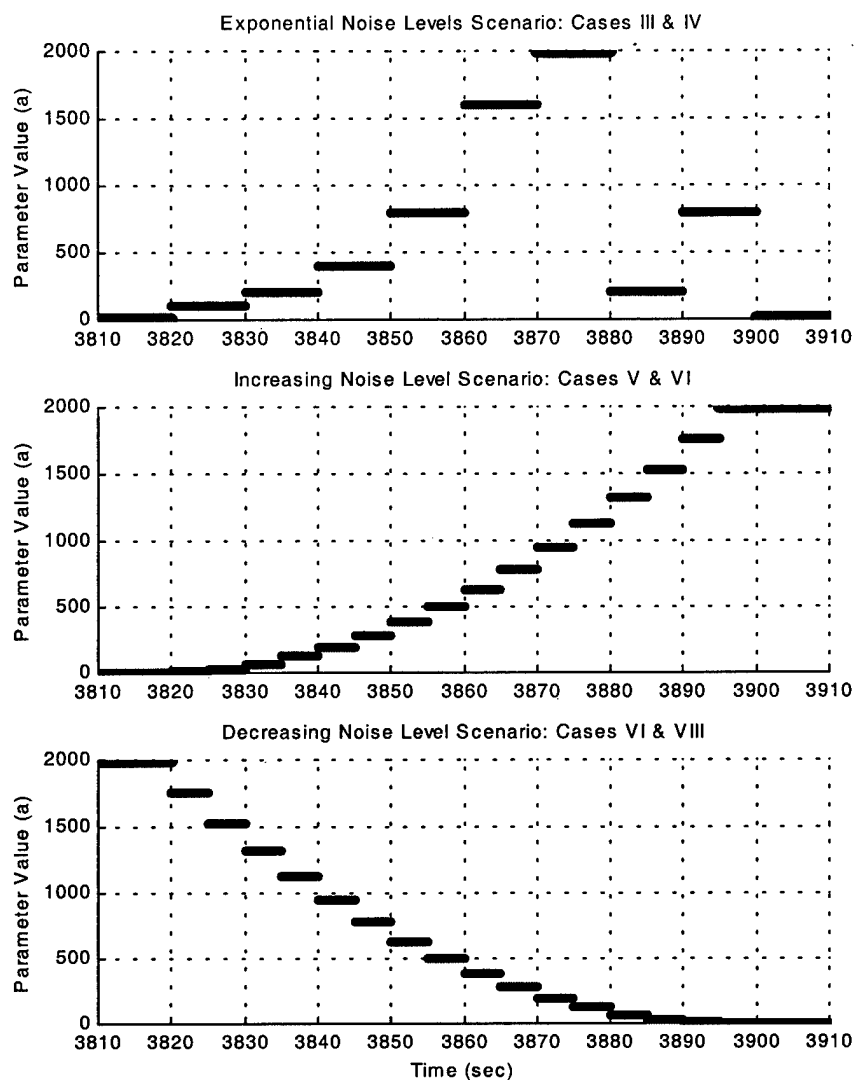


Figure 11. GPS Interference Scenarios

4.5. PLS Comparison Criteria

When the aircraft is on final approach, the FAA ILS criteria [12] are applied at specific decision heights (DH). When the aircraft reaches a particular DH, the uncertainty in the horizontal and vertical must be no greater than the values specified by

that category. These values and the time in the trajectory when the aircraft in these simulations reaches the DH points are summarized in Table 4.

Table 4. FAA ILS Precision Approach Requirements ($\pm 1\sigma$)

| Category | Decision Height (AGL) | Occurrence in Flight Trajectory | Horizontal Accuracy | Vertical Accuracy |
|----------|-----------------------|---------------------------------|---------------------|-------------------|
| I | 200 ft | 3,894 sec | ± 28.1 ft | ± 6.8 ft |
| II | 100 ft | 3,902 sec | ± 8.6 ft | ± 2.8 ft |
| III | 50 ft | 3,907 sec | ± 6.8 ft | ± 1.0 ft |

Two types of data plots are displayed in the next sections covering each test case. The first type includes six graphs. The top graph is a plot of the MMAE's estimate of the parameter, \hat{a} over the simulation period. The solid line indicates the mean value of \hat{a} over ten Monte Carlo runs, while a dashed line above and below show the span of one standard deviation in \hat{a} ($\pm\sigma_a$) over the ten Monte Carlo runs. The heavier solid flat lines represent the true values of a . The horizontal dotted lines show the values of a where each elemental filter is placed, i.e., $a_k, k \in \{1, 2, 3, 4, 5\}$. The five graphs below the estimated parameter plot illustrate how the probability assigned to each elemental filter, p_k , varies over time. Again, a solid line represents the mean value of the quantity in question, p_k , and the dashed lines represent the span of one standard deviation of p_k ($\pm\sigma_p$) over ten Monte Carlo runs. Figure 12 shows a legend for these plots.

The second type of figure shows three graphs. Each one displays the error in the position of the aircraft as it varies during the landing period. The top graphs shows the variation in error in the east horizontal (longitude) direction, the middle graph shows the same for the north horizontal (latitude) direction, and the bottom graphs shows this for

the vertical (altitude) direction. The solid line in the center of each plot represents the mean position error over ten Monte Carlo runs. The dotted lines above and below it represent the span of one standard deviation of the position error ($\pm\sigma_{True}$) over the ten Monte Carlo runs. This is the actual level of estimation performance encountered in the simulations. The dashed lines above and below these represent the span of one standard deviation computed by the filter ($\pm\sigma_{Filter}$). According to the filter model, this is the level of uncertainty expected under the conditions of the simulation. In addition, the filter-computed standard deviation, σ_{Filter} , is shown added to and subtracted from a value of zero, since the filter assumed the errors to be a zero-mean process. Figure 13 shows a legend for these plots.

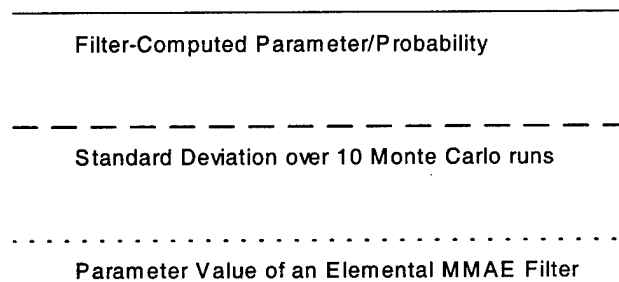


Figure 12. Parameter / Estimated Probability Plot Legend

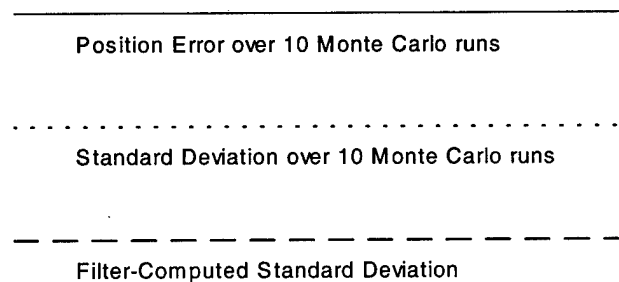


Figure 13. Position Error Plot Legend

4.6. Nominal Interference Scenario

The two cases that follow are set up to examine the performance of the M³AE model in the absence of RF interference. The parameter a is set to 1 to represent a condition where the pseudorange measurement noise variance is equal to the nominal value, i.e., $R_{PRj} = R_{PRO}$, $j \in \{1, 2, 3, 4, 5\}$ (see Section 3.9). Although $a = 1$, the MMAE estimated parameter delivered to the state estimator, \hat{a} , is a higher value. This is due to the minimum probabilities assigned to each elemental filter, p_{\min} . The MMAE implemented in these simulations have $p_{\min} = 0.001$. Thus, assuming the a_1 elemental filter receives all of the probability weight less the minimum assigned to the other filters, the estimated parameter used by the state estimator is computed by:

$$\hat{a} = \sum_{k=1}^5 a_k p_k = 0.996a_1 + 0.001 \sum_{k=2}^5 a_k = 4.514797 \quad (98)$$

Although this value is over four times greater than the nominal, it is the best the MMAE can do given the p_{\min} specified. Given the nature of this problem, it recommended that the blending could be limited to remove the effects caused by p_{\min} (see Section 5.3).

4.6.1. Case I

This case covers the best scenario of the ones examined, using the INS with the lower drift rate, 0.4 nmi/hr, and having no added measurement noise. Figure 14 shows how the estimated parameter, \hat{a} , and the elementary filter probability weights, p_k , vary over time. Without RF interference present, the MMAE parameter estimator decides very quickly that the a_1 elemental filter is the best model for the system. Since a never changes throughout the scenario, \hat{a} remains unchanged once the MMAE determines the a_1 elemental filter has the best representation of the situation. The initial spike in the plot of

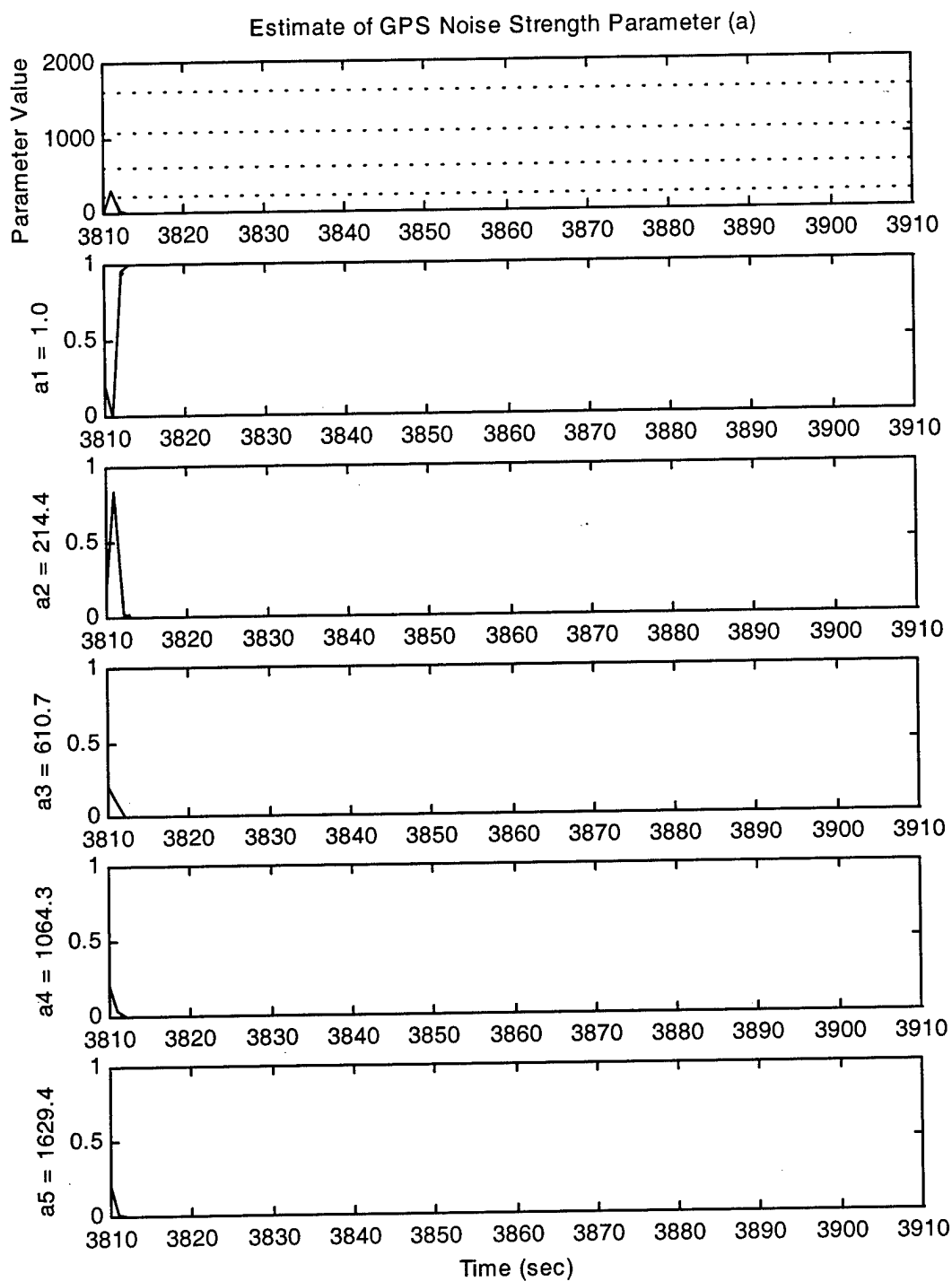


Figure 14. Case I: Estimated Parameter and Elemental Filter Probabilities

\hat{a} is due to the fact that each elemental filter has the same initial probability assigned to it, as shown in Figure 14. At 3,811 seconds, the a_2 elemental filter tries to grab all of the probability weight, but it is not the best representation of the current environment. The MMAE adapts quickly once the a_1 elemental filter residuals look the best, reflecting the current operating environment.

Figure 15 shows the output of the state estimator. The standard deviation of the errors in all three cardinal directions remains under 5 ft for nearly the entire period in question. The filter-computed standard deviation, σ_{Filter} , plots (dashed lines) start at a conservatively high value. It converges to a mean steady-state value of 1.02 ft in the east(/west) direction and 1.30 ft in the north(/south) direction 20 seconds into the trajectory. The value of σ_{Filter} in the vertical direction quickly converges to a value of 4.02 ft within 5 seconds and decreases steadily, as the aircraft approaches ground level. This is due to the improved measurement estimates in the vertical direction (i.e., altitude) due to the radar altimeter. Equation (68) shows that the variance of the noise in the radar altimeter measurement, R_{Rad} , is a function of the altitude AGL, h_{AGL} .

$$R_{Rad} = (0.01^2 h_{AGL}^2 + 0.25) \text{ ft}^2 \quad (68)$$

Thus, the closer the aircraft is to the ground, the better the radar altimeter readings become. This improvement was demonstrated by the research of Gray [13] and Britton [7], where the value of σ_{Filter} converged to a steady-state value and remained unchanged when radar altimeter measurements were not incorporated. Their research showed the same type of decrease in σ_{Filter} in the vertical direction seen in Figure 15 when radar altimeter measurements were included.

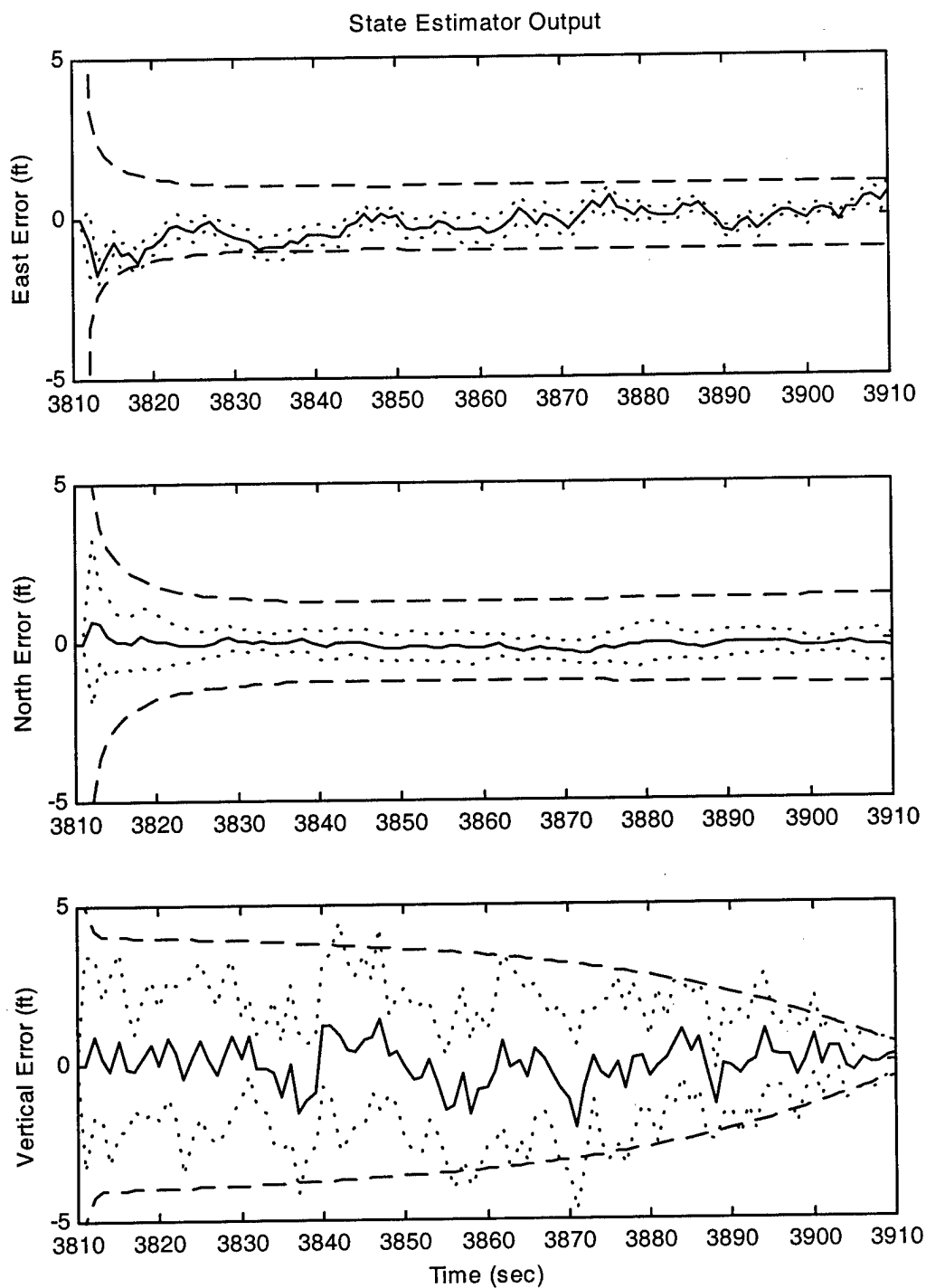


Figure 15. Case I: State Estimator Position Errors

The standard deviation of position errors over ten Monte Carlo runs, σ_{True} , (dotted lines) is consistently less than σ_{Filter} . This indicates that the state estimator overestimates the error in position, a conservative tuning philosophy. The mean of the position errors, even over ten Monte Carlo runs (solid line), does not remain exactly at zero; ideally, it should be (this was seen even over 20 Monte Carlo runs; ten runs were chosen for each case due to the length of computer simulation time required). Still, over time, the position errors do stay close to zero. In addition, as long as the mean position errors $\pm \sigma_{True}$ remain close to the σ_{Filter} bounds, the state estimator filter provides good estimates, as shown by Figure 15.

The critical tests come at the DHs of the FAA ILS categories. Tables 5 – 7 show the values of σ_{Filter} and σ_{True} at each DH for the three position errors. To assess horizontal accuracy, the values of σ_{Filter} in the east and north directions are compared to the FAA requirements. In Case I, the values of both σ_{Filter} and σ_{True} satisfy the Category III requirement, ± 6.8 ft. In the vertical direction, σ_{Filter} and σ_{True} also satisfy the Category III requirement, being ± 1.0 ft. The performance of Case I simulates the best situation of all the test cases considered. Thus, it serves as a reference to determine how a lower quality INS or RF interference degrades the performance of the navigation system.

Table 5. Case I: East Position Error Standard Deviations

| ILS Category | DH (ft) | σ_{Filter} (ft) | σ_{True} (ft) |
|--------------|---------|------------------------|----------------------|
| I | 200 | 1.034 | 0.263 |
| II | 100 | 1.034 | 0.142 |
| III | 50 | 1.034 | 0.302 |

Table 6. Case I: North Position Error Standard Deviations

| ILS Category | DH (ft) | σ_{Filter} (ft) | σ_{True} (ft) |
|--------------|---------|------------------------|----------------------|
| I | 200 | 1.345 | 0.342 |
| II | 100 | 1.361 | 0.233 |
| III | 50 | 1.369 | 0.530 |

Table 7. Case I: Vertical Position Error Standard Deviations

| ILS Category | DH (ft) | σ_{Filter} (ft) | σ_{True} (ft) |
|--------------|---------|------------------------|----------------------|
| I | 200 | 1.814 | 1.214 |
| II | 100 | 1.145 | 0.711 |
| III | 50 | 0.709 | 0.798 |

4.6.2. Case II

This case is identical to Case I, except an INS with a drift rate of 4.0 nmi/hr is implemented in the navigation system model. Figure 16 shows essentially identical results to Figure 14, for \hat{a} and p_k . This follows, since an INS is not affected by any external measurements and, the drift rate of the INS is not a function of the measurement noise (since it is not being updated by the filter).

Conversely, this does not apply to the output of the state estimator, as shown in Figure 17. While the position errors in all three directions remain under 5 ft, the plots of σ_{Filter} show that its steady-state values are greater in the horizontal directions: 1.83 ft, east, and 1.99 ft, north. The values of σ_{True} are still significantly smaller than σ_{Filter} ; however, as the position errors wander about zero, they fit closely within the σ_{Filter} bounds.

Tables 8 – 10 show how σ_{Filter} and σ_{True} compare with the ILS categories. In both the horizontal and vertical directions, the values of σ_{Filter} and σ_{True} satisfy the Category III

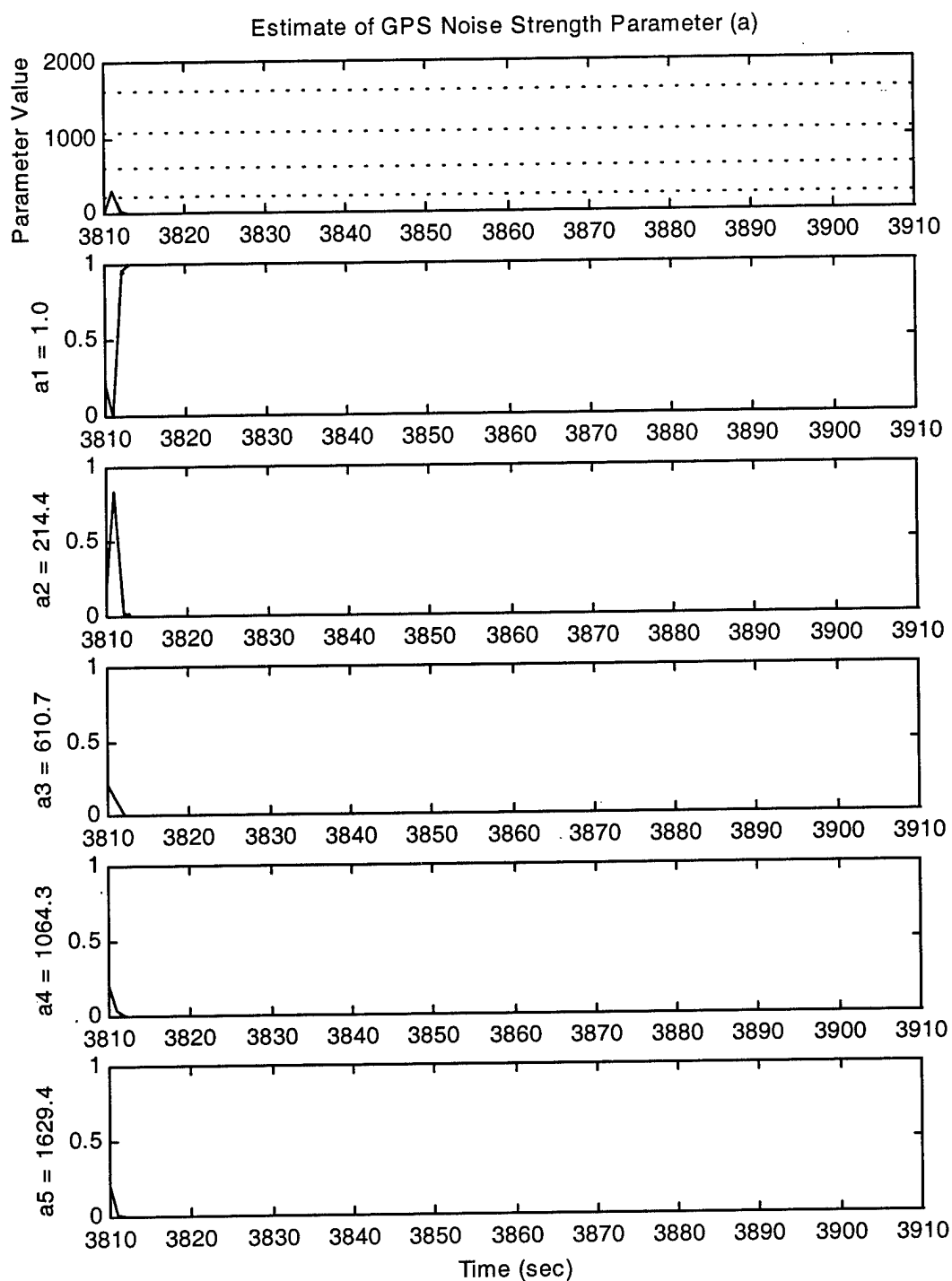


Figure 16. Case II: Estimated Parameter and Elemental Filter Probabilities

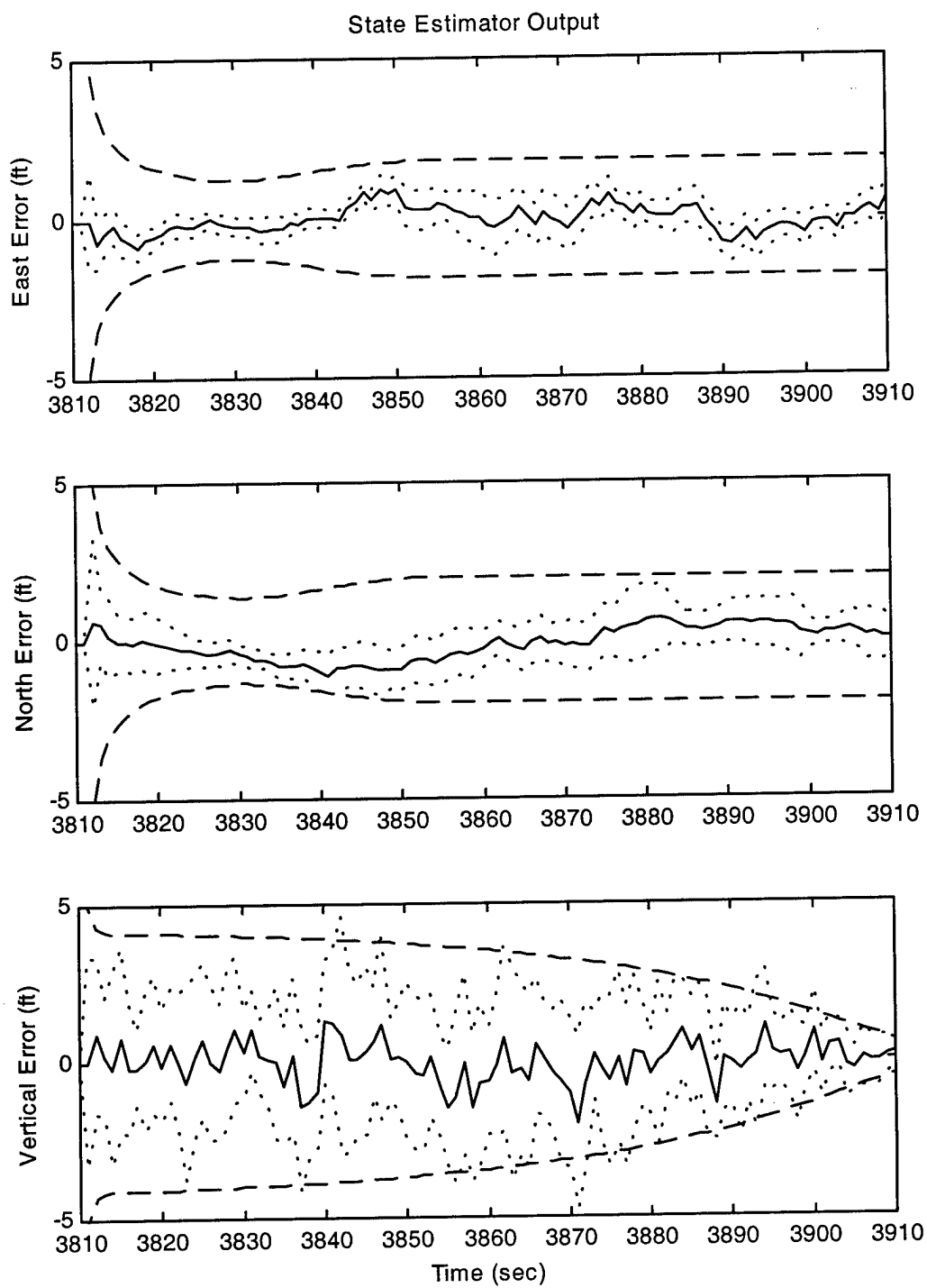


Figure 17. Case II: State Estimator Position Errors

Table 8. Case II: East Position Error Standard Deviations

| ILS Category | DH (ft) | σ_{Filter} (ft) | σ_{True} (ft) |
|--------------|---------|------------------------|----------------------|
| I | 200 | 1.834 | 0.593 |
| II | 100 | 1.829 | 0.348 |
| III | 50 | 1.826 | 0.457 |

Table 9. Case II: North Position Error Standard Deviations

| ILS Category | DH (ft) | σ_{Filter} (ft) | σ_{True} (ft) |
|--------------|---------|------------------------|----------------------|
| I | 200 | 1.999 | 0.723 |
| II | 100 | 1.999 | 0.354 |
| III | 50 | 1.997 | 0.808 |

Table 10. Case II: Vertical Position Error Standard Deviations

| ILS Category | DH (ft) | σ_{Filter} (ft) | σ_{True} (ft) |
|--------------|---------|------------------------|----------------------|
| I | 200 | 1.914 | 1.836 |
| II | 100 | 1.246 | 0.900 |
| III | 50 | 0.792 | 0.824 |

requirements. This shows that an INS with a greater drift rate may be used to met the requirements with nominal GPS pseudorange measurement noise present. In addition, this case serves as a reference for Cases IV, VI, and VIII to determine how increased level of pseudorange measurement noise (i.e., increase in a , hence R_{PRj}) affects the performance of this navigation system (with the 4.0 nmi/hr INS).

4.7. White's ("Exponential") Noise Levels Scenarios

The next two cases examine the system performance against a scenario used in White's research [56]. In this scenario, the value of the parameter a varies at levels of 1, 100, 200, 400, 800, 1600, and 2000 during the 100-second interval under investigation; as shown in the top plot of Figure 11. White used an MMAE with three elemental filters

with parameters spaced at: $a_1 = 1$, $a_2 = 200$, and $a_3 = 2,000$. The position errors (states) calculated by each filter were multiplied by its corresponding probability weight, p_k , $k \in \{1, 2, 3\}$, and then summed together to form a *blended* output.

In the cases performed in this research, blending is done to calculate \hat{a} to pass on to the state estimator, which determines the position errors. The difference between the position errors of a blended output of the MMAE and those of the state estimator are examined in this case to provide an initial baseline. However, it is important to note that the MMAE is tuned for parameter estimation in the M^3AE architecture.

4.7.1. Case III

This case involves the navigation system using the 0.4 nmi/hr drift rate INS with the parameter a (thus, R_{PRj}) at levels researched by White [56]. Figure 18 shows how \hat{a} and p_k vary over the scenario. In the top plot, the actual value of the parameter a is shown by the heavy solid lines. The MMAE estimate, \hat{a} , adapts its value whenever a changes. During the first 10 seconds, the MMAE estimates $\hat{a} = 4.51$ as in the nominal scenario when $a = 1$. When a becomes 100 in the next 10 seconds (3,820 – 3,830 sec), \hat{a} settles on a mean value of 216.9 within 2 seconds. This is very close to the value of $a_2 = 214.4$, indicating the MMAE weighted the a_2 elemental filter with nearly all of the probability weight ($p_2 = 0.996$) and judged it to be the most accurate model for the current operating environment. Thus, minimal blending occurred during this period. Also, the standard deviation of \hat{a} , $\sigma_{\hat{a}}$, remains below 0.1, showing that the MMAE was very consistent in assigning $\hat{a} = 216.9$. This can be seen by the five probability plots; p_2 receives almost all

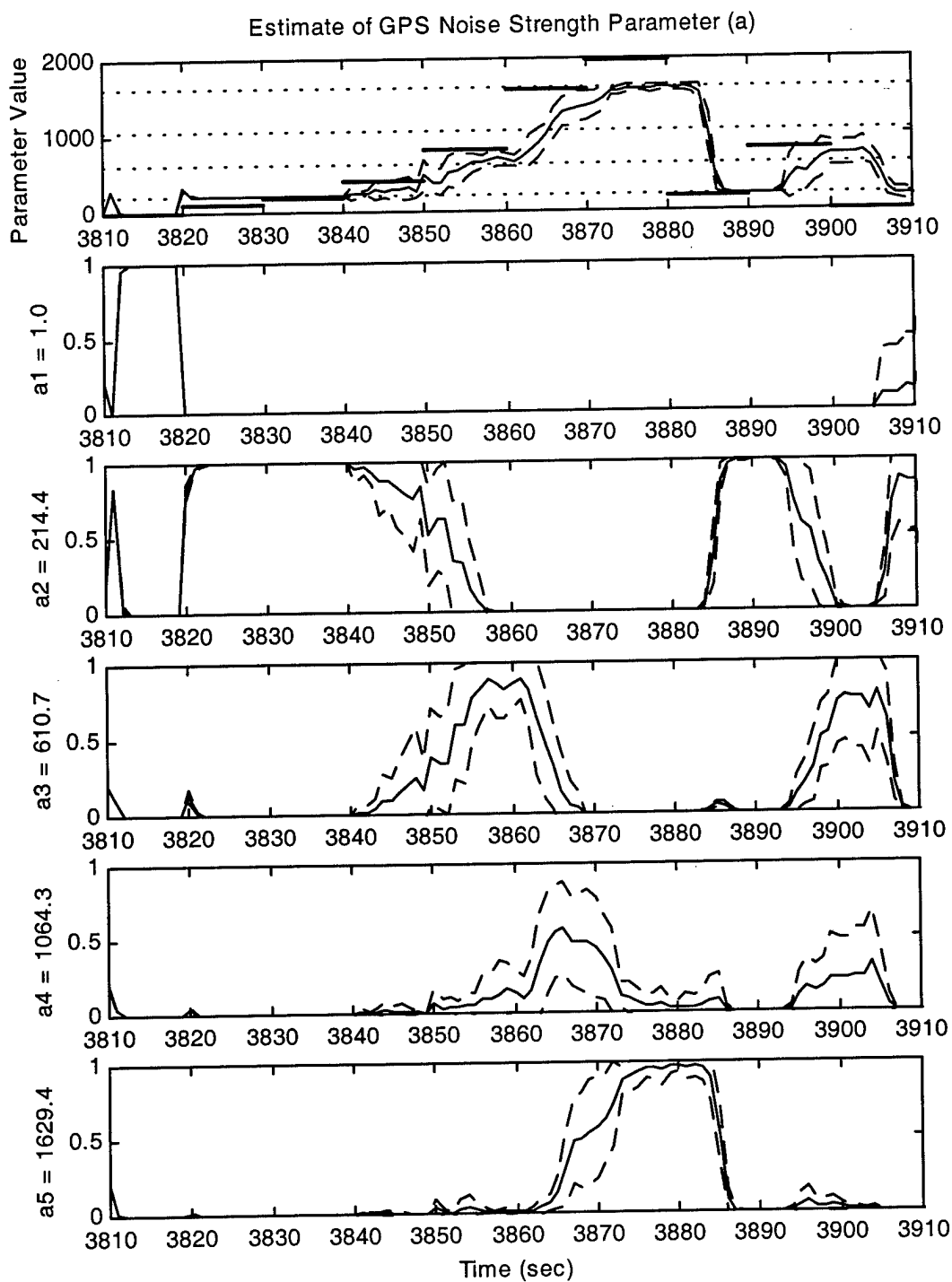


Figure 18. Case III: Estimated Parameter and Elemental Filter Probabilities

of the probability (only 0.996, though, due to p_{min} of the other filters) very quickly while the elemental filters have probabilities near zero.

For the period when $a = 200$ (3,830 – 3,840 sec), the mean of \hat{a} stays at 216.9, which is appropriate since that value is close to a_2 . When a changes level to 400 and 800 (3,840 – 3,850 sec and 3,850 – 3,860 sec, respectively), the MMAE starts to show some blending. The value of \hat{a} does not quite reach a , though it does increase. The probability plots show the probability weighting being distributed primarily between p_2 and p_3 . The increase in the standard deviations of \hat{a} and p_k indicate the MMAE may favor one elemental filter over the others in a single Monte Carlo run. Still, taking the mean over the ten Monte Carlo runs, as shown in the plots of Figure 18, it averages out to show that probability blending taking place.

As a reaches the levels of 1,600 and 2,000 (3,860 – 3,870 sec and 3,870 – 3,880 sec, respectively), the MMAE takes all of the period when $a = 1,600$ to push \hat{a} near that value, and \hat{a} hits a ceiling at 1,612.5 when $a = 2,000$. This ceiling is due to the highest value of a_k for an elemental filter, which is $a_5 = 1,629.4$. The parameter estimate, \hat{a} , can never be greater than a_5 , and its upper limit is slightly less due to the p_{min} that must be assigned to the other filters. Even though the MMAE cannot estimate $a = 2,000$ exactly in the configuration used in this research, the M³AE's state estimate performance is still effective as shown later.

For the remainder of the scenario, when a decreases from 800 to 1, the mean of \hat{a} follows, but with a lag of approximate 5 seconds. This is a typical aspect of fixed-bank MMAEs. The delay occurs since the majority of the probability weight resides with the filter that has the higher a_k value and consequently smaller $L_k(t_i) = \mathbf{r}_k^T(t_i)\mathbf{A}_k^{-1}\mathbf{r}_k(t_i)$ value.

This gives the MMAE the false impression that it has the best parameter estimation performance [33]. However, the MMAE quickly responds once the residuals indicate this performance is incorrect. Subsequently the estimation performance improves when the elemental filter with the best estimate of a is given the majority of the probability weight.

Figure 19 shows the blended output of the position errors from the MMAE (tuned for parameter estimation). Although the MMAE used in these cases is not tuned for state estimation, the output is examined to give a link to the past research of White [56], which involved an MMAE used for state estimation. These plots follow the results of White's [56] research, using his navigational set-up and scenario (cf. Nav Case 1 in [56]). The minor differences between the plots here and in [56] can be attributed to using a different set-up of the elemental filters in the MMAE. Blending does provide considerably better estimates of the position errors than a single non-adaptive Kalman filter could. Figure 20 shows the position error plots from the output of the a_1 elemental filter (note the difference in scale). This filter measurement noise parameter is tuned for performance under nominal conditions. When the measurement noise changes, as in this case, its performance drastically suffers. Improving performance under changing parameters is the thrust for developing adaptive filtering techniques such the M^3AE .

Figure 21 shows the positions errors calculated by the state estimator within the M^3AE . The horizontal (east and north) position error estimates improve when using a filter provided with an estimate of the uncertain parameter (the state estimator) over using ordinary MMAE blending techniques. As mentioned before, the MMAE used in these

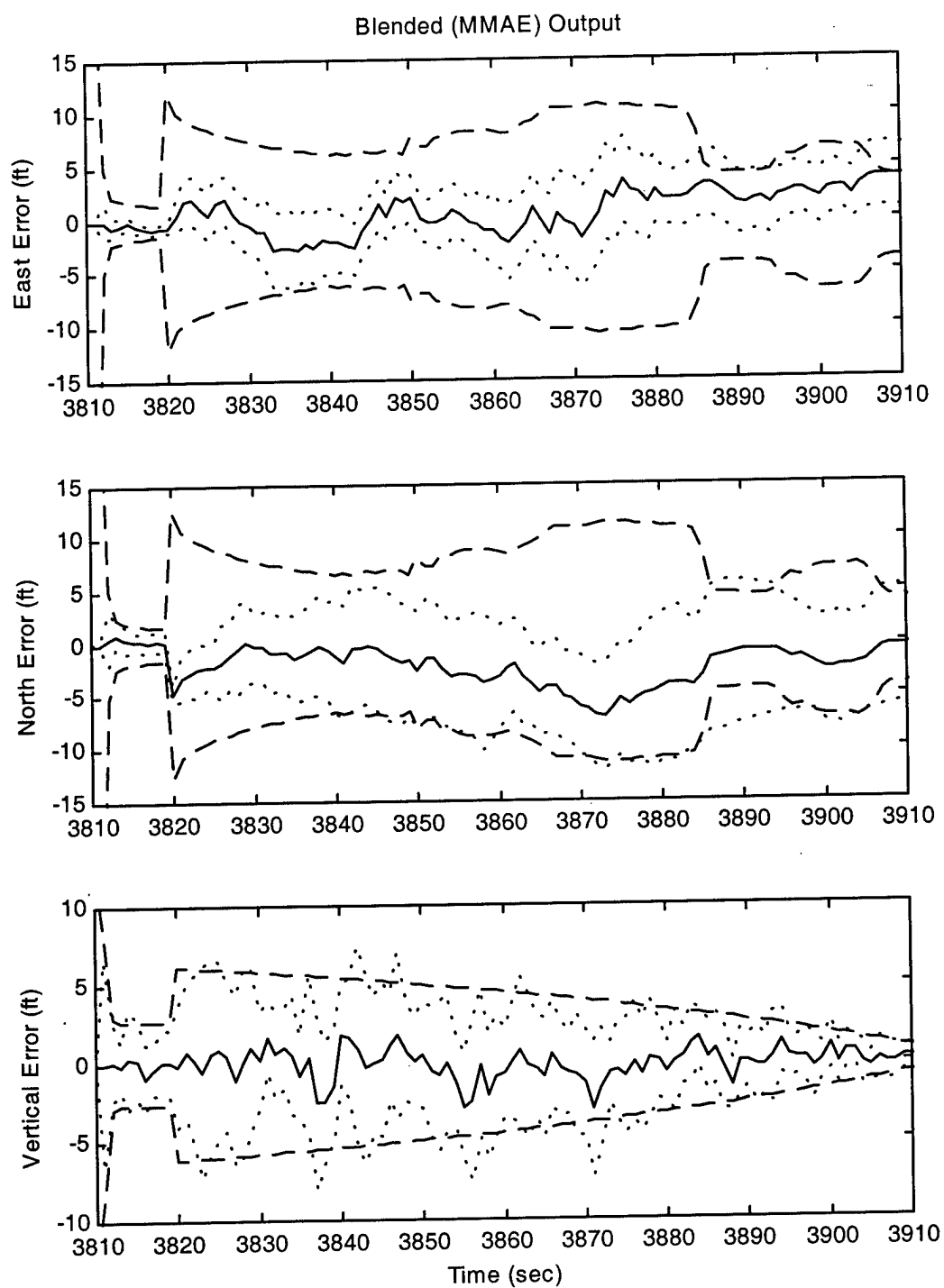


Figure 19. Case III: Blended (MMAE) Position Errors

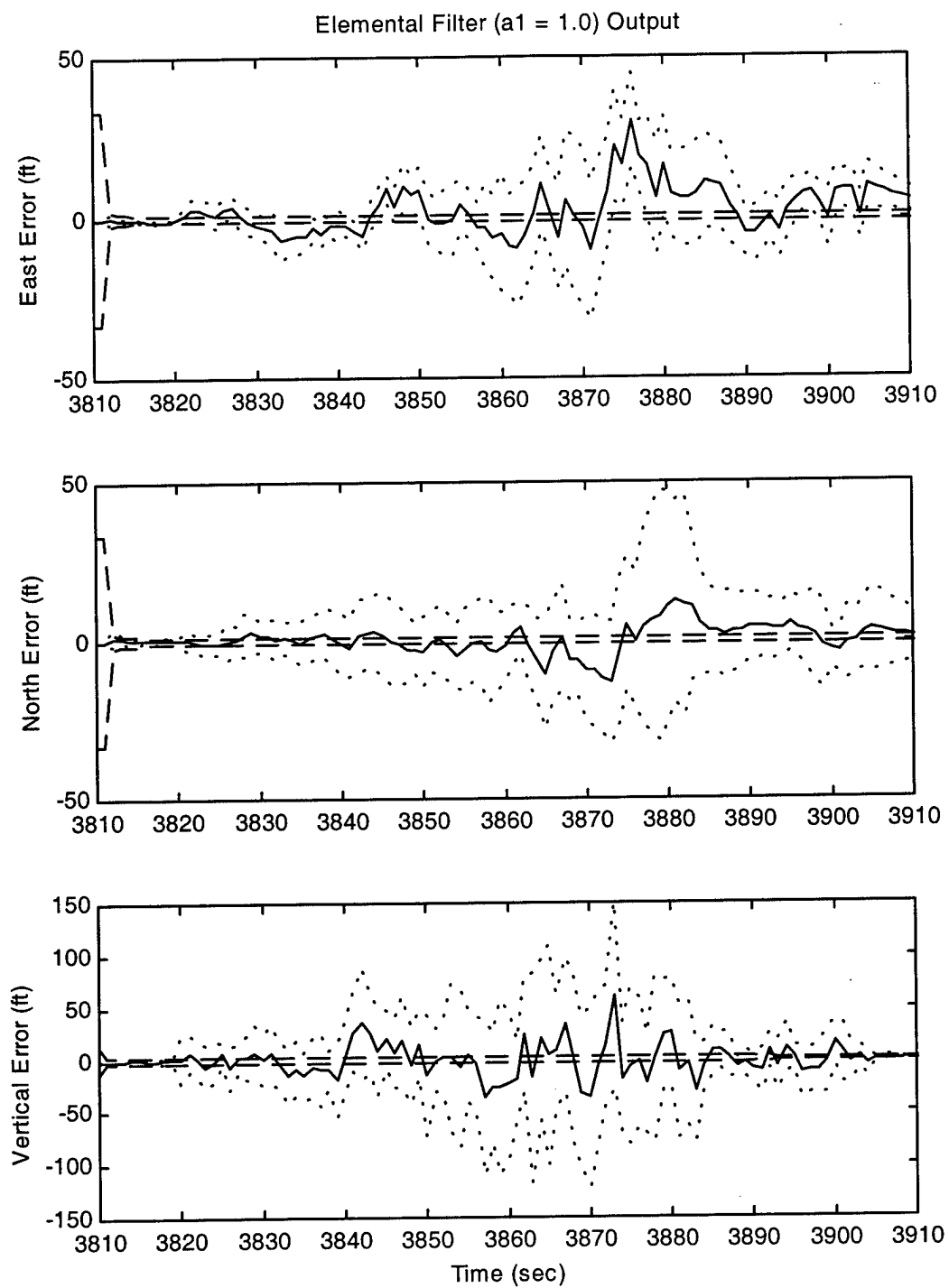


Figure 20. Case III: Elemental Filter ($a_1 = 1.0$) Position Errors

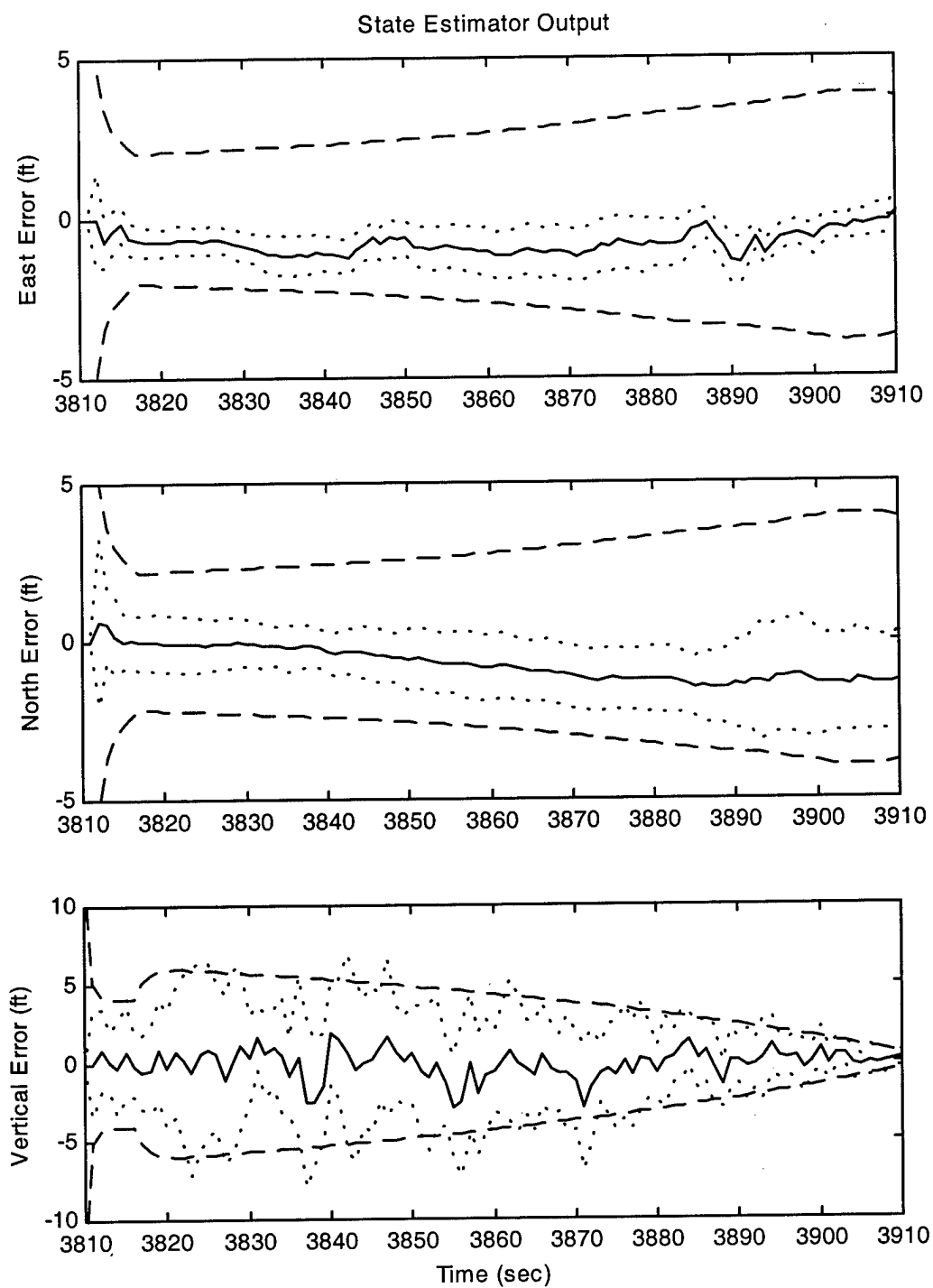


Figure 21. Case III: State Estimator Position Errors

simulations is not optimized for state estimation. Still, the state estimator's σ_{Filter} and σ_{True} values are less than their corresponding blended values. Both horizontal values of σ_{Filter} converge to 2.1 ft in the beginning of the scenario. Then they gradually increase as a increases over time. There is a slight decrease in σ_{Filter} at the end, reflecting the decrease in interference levels. The values of σ_{True} are much smaller than σ_{Filter} , erring on the side of caution. The vertical position error estimates show only minor improvement. This can be attributed to the radar altimeter. It provides better measurements as the aircraft approaches the ground (viz. R_{Rad}), making both the MMAE's blended output and the state estimator's output comparable and both very good.

Tables 11 – 13 show the values of σ_{Filter} and σ_{True} at each DH for the three position errors. The values shown are greater than those in Case I, but in both the horizontal and vertical directions, the values of σ_{Filter} and σ_{True} still satisfy the Category III requirements.

Table 11. Case III: East Position Error Standard Deviations

| ILS Category | DH (ft) | σ_{Filter} (ft) | σ_{True} (ft) |
|--------------|---------|------------------------|----------------------|
| I | 200 | 3.567 | 0.431 |
| II | 100 | 3.868 | 0.393 |
| III | 50 | 3.841 | 0.489 |

Table 12. Case III: North Position Error Standard Deviations

| ILS Category | DH (ft) | σ_{Filter} (ft) | σ_{True} (ft) |
|--------------|---------|------------------------|----------------------|
| I | 200 | 3.672 | 1.741 |
| II | 100 | 3.976 | 1.519 |
| III | 50 | 3.966 | 1.503 |

Table 13. Case III: Vertical Position Error Standard Deviations

| ILS Category | DH (ft) | σ_{Filter} (ft) | σ_{True} (ft) |
|--------------|---------|------------------------|----------------------|
| I | 200 | 1.902 | 1.390 |
| II | 100 | 1.166 | 0.774 |
| III | 50 | 0.714 | 0.787 |

The level of interference (measurement noise) was significant in the time just before the DH were reach, though it dropped to a nominal level in the last 10 seconds of the scenario. The value of a did drop dramatically in the last 5 seconds, so this may have allowed the ILS categories to be met. Case V shows the same navigation configuration under a continually increasing level of noise to observe its performance when the interference level is high at touch-down.

4.7.2. Case IV

This case is identical to Case III, except a 4.0 nmi/hr drift rate INS is used rather than the 0.4 nmi/hr INS. The results of \hat{a} and p_k from the MMAE essentially duplicate those of Case III shown in Figure 18, as expected, thus they are not shown. Figure 22 shows the blended output of the position errors from the MMAE. Like the results of Case III shown in Figure 19, these plots follow the results of White's research [56] (cf. Nav Case 4 in [56]; N.B., White does not use GPS pseudolite or radar altimeter measurements in this case.). Figure 23 shows the position error plots from the output of the a_1 elemental filter to display the poor estimates generated by a single Kalman filter tuned for nominal performance.

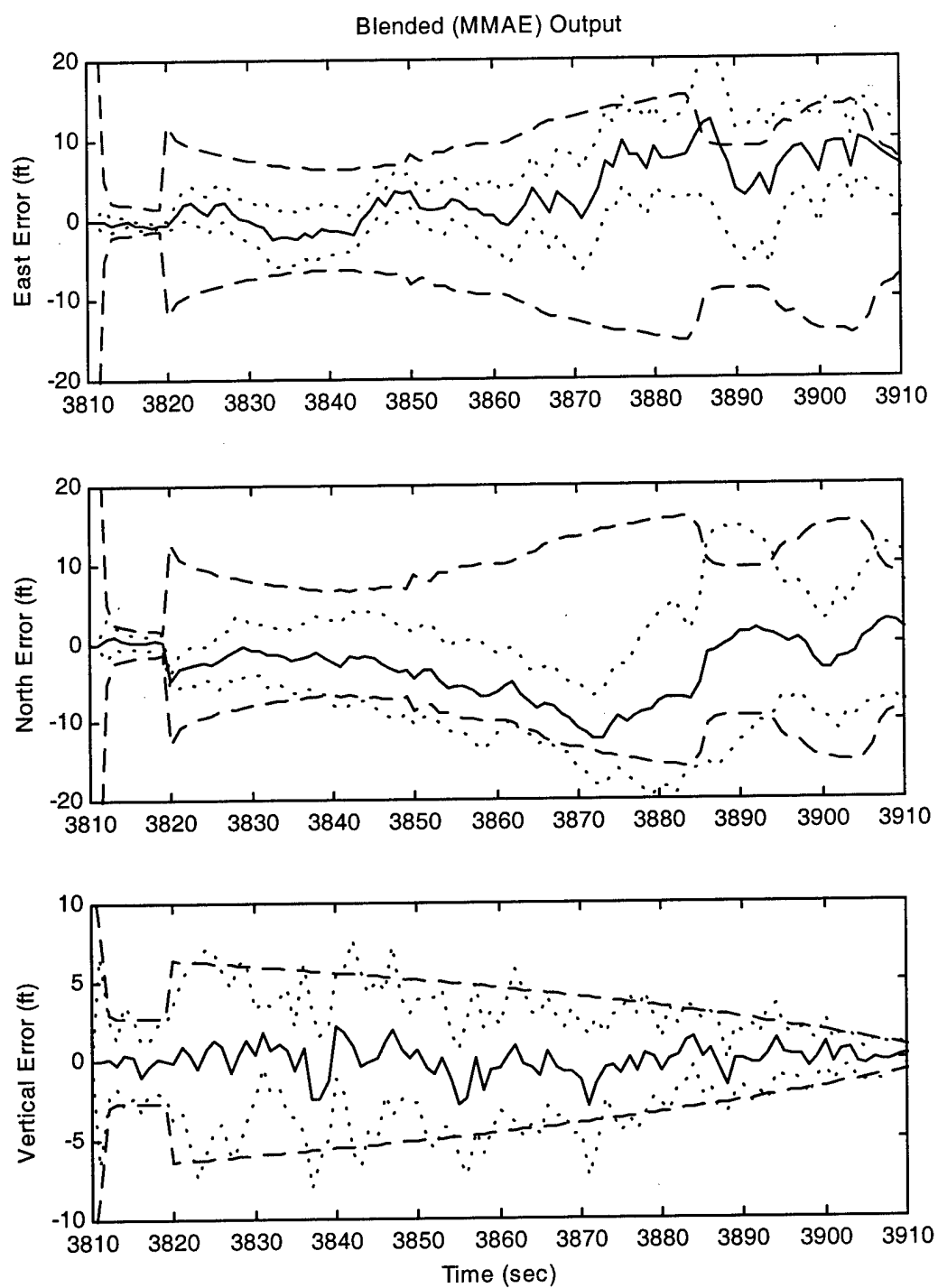


Figure 22. Case IV: Blended (MMAE) Position Errors

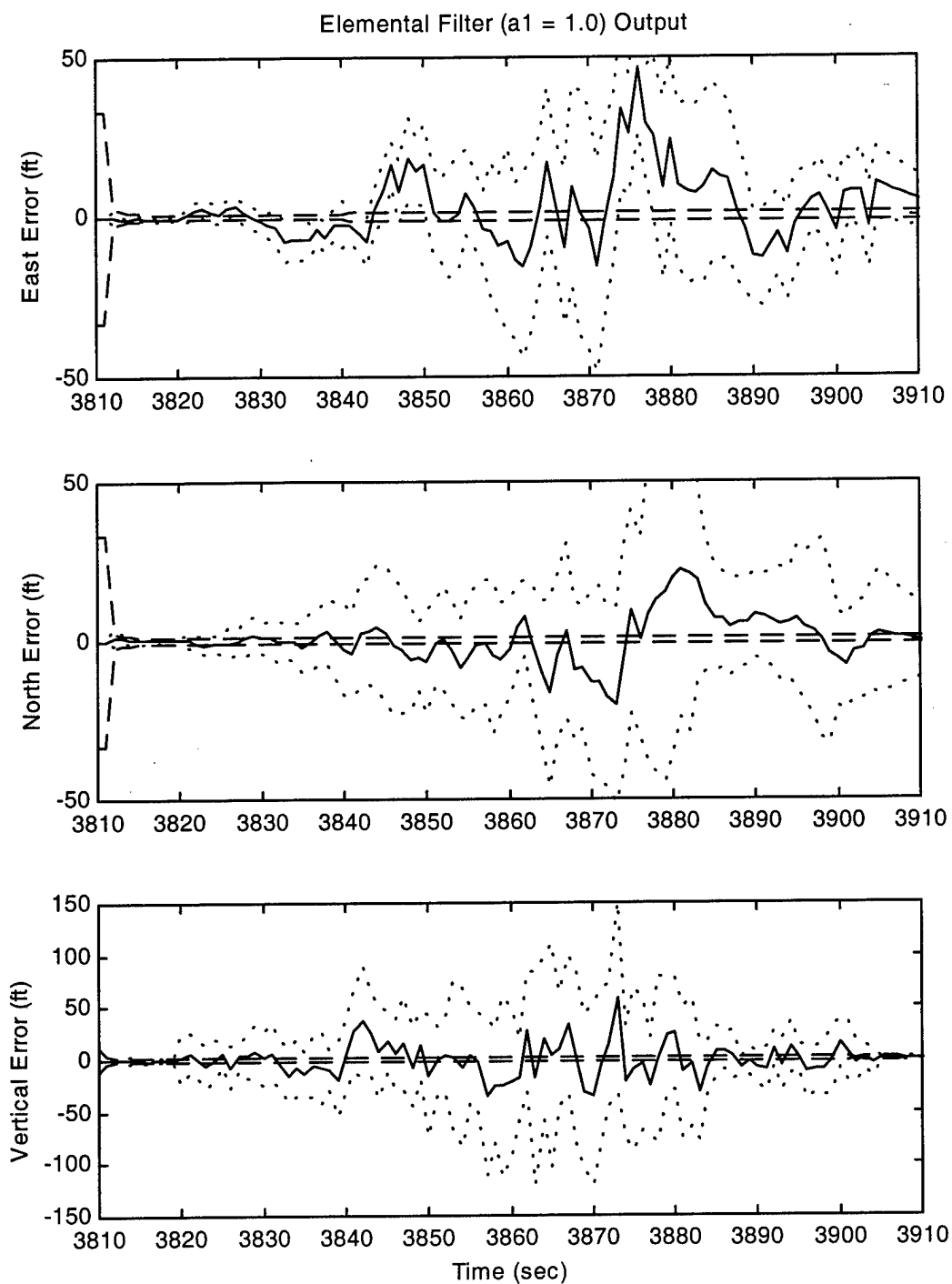


Figure 23. Case IV: Elemental Filter ($a_1 = 1.0$) Position Errors

The output of the M³AE's state estimator is shown in Figure 24. As in Case III, there is a great deal of improvement of these position errors estimates over those from the MMAE, especially in the horizontal directions. The values of σ_{Filter} and σ_{True} for the horizontal position errors are significantly greater than those of Case III; this shows the effects of using an INS with a larger drift rate. (Note the difference in scale of the east and north position error axes between Figures 21 and 24.)

There is a noticeable growth in these values after 3,850 seconds into the scenario. This is expected since a jumps to the levels of 800, 1600, and 2000. Also, for the most part, the values of the estimated east and north errors $\pm \sigma_{True}$ still fit within the bounds of σ_{Filter} . The vertical position error estimates do not show significant difference between the state estimator output of Case III, though, as mentioned previously, the radar altimeter measurements have a significant impact on the altitude measurements.

Tables 14 – 16 show the values of σ_{Filter} and σ_{True} at each DH for the three position errors. In comparing the values of σ_{Filter} against the FAA criteria, this case still satisfies Category III for the vertical positioning error; however, it can only meet Category I for horizontal positioning. The values of σ_{True} show better results with vertical positioning meeting Category III and horizontal positioning meeting Category II. Unlike Case III, the horizontal position errors did not improve quickly enough to meet Category III in all areas. It can be seen that the system modeled with the 4.0 nmi/hr INS results in degraded performance in horizontal position. Thus, this suggests that an INS with a lower drift rate is important to satisfy the landing requirements in this scenario.

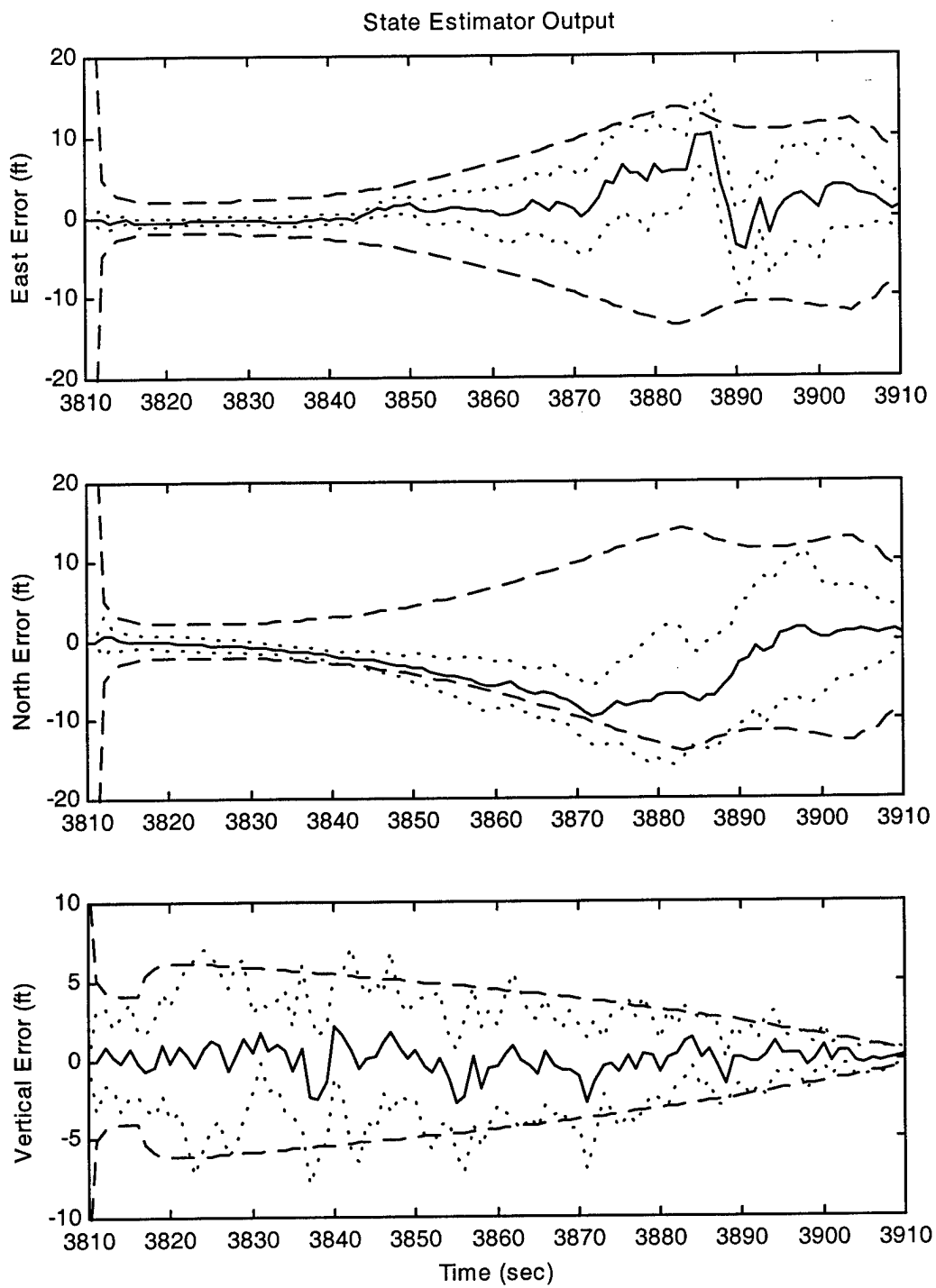


Figure 24. Case IV: State Estimator Position Errors

Table 14. Case IV: East Position Error Standard Deviations

| ILS Category | DH (ft) | σ_{Filter} (ft) | σ_{True} (ft) |
|--------------|---------|------------------------|----------------------|
| I | 200 | 10.67 | 5.614 |
| II | 100 | 11.72 | 5.579 |
| III | 50 | 10.43 | 3.394 |

Table 15. Case IV: North Position Error Standard Deviations

| ILS Category | DH (ft) | σ_{Filter} (ft) | σ_{True} (ft) |
|--------------|---------|------------------------|----------------------|
| I | 200 | 11.42 | 8.222 |
| II | 100 | 12.58 | 5.980 |
| III | 50 | 11.25 | 4.033 |

Table 16. Case IV: Vertical Position Error Standard Deviations

| ILS Category | DH (ft) | σ_{Filter} (ft) | σ_{True} (ft) |
|--------------|---------|------------------------|----------------------|
| I | 200 | 2.016 | 1.954 |
| II | 100 | 1.273 | 0.920 |
| III | 50 | 0.798 | 0.818 |

4.8. Increasing Noise Levels Scenarios

Cases V and VI examine the system performance against a scenario where the level of GPS pseudorange measurement noise increases as the aircraft approaches the touch-down point. The level of σ increases in inverse proportion to the square of the distance to the RF interference source (viz. Friis transmission formula [8]). The source is assumed to be in-line with the flight path of the aircraft. This is meant to depict a point source of RF interference increasing the level of measurement noise for R_{PRj} . Although this is not the most accurate representation, it is meant to show the effects on the position errors as the landing aircraft moves toward an interference source.

To implement the increasing level of a over time (hence over distance, as the aircraft maintains a steady glide velocity), different constant values of a had to be shown in separate intervals. This is due the limitation of the software configuration used, which could only accept constant parameter values at a maximum of 19 intervals. Table 17 shows the how a varies over this scenario.

Table 17. Increasing Noise Levels Scenario

| Interval Start Time (sec) | Actual Parameter (a) |
|---------------------------------|--------------------------------|
| 3,810 | 1.0 |
| 3,820 | 8.0 |
| 3,825 | 30.0 |
| 3,830 | 70.0 |
| 3,835 | 125.0 |
| 3,840 | 195.0 |
| 3,845 | 280.0 |
| 3,850 | 380.0 |
| 3,855 | 500.0 |
| 3,860 | 630.0 |
| 3,865 | 780.0 |
| 3,870 | 945.0 |
| 3,875 | 1,125.0 |
| 3,880 | 1,320.0 |
| 3,885 | 1,530.0 |
| 3,890 | 1,760.0 |
| 3,895 | 2,000.0 |

4.8.1. Case V

This case involves the navigation system using the 0.4 nmi/hr drift rate INS. Figure 25 shows how \hat{a} and p_k vary over the scenario. As in Figure 18, the top plot of Figure 25 includes the actual value of the parameter a with heavy solid lines. The value of \hat{a}

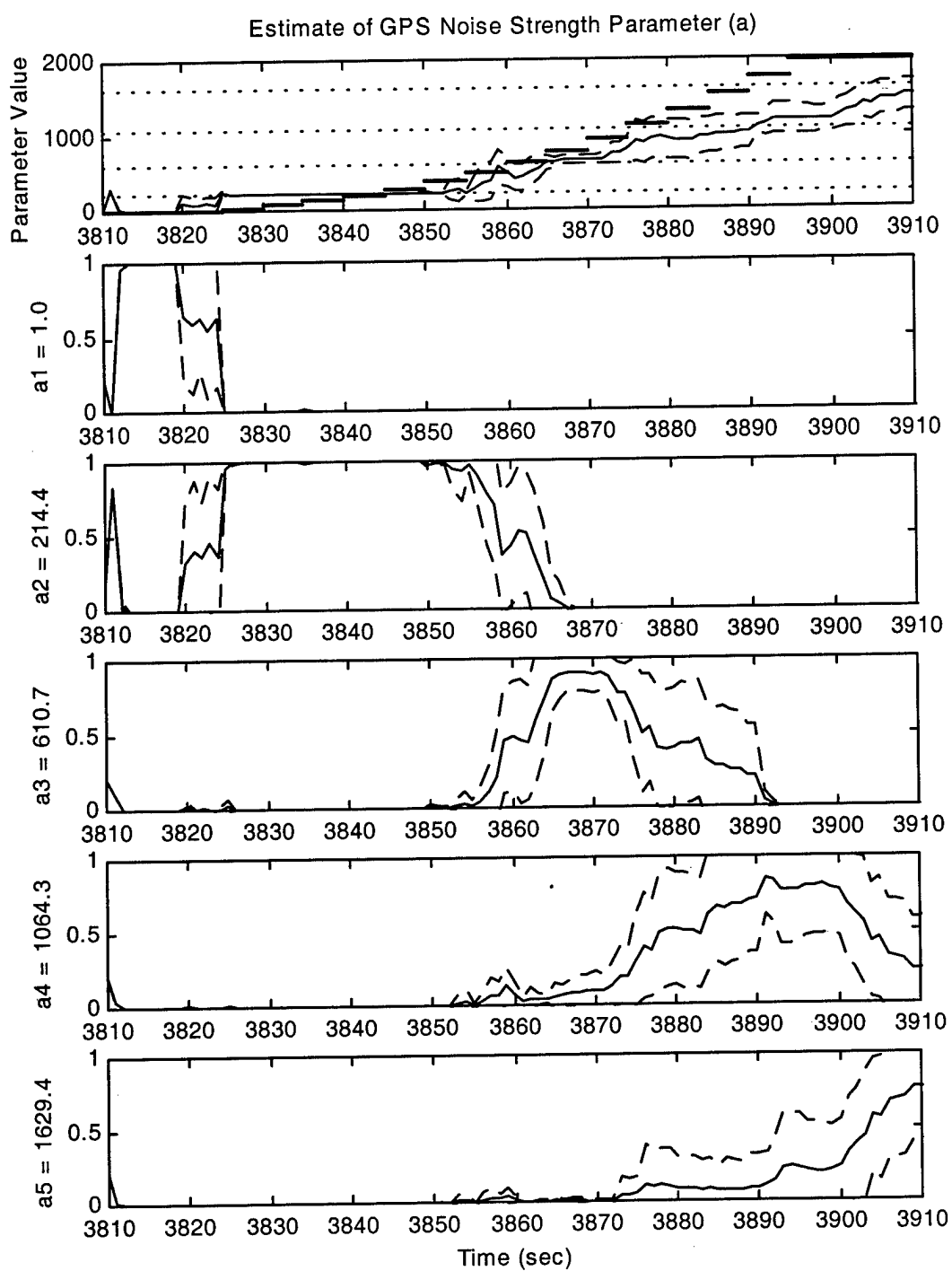


Figure 25. Case V: Estimated Parameter and Elemental Filter Probabilities

follows a throughout the scenario. Up to 3,820 seconds, the a_1 elemental filter is chosen to be the best model. When $a = 8$, between 3,820 seconds and 3,825, the MMAE calculates a blended estimate of $\hat{a} \approx 93$. After that point, when a becomes 30 at 3,825 seconds, the MMAE gives nearly all of the probability weighting to the a_2 elemental filter. This remains the case until 3,850 seconds, when a becomes 380. From this point on, blending occurs within the MMAE to determine the value \hat{a} . At 3,875 seconds, the estimated parameter, \hat{a} , starts to lag the actual parameter, a , which takes on the value of 1,125 at that time. Throughout the remainder of the scenario, the value of \hat{a} slowly increases towards its upper limit, just under a_5 . Again, this highlights the impact of not having an elemental filter at $a = 2,000$ (see recommendation in Section 5.3).

Figure 26 shows the position errors according to the M^3AE 's state estimator. The results appear similar to those of Case III shown in Figure 21 without the decrease in σ_{Filter} at the very end. The absence of the decrease is due to a remaining at 2,000, rather taking on lower levels as in Case III. Also, the values of σ_{True} are much less than σ_{Filter} as in Case III, though they are greater than σ_{True} of Case III overall.

Tables 18 – 20 show the values of σ_{Filter} and σ_{True} at each DH. The horizontal and vertical positioning error according to both σ_{Filter} and σ_{True} continues to meet Category III. This suggests there is no significant impact of a remaining at 2,000 in this scenario. Thus, the navigation system configuration with the lower drift rate INS can operate sufficiently well in the presence of a high degree of pseudorange measurement noise. However, it should be noted that GPS aiding was present at the beginning of the scenario and reduced over time. Previous research [7, 13, 38, 56] has shown that, without GPS aiding, this level of precision could not be met.

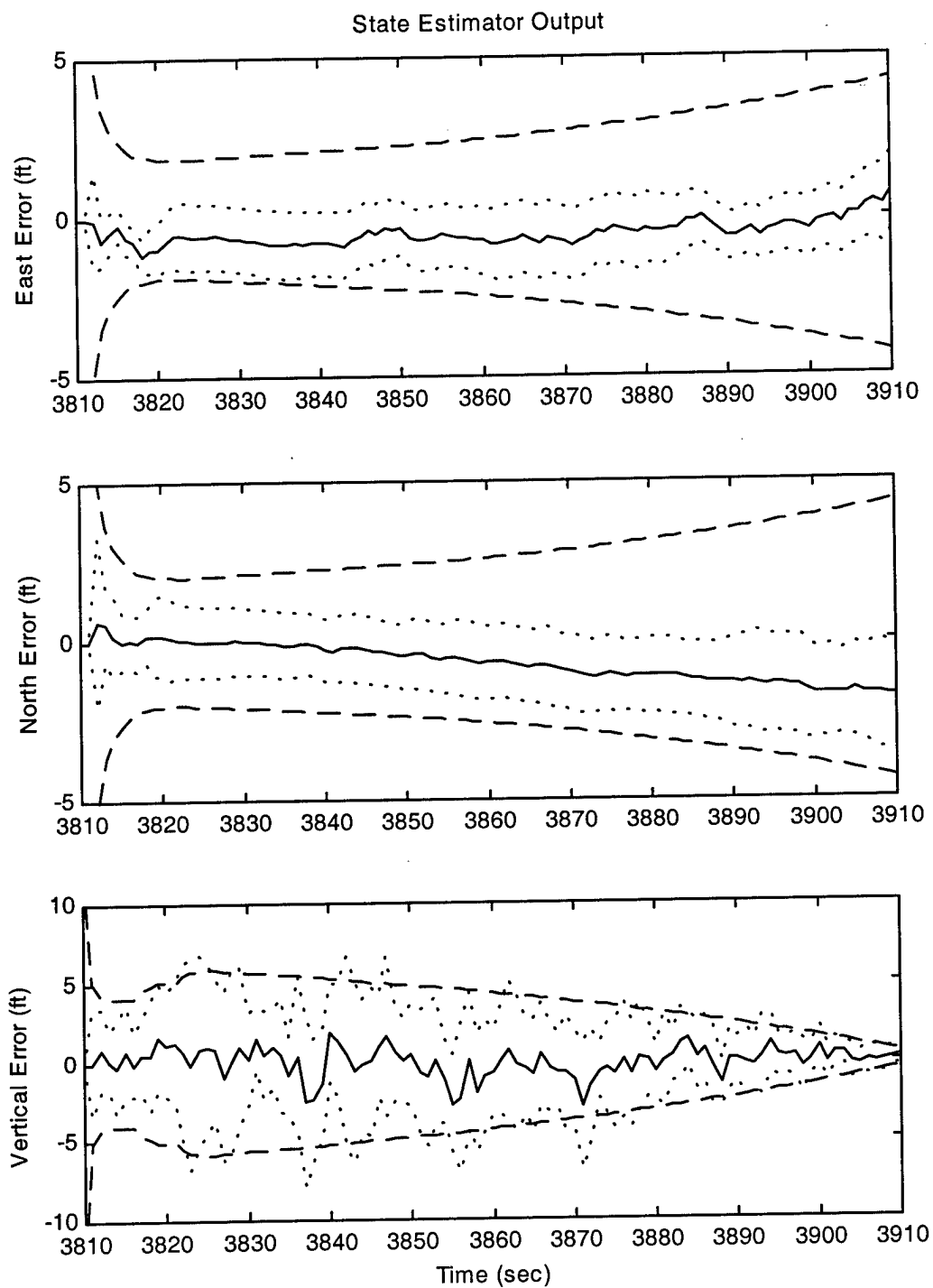


Figure 26. Case V: State Estimator Position Errors

Table 18. Case V: East Position Error Standard Deviations

| ILS Category | DH (ft) | σ_{Filter} (ft) | σ_{True} (ft) |
|--------------|---------|------------------------|----------------------|
| I | 200 | 3.566 | 0.863 |
| II | 100 | 3.914 | 0.983 |
| III | 50 | 4.153 | 1.149 |

Table 19. Case V: North Position Error Standard Deviations

| ILS Category | DH (ft) | σ_{Filter} (ft) | σ_{True} (ft) |
|--------------|---------|------------------------|----------------------|
| I | 200 | 3.649 | 1.481 |
| II | 100 | 3.997 | 1.309 |
| III | 50 | 4.236 | 1.712 |

Table 20. Case V: Vertical Position Error Standard Deviations

| ILS Category | DH (ft) | σ_{Filter} (ft) | σ_{True} (ft) |
|--------------|---------|------------------------|----------------------|
| I | 200 | 1.902 | 1.395 |
| II | 100 | 1.166 | 0.768 |
| III | 50 | 0.715 | 0.794 |

4.8.2. Case VI

This case is identical to Case V, except for the 4.0 nmi/hr drift rate INS. As in Case IV, the results of \hat{a} and p_k are not shown since they essentially duplicate those of the previous case shown in Figure 25. The output of the state estimator is shown in Figure 27. The standard deviations of the horizontal position errors are significantly greater than those of Case V. These are in the same scale as in Case IV, so Figure 27 uses the same axis scaling as Figure 24. Unlike Case IV, the values of σ_{Filter} and σ_{True} for the horizontal errors continue to increase due to the growth in the level of a , in the same manner as seen in Case V.

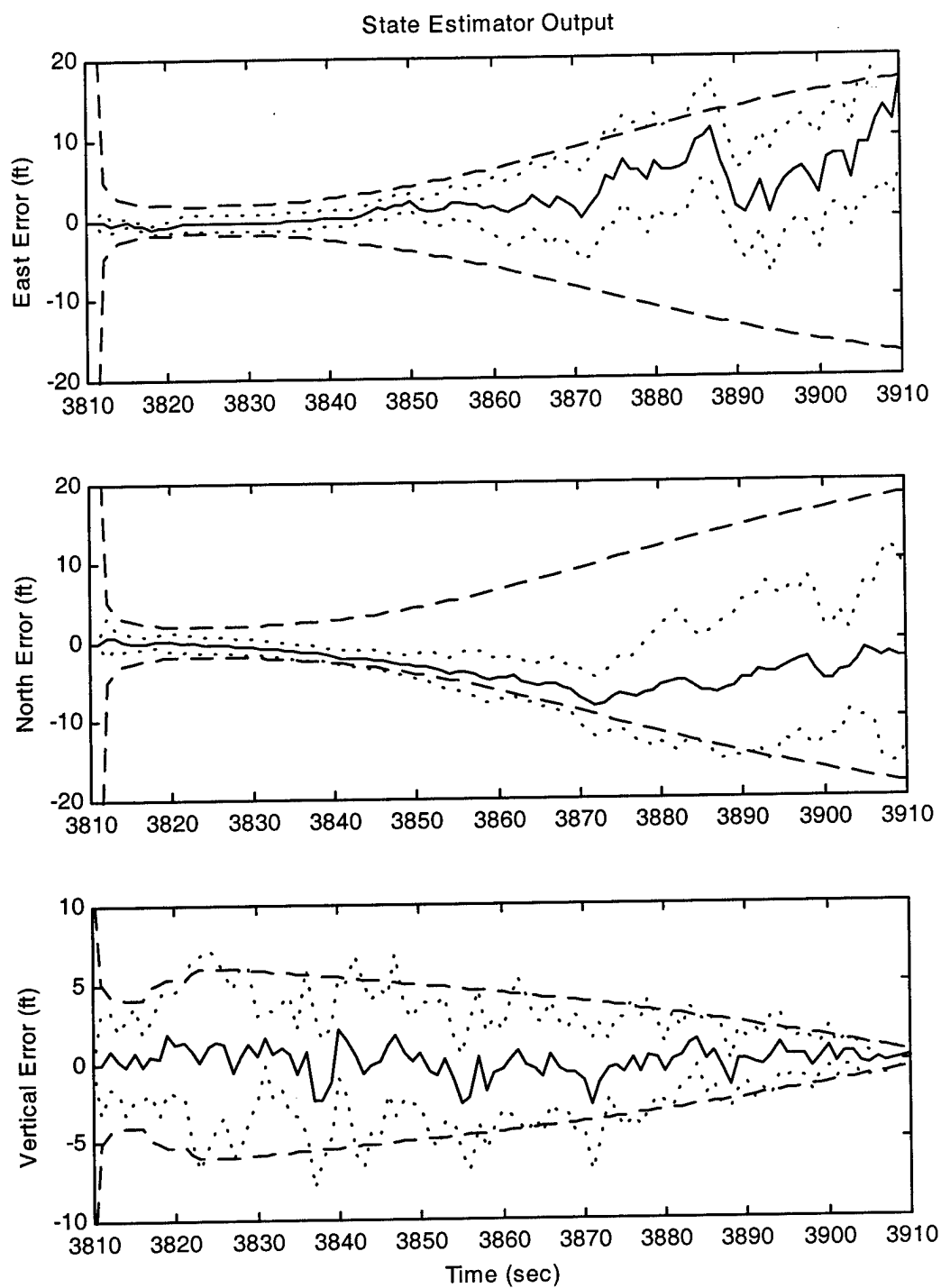


Figure 27. Case VI: State Estimator Position Errors

Tables 21 – 23 show the values of σ_{Filter} and σ_{True} the DH points. As in Case IV, the value of σ_{Filter} meets Category III in the vertical direction and only Category I in the horizontal directions. The values of σ_{True} meet Category III specifications in the vertical direction; however, they can only meet Category II specifications in the horizontal directions. The filter-computed standard deviation, σ_{Filter} , is more conservative than the standard deviation over the Monte Carlo runs, σ_{True} , as usual. As in Case IV, the quality of the INS has a prominent effect on the position errors in the presence of measurement noise. This also emphasizes the importance of having an INS of good quality on board when GPS measurements are disrupted.

Table 21. Case VI: East Position Error Standard Deviations

| ILS Category | DH (ft) | σ_{Filter} (ft) | σ_{True} (ft) |
|--------------|---------|------------------------|----------------------|
| I | 200 | 14.46 | 7.724 |
| II | 100 | 15.86 | 6.208 |
| III | 50 | 16.68 | 8.983 |

Table 22. Case VI: North Position Error Standard Deviations

| ILS Category | DH (ft) | σ_{Filter} (ft) | σ_{True} (ft) |
|--------------|---------|------------------------|----------------------|
| I | 200 | 15.23 | 10.29 |
| II | 100 | 16.81 | 7.921 |
| III | 50 | 17.74 | 12.64 |

Table 23. Case VI: Vertical Position Error Standard Deviations

| ILS Category | DH (ft) | σ_{Filter} (ft) | σ_{True} (ft) |
|--------------|---------|------------------------|----------------------|
| I | 200 | 2.017 | 1.942 |
| II | 100 | 1.273 | 0.923 |
| III | 50 | 0.800 | 0.829 |

4.9. Decreasing Noise Levels Scenarios

In the last two cases, the system performance is examined against a scenario where the level of GPS pseudorange measurement noise starts at the level where GPS is ineffective. As the trajectory progresses, the interference decreases to a nominal level as the aircraft approaches the touch-down point. The level of a decreases in inverse proportion to the square of the distance to the RF interference source, as in Cases V and VI. Also, the source is assumed to be in-line with the flight path of the aircraft. Table 24 shows the how a varies over this scenario.

Table 24. Decreasing Noise Levels Scenario

| Interval Start Time (sec) | Actual Parameter (a) |
|--|--|
| 3,810 | 2,000.0 |
| 3,820 | 1,760.0 |
| 3,825 | 1,530.0 |
| 3,830 | 1,320.0 |
| 3,835 | 1,125.0 |
| 3,840 | 945.0 |
| 3,845 | 780.0 |
| 3,850 | 630.0 |
| 3,855 | 500.0 |
| 3,860 | 380.0 |
| 3,865 | 280.0 |
| 3,870 | 195.0 |
| 3,875 | 125.0 |
| 3,880 | 70.0 |
| 3,885 | 30.0 |
| 3,890 | 8.0 |
| 3,895 | 1.0 |

4.9.1. Case VII

As with the other odd-numbered cases, this case involves the navigation system using the 0.4 nmi/hr drift rate INS. Figure 28 shows how \hat{a} and p_k vary over the scenario. As in Case V, the value of \hat{a} follows a throughout the scenario with a lag. The effect of this is that \hat{a} tends to be greater than a , except during the beginning of the scenario (\hat{a} tended to be less than a in previous scenario where a was increasing due to $a_5 < 2,000$). The value of \hat{a} reaches the upper bound just under a_5 by the time a drops to 1,530. Up to the time of 3,880 seconds in the scenario, blending is achieved within the MMAE as the probability plots of the a_2 , a_3 , a_4 , and a_5 elemental filters show. From 3,880 to 3,895 seconds of the scenario, the MMAE favors the a_2 elemental filter almost exclusively, as in Case V, when the values of a was between a_1 and a_2 . After that point, when a reaches the nominal level of 1, the MMAE readjusts \hat{a} within 5 seconds.

Figure 29 shows the positions errors according to the M³AE's state estimator. The values of σ_{Filter} and σ_{True} decrease, as the state estimator adapts to account for the decrease in a as the scenario progresses. Note that the scale of the horizontal error plots is greater than in previous figures, to show the entire range of how the errors and their standard deviations vary. Overall, the values of σ_{True} stay within the σ_{Filter} bounds, showing that the state estimator filter performs adequately.

Tables 25 – 27 show the values of σ_{Filter} and σ_{True} at each DH. For both the σ_{Filter} and σ_{True} in vertical and horizontal directions, Category III is satisfied. Despite a high level of interference at the beginning of the scenario, the state estimator, provided with updated values of \hat{a} , can perform well enough to meet Category III. This indicates that the effects

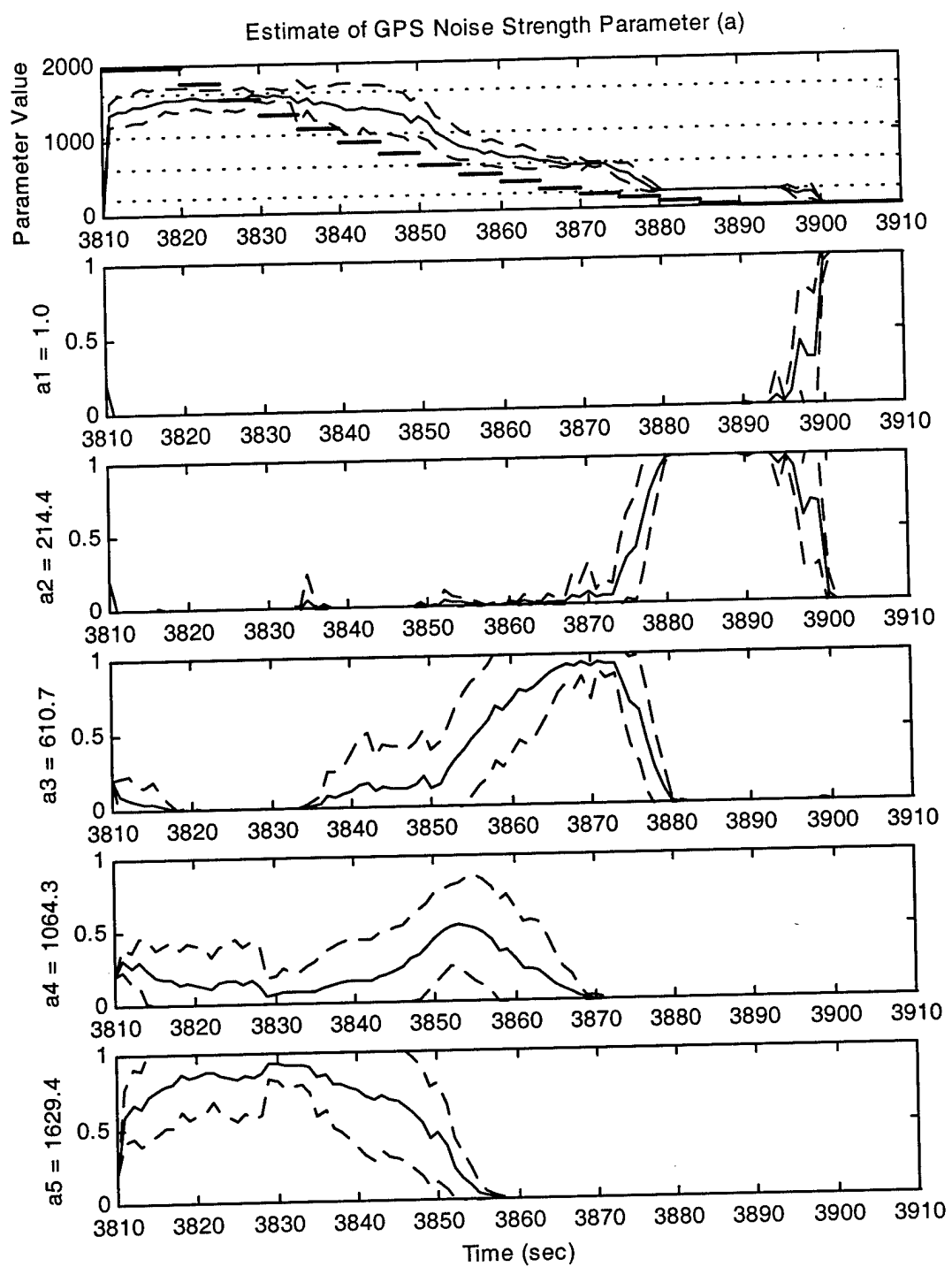


Figure 28. Case VII: Estimated Parameter and Elemental Filter Probabilities

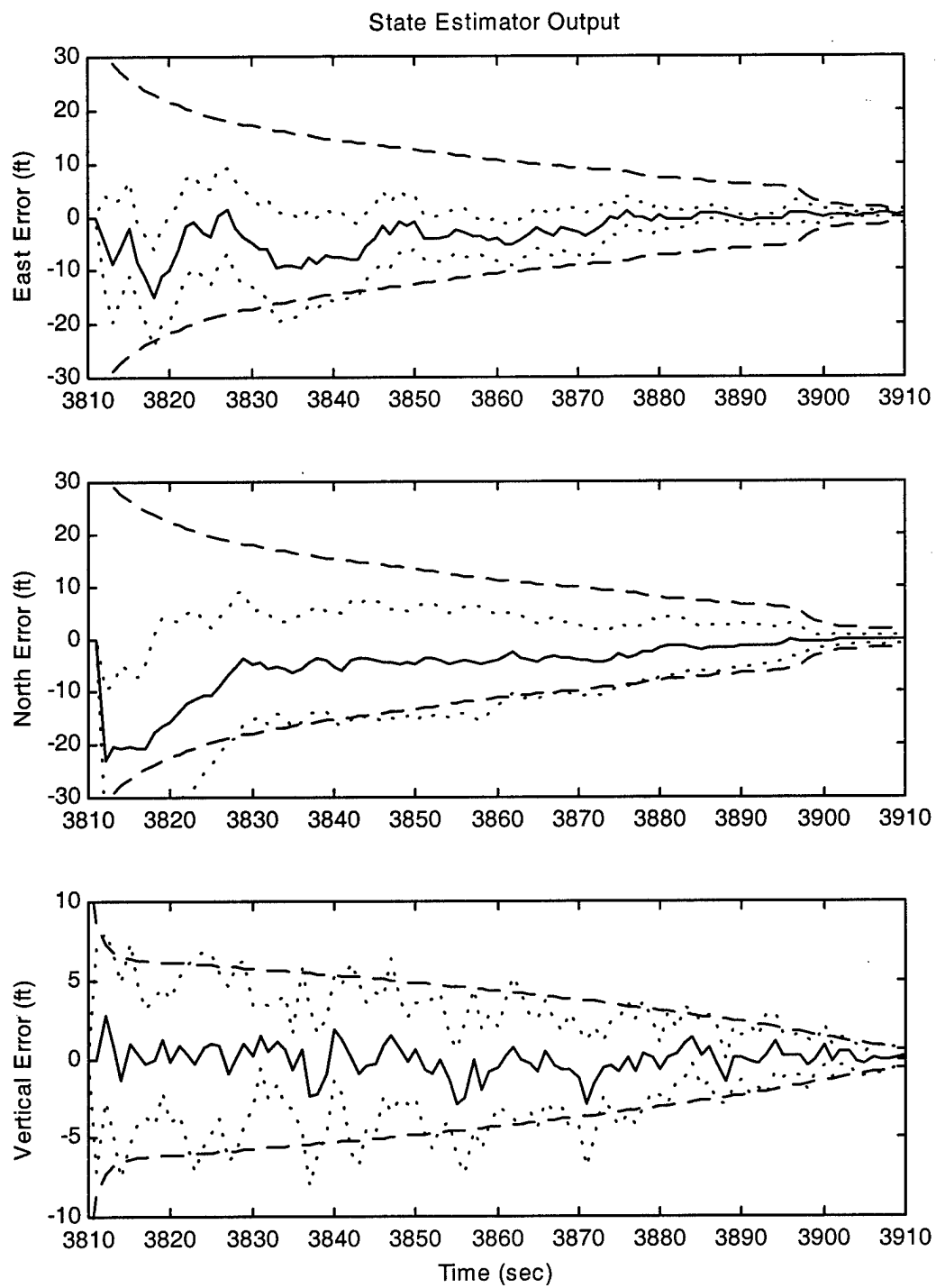


Figure 29. Case VII: State Estimator Position Errors

Table 25. Case VII: East Position Error Standard Deviations

| ILS Category | DH (ft) | σ_{Filter} (ft) | σ_{True} (ft) |
|--------------|---------|------------------------|----------------------|
| I | 200 | 5.507 | 0.936 |
| II | 100 | 1.858 | 0.701 |
| III | 50 | 1.509 | 0.582 |

Table 26. Case VII: North Position Error Standard Deviations

| ILS Category | DH (ft) | σ_{Filter} (ft) | σ_{True} (ft) |
|--------------|---------|------------------------|----------------------|
| I | 200 | 5.982 | 3.183 |
| II | 100 | 2.068 | 0.888 |
| III | 50 | 1.665 | 0.838 |

Table 27. Case VII: Vertical Position Error Standard Deviations

| ILS Category | DH (ft) | σ_{Filter} (ft) | σ_{True} (ft) |
|--------------|---------|------------------------|----------------------|
| I | 200 | 1.886 | 1.435 |
| II | 100 | 1.146 | 0.719 |
| III | 50 | 0.710 | 0.798 |

of increased pseudorange measurement noise do not linger within the filters' calculations long enough to affect the outcomes, if the noise variance returns to a nominal level soon before touch-down.

4.9.2. Case VIII

This case is identical to Case VII, except for the 4.0 nmi/hr drift rate INS. As with the other even-numbered cases, the plots of \hat{a} and p_k are essentially identical to its previous case (see Figure 28). Figure 30 shows the positions errors determined by the M³AE's state estimator. The only notable feature is that σ_{Filter} for the horizontal position errors remains at a higher level than in Case VII from 3,870 to 3,890 seconds in the

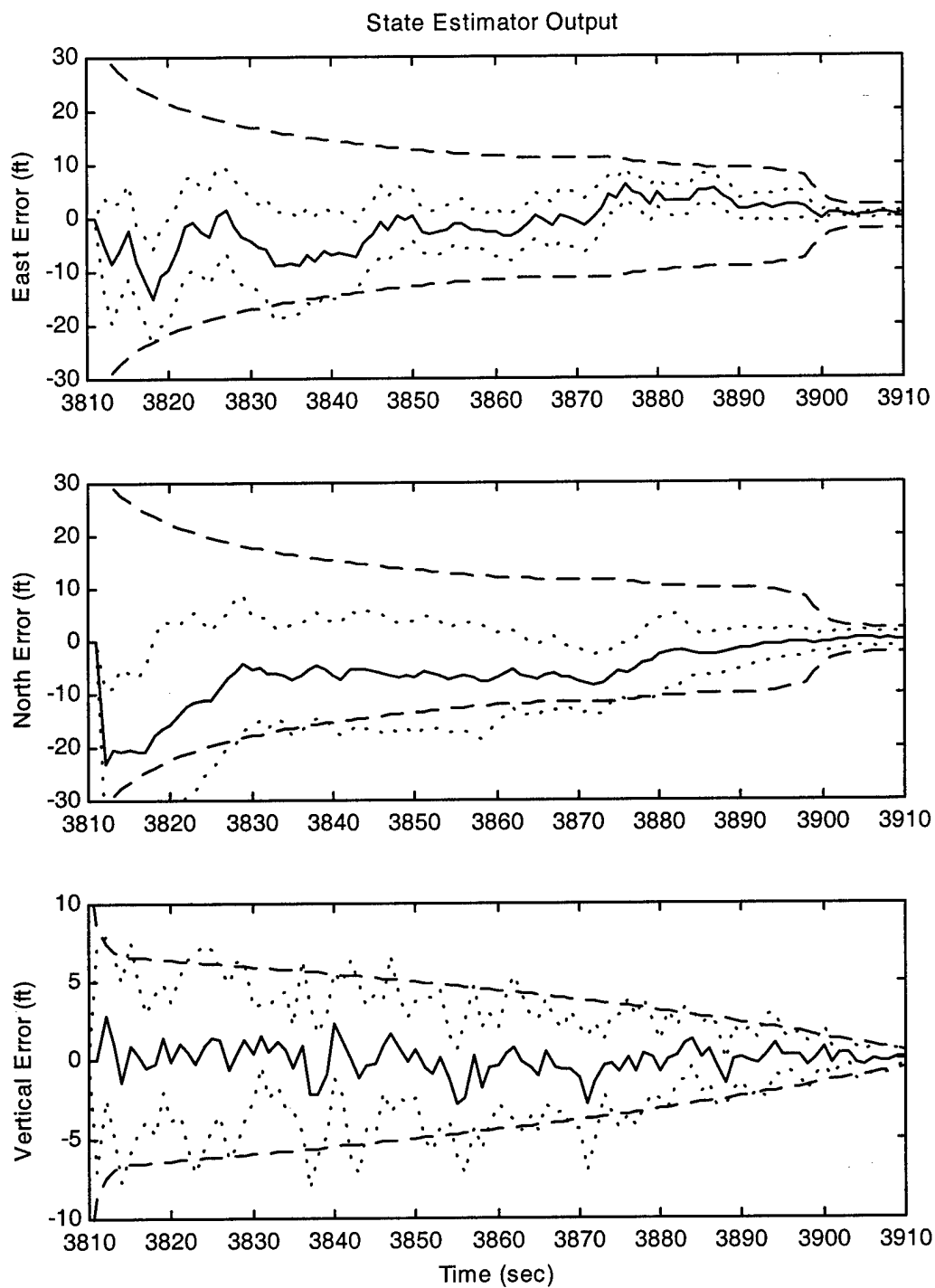


Figure 30. Case VIII: State Estimator Position Errors

scenario. Otherwise, the navigation system demonstrates a performance similar to that in Case VII.

Tables 28 – 30 show the values of σ_{Filter} and σ_{True} at the DH points. Although the values of σ_{Filter} and σ_{True} at the DH points are greater than in Case VII, Category III is satisfied, in both the vertical and horizontal directions. As with Case VII, the effects of increased measurement noise do not persist if a nominal level is reached in reasonably short time prior to touch-down.

Table 28. Case VIII: East Position Error Standard Deviations

| ILS Category | DH (ft) | σ_{Filter} (ft) | σ_{True} (ft) |
|--------------|---------|------------------------|----------------------|
| I | 200 | 8.965 | 2.495 |
| II | 100 | 2.691 | 0.587 |
| III | 50 | 2.210 | 0.679 |

Table 29. Case VIII: North Position Error Standard Deviations

| ILS Category | DH (ft) | σ_{Filter} (ft) | σ_{True} (ft) |
|--------------|---------|------------------------|----------------------|
| I | 200 | 9.602 | 2.713 |
| II | 100 | 2.979 | 1.767 |
| III | 50 | 2.423 | 1.524 |

Table 30. Case VIII: Vertical Position Error Standard Deviations

| ILS Category | DH (ft) | σ_{Filter} (ft) | σ_{True} (ft) |
|--------------|---------|------------------------|----------------------|
| I | 200 | 2.009 | 1.939 |
| II | 100 | 1.248 | 0.891 |
| III | 50 | 0.793 | 0.825 |

4.10. Summary

The test cases presented in this chapter covered four different pseudorange measurement noise scenarios using the flight profile of a simulated landing for a KC-135 tanker aircraft. Table 31 summarizes the results of all the test cases. The minimum ILS category each case can satisfy is listed, i.e., the worst performance between the horizontal and vertical position errors, and between the filter-computed standard deviation, σ_{Filter} , and the standard deviation over the Monte Carlo runs, σ_{True} , is used to make this assessment. For most instances, Category III could be met. In the cases which could not, the higher drift rate INS were used and there was a high level of interference near the DH points.

Table 31. ILS Precision Approach Categories Met for each Test Case

| ILS Category | Case I | Case II | Case III | Case IV | Case V | Case VI | Case VII | Case VIII |
|--------------|--------|---------|----------|---------|--------|---------|----------|-----------|
| I | Yes | Yes | Yes | Yes | Yes | Yes | Yes | Yes |
| II | Yes | Yes | Yes | No | Yes | No | Yes | Yes |
| III | Yes | Yes | Yes | No | Yes | No | Yes | Yes |

5. Conclusions and Recommendations

5.1. Overview

The objective of this research effort has been to apply the M³AE architecture to an aircraft precision approach landing where the GPS signals were subjected to interference. The work has focused on calculating accurate data on the aircraft's position throughout its glideslope, and comparing the precision of the data against FAA ILS criteria to assess the performance of the modeled aircraft navigation system. The navigation system models have included an INS with a built-in barometric altimeter, a GPS receiver collecting measurements from 4 GPS SVs and a ground-based pseudolite, and a radar altimeter. This is a direct extension to the research of previous AFIT theses by Gray [13], Britton [7], White [56], and Miller [33].

The modeled system underwent a series of simulations where the measurement noise of the GPS signals varied to depict RF interference. An M³AE architecture was applied to handle the nature of the changing parameter of the noise, yet still produce accurate state estimation. This has been done to attempt to maintain the level of precision in the estimated aircraft's position.

5.2. Conclusions

This research showed that an M³AE provides improvement in estimating both GPS interference levels and aircraft position errors over that obtained in previous research. Several test cases were researched using two INSs of different quality and various interference profiles. The overall performance of each simulation was judged against the

FAA ILS criteria for precision approach. Most of the test cases examined in this research effort satisfied the requirements for a Category III approach. In the cases where the Category III requirements were not met, there was a high level of GPS interference near the landing point and the navigation system was using the poorer quality INS (4.0 nmi/hr drift rate). However, in those cases, Category I requirements were met. When Category III could not be met, it was due to the level of accuracy in the horizontal (east and north) directions. In the horizontal directions, the INS has aiding from GPS measurements only, unlike in the vertical direction, where there are measurements from a barometric altimeter and a radar altimeter as well GPS (recall that INSs inherently have a greater difficulty estimating vertical positions [6, 27], an extremely important concern to all aircraft, thus these instruments are added). The results of the simulations show the significance of the INS drift rate and GPS measurements. Without high-accuracy pseudorange measurements provided by the GPS receiver, the effect of the INS drift rate becomes prominent enough to affect the positioning accuracy at the decision height (DH) points.

Based on the results, the following conclusions can be made:

1. The M^3AE 's MMAE provided good estimates of the interference levels, except at the high interference levels (beyond the boundary of the MMAE's elemental filters) where parameter estimation suffered. This would be readily compensated by allowing an elemental filter to assume the largest interference level of concern. However, navigation performance was not adversely affected.
2. The M^3AE architecture and techniques were validated against a realistic aircraft navigation truth model. The results in this research provide a practical demonstration of M^3AE using truth and filter models of different orders.

3. The level of GPS pseudorange measurement noise had a greater impact on the position errors in the horizontal directions (east and north) than in the vertical direction. This is attributed to the assistance the navigation system derives from other altitude measuring devices that are unaffected by interference in the GPS frequency band, particularly the very accurate radar altimeter.

5.3. Recommendations

The scope of this research encompassed examining the performance of a GPS-aided INS in the presence of GPS interference. As shown, precision approach under the presence of GPS interference was achieved using an M³AE architecture. However, there are several areas that require further research:

1. Develop a more accurate model of interference than the one implemented here.
The effects of a change in the actual power of RF noise should be represented by a more detailed algorithm.
2. Implement a moving-bank MMAE architecture, developed by Vasquez [54, 55], in place of the fixed-bank MMAE parameter estimator to investigate the differences in performance.
3. Generate several different flight profiles to examine the effects of maneuvering during the landing approach phase of flight.
4. Perform the constrained parameter discretization fixing filters at $a_1 = 1$ and $a_K = 2,000$ (where there are K filters in the MMAE).
5. Incorporate logic where, if $p_k = 1 - (K-1)p_{min}$, then $p_k = 1$ and $p_j = 0 \forall j \neq k \ni j \in \{1, 2, \dots, K\}$ is sent the output of the MMAE.

Appendix A. Acronym List

| | |
|-------------------|---|
| AFIT | Air Force Institute of Technology |
| AGL | Above Ground Level |
| DGPS | Differential GPS |
| DH | Decision Height |
| ECEF | Earth-Centered, Earth-Fixed (reference frame) |
| EKF | Extended Kalman Filter |
| FAA | Federal Aviation Administration |
| GPS | Global Positioning System |
| ILS | Instrument Landing System |
| INS | Inertial Navigation System |
| IRDF | Inter-Residual Distance Feedback |
| LAAS | Local Area Augmentation System |
| MSOFE | Multi-mode Simulation of Optimal Filter Equations |
| MMSOFE | Multiple Model Simulation of Optimal Filter Equations |
| MMAE | Multiple Model Adaptive Estimator |
| M ³ AE | Modified Multiple Model Adaptive Estimator |
| PLS | Precision Landing System |
| PPS | Precise Positioning Service |
| PR | Pseudorange |
| RF | Radio Frequency |
| SA | Selective Availability |
| SP | Standard Positioning Service |
| SV | Space Vehicle |
| TACAN | Tactical Air Navigation |
| UHF | Ultra High Frequency |
| VHF | Very High Frequency |
| VOR | VHF Omnidirectional Range |
| WGN | White Gaussian Noise |
| WGS-84 | World Geodetic Survey 1984 |

Appendix B. Error States of the Truth and Filter Models

This appendix lists the error states implemented by the truth and filter models considered in this research. Tables 32 – 34 show a complete list of the 93 error states that comprise the Litton LN-93 INS truth model [26]. Tables 35 and 36 list the 39 error states of the reduced-order truth model used in the simulations [7, 13, 38, 56, 57]. These consist of a proper subset of the original LN-93 states, i.e., every state in the reduced-order truth model is a state in the original truth model. Table 37 lists the 30 error states characterizing a GPS truth model using 4 SVs and 1 receiver [7, 13, 38, 56, 57]. Table 38 lists the 22 error states associated with a DGPS truth model; these form a proper subset of the GPS states [7, 13, 38, 56, 57]. Table 39 lists the 13-state filter model, consisting of 11 INS error states and the 2 error states related to the GPS receiver [7, 13, 38, 56, 57].

Table 32. Original 93-State Truth Model for the INS: States 1 - 31

| State Number | State Symbol | State Definition |
|--------------|------------------|--|
| 1 | $\delta\theta_x$ | X-component of vector angle from true to computer frame |
| 2 | $\delta\theta_y$ | Y-component of vector angle from true to computer frame |
| 3 | $\delta\theta_z$ | Z-component of vector angle from true to computer frame |
| 4 | ϕ_x | X-component of vector angle from true to platform frame |
| 5 | ϕ_y | Y-component of vector angle from true to platform frame |
| 6 | ϕ_z | Z-component of vector angle from true to platform frame |
| 7 | δV_x | X-component of error in computed velocity |
| 8 | δV_y | Y-component of error in computed velocity |
| 9 | δV_z | Z-component of error in computed velocity |
| 10 | δh | Error in vehicle altitude above reference ellipsoid |
| 11 | δh_L | Error in lagged inertial altitude |
| 12 | δS_3 | Error in vertical channel aiding state |
| 13 | δS_4 | Error in vertical channel aiding state |
| 14 | b_{x_c} | X-component of gyro correlated drift rate |
| 15 | b_{y_c} | Y-component of gyro correlated drift rate |
| 16 | b_{z_c} | Z-component of gyro correlated drift rate |
| 17 | ∇_{x_c} | X-component of accelerometer and velocity quantizer correlated noise |
| 18 | ∇_{y_c} | Y-component of accelerometer and velocity quantizer correlated noise |
| 19 | ∇_{z_c} | Z-component of accelerometer and velocity quantizer correlated noise |
| 20 | δg_x | X-component of gravity vector errors |
| 21 | δg_y | Y-component of gravity vector errors |
| 22 | δg_z | Z-component of gravity vector errors |
| 23 | δh_B | Total barometric altimeter correlated error |
| 24 | b_{x_t} | X-component of gyro trend |
| 25 | b_{y_t} | Y-component of gyro trend |
| 26 | b_{z_t} | Z-component of gyro trend |
| 27 | ∇_{x_t} | X-component of accelerometer trend |
| 28 | ∇_{y_t} | Y-component of accelerometer trend |
| 29 | ∇_{z_t} | Z-component of accelerometer trend |
| 30 | b_x | X-component of gyro drift rate repeatability |
| 31 | b_y | Y-component of gyro drift rate repeatability |

Table 33. Original 93-State Truth Model for the INS: States 32 - 63

| State Number | State Symbol | State Definition |
|--------------|----------------|--|
| 32 | b_z | Z-component of gyro drift rate repeatability |
| 33 | S_{gx} | X-component of gyro scale factor error |
| 34 | S_{gy} | Y-component of gyro scale factor error |
| 35 | S_{gz} | Z-component of gyro scale factor error |
| 36 | χ_1 | X gyro misalignment about Y-axis |
| 37 | χ_2 | Y gyro misalignment about X-axis |
| 38 | χ_3 | Z gyro misalignment about X-axis |
| 39 | v_1 | X gyro misalignment about Z-axis |
| 40 | v_2 | Y gyro misalignment about Z-axis |
| 41 | v_3 | Z gyro misalignment about Y-axis |
| 42 | D_{xxx} | X gyro scale factor nonlinearity |
| 43 | D_{yyy} | Y gyro scale factor nonlinearity |
| 44 | D_{zzz} | Z gyro scale factor nonlinearity |
| 45 | S_{Qb_x} | X gyro scale factor asymmetry error |
| 46 | S_{Qb_y} | Y gyro scale factor asymmetry error |
| 47 | S_{Qb_z} | Z gyro scale factor asymmetry error |
| 48 | ∇_{b_x} | X-component of accelerometer bias repeatability |
| 49 | ∇_{b_y} | Y-component of accelerometer bias repeatability |
| 50 | ∇_{b_z} | Z-component of accelerometer bias repeatability |
| 51 | S_{Ax} | X-component of accelerometer and velocity quantizer scale factor |
| 52 | S_{Ay} | Y-component of accelerometer and velocity quantizer scale factor |
| 53 | S_{Az} | Z-component of accelerometer and velocity quantizer scale factor |
| 54 | S_{QAx} | X-component of accelerometer and velocity quantizer scale factor asymmetry |
| 55 | S_{QAy} | Y-component of accelerometer and velocity quantizer scale factor asymmetry |
| 56 | S_{QAz} | Z-component of accelerometer and velocity quantizer scale factor asymmetry |
| 57 | f_{xx} | Coefficient of error proportional to square of measured acceleration |
| 58 | f_{yy} | Coefficient of error proportional to square of measured acceleration |
| 59 | f_{zz} | Coefficient of error proportional to square of measured acceleration |
| 60 | f_{xy} | Coefficient of error proportional to square of measured acceleration |
| 61 | f_{xz} | Coefficient of error proportional to square of measured acceleration |
| 62 | f_{yx} | Coefficient of error proportional to square of measured acceleration |
| 63 | f_{yz} | Coefficient of error proportional to square of measured acceleration |

Table 34. Original 93-State Truth Model for the INS: States 64 - 93

| State Number | State Symbol | State Definition |
|--------------|----------------|--|
| 64 | f_{zz} | Coefficient of error proportional to square of measured acceleration |
| 65 | f_{zy} | Coefficient of error proportional to square of measured acceleration |
| 66 | μ_1 | X accelerometer misalignment about Z-axis |
| 67 | μ_2 | Y accelerometer misalignment about Z-axis |
| 68 | μ_3 | Z accelerometer misalignment about Y-axis |
| 69 | σ_3 | Z accelerometer misalignment about Y-axis |
| 70 | ∇_{x_q} | X-component of accelerometer bias thermal transient |
| 71 | ∇_{y_q} | Y-component of accelerometer bias thermal transient |
| 72 | ∇_{z_q} | Z-component of accelerometer bias thermal transient |
| 73 | b_{x_q} | X-component of initial gyro drift rate bias thermal transient |
| 74 | b_{y_q} | Y-component of initial gyro drift rate bias thermal transient |
| 75 | b_{z_q} | Z-component of initial gyro drift rate bias thermal transient |
| 76 | F_{xyz} | X gyro compliance term |
| 77 | F_{xyy} | X gyro compliance term |
| 78 | F_{xyx} | X gyro compliance term |
| 79 | F_{xzy} | X gyro compliance term |
| 80 | F_{xzz} | X gyro compliance term |
| 81 | F_{xz} | X gyro compliance term |
| 82 | F_{yzx} | Y gyro compliance term |
| 83 | F_{yzz} | Y gyro compliance term |
| 84 | F_{yzy} | Y gyro compliance term |
| 85 | F_{yxz} | Y gyro compliance term |
| 86 | F_{yxx} | Y gyro compliance term |
| 87 | F_{yxy} | Y gyro compliance term |
| 88 | F_{zxy} | Z gyro compliance term |
| 89 | F_{zxx} | Z gyro compliance term |
| 90 | F_{zxz} | Z gyro compliance term |
| 91 | F_{zyx} | Z gyro compliance term |
| 92 | F_{zyy} | Z gyro compliance term |
| 93 | F_{zyz} | Z gyro compliance term |

Table 35. Reduced-Order 39-State Truth Model for the INS: States 1 - 20

| State Number | State Symbol | State Definition |
|--------------|------------------|--|
| 1 | $\delta\theta_x$ | X-component of vector angle from true to computer frame |
| 2 | $\delta\theta_y$ | Y-component of vector angle from true to computer frame |
| 3 | $\delta\theta_z$ | Z-component of vector angle from true to computer frame |
| 4 | ϕ_x | X-component of vector angle from true to platform frame |
| 5 | ϕ_y | Y-component of vector angle from true to platform frame |
| 6 | ϕ_z | Z-component of vector angle from true to platform frame |
| 7 | δV_x | X-component of error in computed velocity |
| 8 | δV_y | Y-component of error in computed velocity |
| 9 | δV_z | Z-component of error in computed velocity |
| 10 | δh | Error in vehicle altitude above reference ellipsoid |
| 11 | δh_B | Total barometric altimeter correlated error |
| 12 | δh_L | Error in lagged inertial altitude |
| 13 | δS_3 | Error in vertical channel aiding state |
| 14 | δS_4 | Error in vertical channel aiding state |
| 15 | ∇_{x_c} | X-component of accelerometer and velocity quantizer correlated noise |
| 16 | ∇_{y_c} | Y-component of accelerometer and velocity quantizer correlated noise |
| 17 | ∇_{z_c} | Z-component of accelerometer and velocity quantizer correlated noise |
| 18 | δg_x | X-component of gravity vector errors |
| 19 | δg_y | Y-component of gravity vector errors |
| 20 | δg_z | Z-component of gravity vector errors |

Table 36. Reduced-Order 39-State Truth Model for the INS: States 21 - 39

| State Number | State Symbol | State Definition |
|--------------|----------------|--|
| 21 | b_x | X-component of gyro drift rate repeatability |
| 22 | b_y | Y-component of gyro drift rate repeatability |
| 23 | b_z | Z-component of gyro drift rate repeatability |
| 24 | S_{gx} | X-component of gyro scale factor error |
| 25 | S_{gy} | Y-component of gyro scale factor error |
| 26 | S_{gz} | Z-component of gyro scale factor error |
| 27 | ∇_{b_x} | X-component of accelerometer bias repeatability |
| 28 | ∇_{b_y} | Y-component of accelerometer bias repeatability |
| 29 | ∇_{b_z} | Z-component of accelerometer bias repeatability |
| 30 | S_{Ax} | X-component of accelerometer and velocity quantizer scale factor |
| 31 | S_{Ay} | Y-component of accelerometer and velocity quantizer scale factor |
| 32 | S_{Az} | Z-component of accelerometer and velocity quantizer scale factor |
| 33 | S_{QAx} | X-component of accelerometer and velocity quantizer scale factor asymmetry |
| 34 | S_{QAy} | Y-component of accelerometer and velocity quantizer scale factor asymmetry |
| 35 | S_{QAz} | Z-component of accelerometer and velocity quantizer scale factor asymmetry |
| 36 | μ_1 | X accelerometer misalignment about Z-axis |
| 37 | μ_2 | Y accelerometer misalignment about Z-axis |
| 38 | μ_3 | Z accelerometer misalignment about Y-axis |
| 39 | σ_3 | Z accelerometer misalignment about X-axis |

Table 37. 30-State Truth Model for GPS

| State Number | State Symbol | State Definition |
|--------------|--------------------|------------------------------------|
| 1 | δR_{Uclk} | User clock bias |
| 2 | δD_{Uclk} | User clock drift |
| 3 | δR_{MP1} | SV 1 multi-path error |
| 4 | δR_{trop1} | SV 1 tropospheric error |
| 5 | δR_{ion1} | SV 1 ionospheric error |
| 6 | δR_{sclk1} | SV 1 clock error |
| 7 | δx_{SV1} | SV 1 x-component of position error |
| 8 | δy_{SV1} | SV 1 y-component of position error |
| 9 | δz_{SV1} | SV 1 z-component of position error |
| 10 | δR_{MP2} | SV 2 multi-path error |
| 11 | δR_{trop2} | SV 2 tropospheric error |
| 12 | δR_{ion2} | SV 2 ionospheric error |
| 13 | δR_{sclk2} | SV 2 clock error |
| 14 | δx_{SV2} | SV 2 x-component of position error |
| 15 | δy_{SV2} | SV 2 y-component of position error |
| 16 | δz_{SV2} | SV 2 z-component of position error |
| 17 | δR_{MP3} | SV 3 multi-path error |
| 18 | δR_{trop3} | SV 3 tropospheric error |
| 19 | δR_{ion3} | SV 3 ionospheric error |
| 20 | δR_{sclk3} | SV 3 clock error |
| 21 | δx_{SV3} | SV 3 x-component of position error |
| 22 | δy_{SV3} | SV 3 y-component of position error |
| 23 | δz_{SV3} | SV 3 z-component of position error |
| 24 | δR_{MP4} | SV 4 multi-path error |
| 25 | δR_{trop4} | SV 4 tropospheric error |
| 26 | δR_{ion4} | SV 4 ionospheric error |
| 27 | δR_{sclk4} | SV 4 clock error |
| 28 | δx_{SV4} | SV 4 x-component of position error |
| 29 | δy_{SV4} | SV 4 y-component of position error |
| 30 | δz_{SV4} | SV 4 z-component of position error |

Table 38. 22-State Truth Model for Differential GPS

| State Number | State Symbol | State Definition |
|--------------|--------------------|------------------------------------|
| 1 | δR_{Uclk} | User clock bias |
| 2 | δD_{Uclk} | User clock drift |
| 3 | δR_{trop1} | SV 1 tropospheric error |
| 4 | δR_{ion1} | SV 1 ionospheric error |
| 5 | δx_{SV1} | SV 1 x-component of position error |
| 6 | δy_{SV1} | SV 1 y-component of position error |
| 7 | δz_{SV1} | SV 1 z-component of position error |
| 8 | δR_{trop2} | SV 2 tropospheric error |
| 9 | δR_{ion2} | SV 2 ionospheric error |
| 10 | δx_{SV2} | SV 2 x-component of position error |
| 11 | δy_{SV2} | SV 2 y-component of position error |
| 12 | δz_{SV2} | SV 2 z-component of position error |
| 13 | δR_{trop3} | SV 3 tropospheric error |
| 14 | δR_{ion3} | SV 3 ionospheric error |
| 15 | δx_{SV3} | SV 3 x-component of position error |
| 16 | δy_{SV3} | SV 3 y-component of position error |
| 17 | δz_{SV3} | SV 3 z-component of position error |
| 18 | δR_{trop4} | SV 4 tropospheric error |
| 19 | δR_{ion4} | SV 4 ionospheric error |
| 20 | δx_{SV4} | SV 4 x-component of position error |
| 21 | δy_{SV4} | SV 4 y-component of position error |
| 22 | δz_{SV4} | SV 4 z-component of position error |

Table 39. 13-State Filter Model (for all navigation components)

| State Number | State Symbol | State Definition |
|--------------|-------------------|---|
| 1 | $\delta\theta_x$ | X-component of vector angle from true to computer frame |
| 2 | $\delta\theta_y$ | Y-component of vector angle from true to computer frame |
| 3 | $\delta\theta_z$ | Z-component of vector angle from true to computer frame |
| 4 | ϕ_x | X-component of vector angle from true to platform frame |
| 5 | ϕ_y | Y-component of vector angle from true to platform frame |
| 6 | ϕ_z | Z-component of vector angle from true to platform frame |
| 7 | δV_x | X-component of error in computed velocity |
| 8 | δV_y | Y-component of error in computed velocity |
| 9 | δV_z | Z-component of error in computed velocity |
| 10 | δh | Error in vehicle altitude above reference ellipsoid |
| 11 | δh_B | Total barometric altimeter correlated error |
| 12 | δR_{Uclk} | User clock bias |
| 13 | δD_{Uclk} | User clock drift |

Appendix C. Truth Model System Dynamics and Process Noise Matrices

The LN-93 [26] error-state system dynamics matrix, \mathbf{F} , is a 93×93 matrix with numerous zero elements. This matrix is parsed out into portions (submatrices) that contain non-zero elements, see Equations (64) and (65). The submatrices of the reduced-order truth matrix \mathbf{F} develop by Negast [38] are shown in Tables 40 – 44. A complete listing of the 93-state system dynamics matrix can be found in the Litton's reference [26] as well in theses at AFIT [38, 56]. The system dynamics model for the single-positioning GPS and DGPS models are contained within Section 3.5.

The Litton LN-93 truth model also includes a 93×93 process noise matrix, \mathbf{Q} [26]. As shown in Equations (64) and (65), the WGN process noise vector, \mathbf{w} , was subdivided into subvectors, \mathbf{w}_1 and \mathbf{w}_2 , corresponding to the error state subvectors, $\delta\mathbf{x}_1$ and $\delta\mathbf{x}_2$. These noise subvectors have process noise covariance (strength) matrices described by \mathbf{Q}_{11} and \mathbf{Q}_{22} listed in Tables 45 and 46. The process noise submatrices for the GPS truth models are contained within Section 3.5.

Table 40. Elements of the System Dynamics Submatrix, F_{11}

| Element | Term | Element | Term |
|---------|-----------------------------------|---------|----------------------------------|
| (1,3) | $-\rho_y$ | (1,8) | $-C_{RY}$ |
| (2,3) | ρ_x | (2,7) | C_{RX} |
| (3,1) | ρ_y | (3,2) | $-\rho_x$ |
| (4,2) | $-\Omega_z$ | (4,3) | Ω_y |
| (4,5) | ω_{in_z} | (4,6) | $-\omega_{in_y}$ |
| (4,8) | $-C_{RY}$ | (5,1) | Ω_z |
| (5,3) | $-\Omega_x$ | (5,4) | $-\omega_{in_z}$ |
| (5,6) | ω_{in_x} | (5,7) | C_{RX} |
| (6,1) | $-\Omega_y$ | (6,2) | Ω_x |
| (6,4) | ω_{in_y} | (6,5) | $-\omega_{in_x}$ |
| (7,1) | $-2V_y\Omega_y - 2V_z\Omega_z$ | (7,2) | $2V_y\Omega_x$ |
| (7,3) | $2V_z\Omega_x$ | (7,5) | $-A_z$ |
| (7,6) | A_y | (7,7) | $-V_zC_{RX}$ |
| (7,8) | $2\Omega_z$ | (7,9) | $-\rho_y - 2\Omega_y$ |
| (8,1) | $2V_x\Omega_y$ | (8,2) | $-2V_x\Omega_x - 2V_z\Omega_z$ |
| (8,3) | $2V_z\Omega_y$ | (8,4) | A_z |
| (8,6) | $-A_x$ | (8,7) | $-2\Omega_z$ |
| (8,8) | $-V_zC_{RY}$ | (8,9) | $\rho_x + 2\Omega_x$ |
| (9,1) | $2V_x\Omega_z$ | (9,2) | $2V_y\Omega_z$ |
| (9,3) | $-2V_y\Omega_y - 2V_x\Omega_x$ | (9,4) | $-A_y$ |
| (9,5) | A_x | (9,7) | $\rho_y + 2\Omega_y + V_xC_{RX}$ |
| (9,8) | $-\rho_x - 2\Omega_x + V_yC_{RY}$ | (9,10) | $2g_o / a$ |
| (9,14) | $-k_2$ | (9,12) | -1 |
| (9,16) | k_2 | (10,9) | 1 |
| (10,14) | $-k_1$ | (10,16) | $k_1 - 1$ |
| (14,10) | 1 | (14,14) | -1 |
| (15,14) | k_3 | (15,16) | $-k_3$ |
| (16,10) | k_4 | (16,14) | $-k_4$ |
| (16,16) | $k_4 - 1$ | | |

- $\rho_{x,y}$ = Components of angular rate, navigation frame to ECEF frame
 $\Omega_{x,y,z}$ = Components of angular rate, ECEF to inertial frame
 $\omega_{in_{x,y,z}}$ = Components of angular rate, navigation frame to inertial frame
 $V_{x,y,z}$ = Components of vehicle velocity vector in ECEF coordinates
 $A_{x,y,z}$ = Components of specific force in sensor frame
 $k_{1,2,3,4}$ = Vertical channel gains
 a = Equatorial radius of the earth (20,926,470 ft)
 $C_{RX,RY}$ = Components of earth spheroid inverse radii of curvature
 g_o = Equatorial gravity (32.08744 ft/sec²)

Table 41. Elements of the System Dynamics Submatrix, F_{12}

| Element | Term | Element | Term | Element | Term |
|---------|-----------|---------|----------|---------|----------|
| (7,17) | C_{11} | (7,18) | C_{12} | (7,19) | C_{13} |
| (7,20) | 1 | (8,17) | C_{21} | (8,18) | C_{22} |
| (8,19) | C_{23} | (8,21) | 1 | (9,17) | C_{31} |
| (9,18) | C_{32} | (9,19) | C_{33} | (9,22) | 1 |
| (9,11) | k_2 | (10,11) | k_1 | (15,11) | $-k_3$ |
| (16,11) | $k_4/600$ | | | | |

Note: For the above element definitions, $t_0 = 0$

C = Coordinate transformation matrix from body frame to navigation frame, C_b^n

Table 42. Elements of the Dynamics Submatrix, F_{13}

| Element | Term | Element | Term | Element | Term |
|---------|-----------------------|---------|-----------------------|---------|-----------------------|
| (4,23) | C_{11} | (4,24) | C_{12} | (4,25) | C_{13} |
| (4,26) | $C_{11}\omega_{in_x}$ | (4,27) | $C_{12}\omega_{in_y}$ | (4,28) | $C_{13}\omega_{in_z}$ |
| (5,23) | C_{21} | (5,24) | C_{22} | (5,25) | C_{23} |
| (5,26) | $C_{21}\omega_{in_x}$ | (5,27) | $C_{22}\omega_{in_y}$ | (5,28) | $C_{23}\omega_{in_z}$ |
| (6,23) | C_{31} | (6,24) | C_{32} | (6,25) | C_{33} |
| (6,26) | $C_{31}\omega_{in_x}$ | (6,27) | $C_{32}\omega_{in_y}$ | (6,28) | $C_{33}\omega_{in_z}$ |

Table 43. Elements of the Dynamics Submatrix, F_{14}

| Element | Term | Element | Term | Element | Term |
|---------|--------------------|---------|--------------------|---------|--------------------|
| (7,29) | C_{11} | (7,30) | C_{12} | (7,31) | C_{13} |
| (7,32) | $C_{11}A_x^B$ | (7,33) | $C_{12}A_y^B$ | (7,34) | $C_{13}A_z^{B'}$ |
| (7,35) | $C_{11} A_x^B $ | (7,36) | $C_{12} A_y^B $ | (7,37) | $C_{13} A_z^{B'} $ |
| (7,38) | $C_{11}A_y^B$ | (7,39) | $-C_{12}A_x^B$ | (7,40) | $C_{13}A_y^B$ |
| (7,41) | $C_{13}A_x^B$ | (8,29) | C_{21} | (8,30) | C_{22} |
| (8,31) | C_{23} | (8,32) | $C_{21}A_x^B$ | (8,33) | $C_{22}A_y^B$ |
| (8,34) | $C_{23}A_z^{B'}$ | (8,35) | $C_{21} A_x^B $ | (8,36) | $C_{22} A_y^B $ |
| (8,37) | $C_{23} A_z^{B'} $ | (8,38) | $C_{21}A_y^B$ | (8,39) | $-C_{22}A_x^B$ |
| (8,40) | $C_{23}A_y^B$ | (8,41) | $C_{23}A_x^B$ | (9,29) | C_{31} |
| (9,30) | C_{32} | (9,31) | C_{33} | (9,32) | $C_{31}A_x^B$ |
| (9,33) | $C_{32}A_y^B$ | (9,34) | $C_{33}A_z^{B'}$ | (9,35) | $C_{31} A_x^B $ |
| (9,36) | $C_{32} A_y^B $ | (9,37) | $C_{33} A_z^{B'} $ | (9,38) | $C_{31}A_y^B$ |
| (9,39) | $-C_{32}A_x^B$ | (9,40) | $C_{33}A_y^B$ | (9,41) | $C_{33}A_x^B$ |

$A_{x,y,z}^B$ = Components of acceleration in the body frame

$A_z^{B'}$ = Specific force component (includes gravity)

Table 44. Elements of the Dynamics Submatrix, F_{22}

| Element | Term | Element | Term | Element | Term |
|---------|-------------------------|---------|-------------------------|---------|-------------------------|
| (17,17) | $-\beta_{\nabla_{x_c}}$ | (18,18) | $-\beta_{\nabla_{y_c}}$ | (19,19) | $-\beta_{\nabla_{z_c}}$ |
| (20,20) | $-\beta_{\delta_{g_x}}$ | (21,21) | $-\beta_{\delta_{g_y}}$ | (22,22) | $-\beta_{\delta_{g_z}}$ |
| (11,11) | $-\beta_{\delta_{n_c}}$ | | | | |

$\beta_{b_{x_c, y_c, z_c}}$ = Gyro inverse correlation time constants (5 min)

$\beta_{\nabla_{x_c, y_c, z_c}}$ = Accelerometer inverse correlation time constants (5 min)

$\beta_{\delta_{g_x, y, z}}$ = Gravity vector error inverse correlation time constants (V/20NM)

$\beta_{\delta_{n_c}}$ = Barometer inverse correlation time (10 min)

Table 45. Elements of Process Noise Submatrix Q_{11}

| Element | Term | Element | Term |
|---------|-------------------------|---------|-------------------------|
| (4,4) | $\sigma_{\eta_{b_x}}^2$ | (5,5) | $\sigma_{\eta_{b_y}}^2$ |
| (6,6) | $\sigma_{\eta_{b_z}}^2$ | (7,7) | $\sigma_{\eta_{A_x}}^2$ |
| (8,8) | $\sigma_{\eta_{A_y}}^2$ | (9,9) | $\sigma_{\eta_{A_z}}^2$ |

Table 46. Elements of Process Noise Submatrix Q_{22}

| Element | Term | Element | Term |
|---------|---|---------|---|
| (17,17) | $2\beta_{\nabla_{x_c}} \sigma_{\nabla_{x_c}}^2$ | (18,18) | $2\beta_{\nabla_{y_c}} \sigma_{\nabla_{y_c}}^2$ |
| (19,19) | $2\beta_{\nabla_{z_c}} \sigma_{\nabla_{z_c}}^2$ | (20,20) | $2\beta_{\delta g_x} \sigma_{\delta g_x}^2$ |
| (21,21) | $2\beta_{\delta g_y} \sigma_{\delta g_y}^2$ | (22,22) | $2\beta_{\delta g_z} \sigma_{\delta g_z}^2$ |
| (11,11) | $2\beta_{\delta h_c} \sigma_{\delta h_c}^2$ | | |

- $\sigma_{\eta_{b_{x,y,z}}}^2$ = PSD value of gyro drift rate white noise ($6.25 \times 10^{-10} \frac{\text{deg}^2}{\text{sec}^3}$)
 $\sigma_{\eta_{A_{x,y,z}}}^2$ = PSD value of accelerometer white noise ($1.037 \times 10^{-7} \frac{\text{ft}^2}{\text{sec}^3}$)
 $\sigma_{b_{x_c, y_c, z_c}}^2$ = Variances of gyro drift correlated noise ($3.086 \times 10^{-13} \frac{\text{deg}^2}{\text{sec}^2}$)
 $\sigma_{\nabla_{x_c, y_c, z_c}}^2$ = Variances of accelerometer correlated noise ($4.147 \times 10^{-9} \frac{\text{ft}^2}{\text{sec}^4}$)
 $\sigma_{\delta g_{x,y,z}}^2$ = Variances of gravity vector error component correlated noise ($1.93 \times 10^{-6} \text{deg}^2$)
 $\sigma_{\delta h_c}^2$ = Variance of barometer correlated noise (10,000 ft²)

Appendix D. Filter Model Process and Measurement Noise Matrices

This appendix provides the values of the system dynamics driving noise employed in the M³AE's Kalman filters used in the software simulations. These values are adjusted from the levels specified in the truth model. This is done to compensate for the inadequacies introduced by using a small subset of states to represent the behavior of a higher-order truth model. Tables 47 – 49 below show the diagonal (autocovariance) terms of the process and measurement noise matrices, **Q** and **R**, respectively. Off-diagonal terms (cross-covariance) are assumed to be zero.

Table 47. Process Noise Strength Values (Q) for Filter States (0.4 nmi/hr INS)

| State | DGPS | Units |
|---------------------|-----------------------|-----------------------------------|
| $\delta\theta_x$ | 1.2×10^{-16} | (arc-sec) ² /sec |
| $\delta\theta_y$ | 1.5×10^{-16} | (arc-sec) ² /sec |
| $\delta\theta_z$ | 0.0 | (arc-sec) ² /sec |
| ϕ_x | 20.0 | (arc-sec) ² /sec |
| ϕ_y | 28.0 | (arc-sec) ² /sec |
| ϕ_z | 85.0 | (arc-sec) ² /sec |
| δV_x | 0.1 | ft ² /sec ³ |
| δV_y | 0.1 | ft ² /sec ³ |
| δV_z | 33,000.0 | ft ² /sec ³ |
| δh | 16.0 | ft ² /sec |
| δh_B | 2.0 | ft ² /sec |
| δR_{Uclk_n} | 0.1 | ft ² /sec |
| δD_{Uclk_n} | 5.0×10^{-15} | ft ² /sec ³ |

Table 48. Process Noise Strength Values (Q) for Filter States (4.0 nmi/hr INS)

| State | DGPS | Units |
|---------------------|-----------------------|-----------------------------------|
| $\delta\theta_x$ | 1.2×10^{-23} | (arc-sec) ² /sec |
| $\delta\theta_y$ | 1.5×10^{-23} | (arc-sec) ² /sec |
| $\delta\theta_z$ | 0.0 | (arc-sec) ² /sec |
| ϕ_x | 14,500.0 | (arc-sec) ² /sec |
| ϕ_y | 14,500.0 | (arc-sec) ² /sec |
| ϕ_z | 520.0 | (arc-sec) ² /sec |
| δV_x | 500.0 | ft ² /sec ³ |
| δV_y | 500.0 | ft ² /sec ³ |
| δV_z | 43,000.0 | ft ² /sec ³ |
| δh | 18.0 | ft ² /sec |
| δh_B | 10.0 | ft ² /sec |
| δR_{Uclk_n} | 0.1 | ft ² /sec |
| δD_{Uclk_n} | 5.0×10^{-16} | ft ² /sec ³ |

Table 49. Measurement Noise Strengths Values (R) for the Truth and Filter States

| Measurement | Truth Model Value | Filter Model Value | Units |
|----------------------|-------------------|--------------------|-----------------------------------|
| Barometric Altimeter | 2,500.0 | 3,500.0 | ft ² |
| DGPS | 9.0 | $R_{PR1,2,3,4}$ | ft ² |
| GPS Pseudolite | 1.0 | R_{PR5} | ft ² |
| Radar Altimeter | 0.09 | 0.12 | ft ² /sec ² |

Bibliography

1. Athans, M. and C. B. Chang. *Adaptive Estimation and Parameter Identification Using a Multiple Model Estimation Algorithm*. Technical Note 1976-28: Lincoln Laboratory, Massachusetts Institute of Technology, Lexington, MA, June 1985. ESD-TR-76-184.
2. Bagley, Daniel, T. *GPS/INS Integration for Improved Aircraft Attitude Estimates*. MS Thesis, AFIT/GE/ENG/91D-04, School of Engineering, Air Force Institute of Technology, Wright-Patterson AFB, OH, December 1991.
3. Baram, Yoram. *Information, Consistent Estimation and Dynamic System Identification*. PhD Dissertation, Massachusetts Institute of Technology, Cambridge, MA, November 1976.
4. Bohenek, Brian J. *The Enhanced Performance of an Integrated Navigation System in a Highly Dynamic Environment*. MS Thesis, AFIT/GE/ENG/94D-01, School of Engineering, Air Force Institute of Technology, Wright-Patterson AFB, OH, December 1994.
5. Braff, Ronald, *Description of the FAA's Local Area Augmentation System (LAAS)*. NAVIGATION, Vol. 44, No. 4, Winter 1997-98, pp. 411-424.
6. Britting, Kenneth R. *Inertial Navigation Systems Analysis*. New York: Wiley-Interscience, 1971.
7. Britton, Ryan L. *A Differential GPS Aided INS for Aircraft Landings*. MS Thesis, AFIT/GE/ENG/95D-03, School of Engineering, Air Force Institute of Technology, Wright-Patterson AFB, OH, December 1995.
8. Cheng, David K. *Field and Wave Electromagnetics*, 2nd Ed. Reading, MA: Addison-Wesley Publishing, Inc., 1992.
9. Defense Mapping Agency. *Department of Defense World Geodetic System 1984*. DMA Technical Report, DMA TR 8350.2, 30 September 1987.
10. Department of Transportation. *Automatic Landing Systems*, Federal Aviation Administration, AC 20-57A, Washington, DC, 12 January 1971.
11. Department of Transportation. *Engineering and Operational Issues Associated with the Application of Satellite-Based Navigation to Precision Approach and Landing*, Revision A, NAS System Engineering Service, Federal Aviation Administration, Washington, DC, February 1992.

12. Department of Transportation. *FAR-AIM (Federal Aviation Regulations and Airman's Information Manual) Part 1*, Aviation Supplies & Academics, Inc., Renton, WA, 1993.
13. Gray, Robert A. *An Integrated GPS/INS/BARO and Radar Altimeter System for Aircraft Precision Approach Landings*. MS Thesis, AFIT/GE/ENG/94D-13, School of Engineering, Air Force Institute of Technology, Wright-Patterson AFB, OH, December 1994.
14. Grejner-Brzezinska, Dorota A. "Direct Platform Orientation with Tightly Integrated GPS/INS in Airborne Applications," 1998.
15. Griffin, Gordon C. and Peter S. Maybeck. "MMAE/MMAC Techniques Applied to Large Space Structure Bending with Multiple Uncertain Parameters," *Proceedings of the 34th IEEE Conference on Decision and Control*, New Orleans, LA, 1153-1158, December 1995.
16. Gustafson, John A. and Peter S. Maybeck. "Flexible Spacestructure Control Via Moving-Bank Multiple Model Algorithms," *IEEE Transactions on Aerospace and Electronic Systems*, Vol. 30, No. 3, 750-757, July 1994.
17. Hansen, Neil P. *Incorporation of Carrier-Phase Global Positioning System Measurements into the Navigation Reference System for Improved Performance*. MS Thesis, AFIT/GE/ENG/93D-40, School of Engineering, Air Force Institute of Technology, Wright-Patterson AFB, OH, December 1993.
18. Hartman, Randolph and Don Johnson. *Demonstration of a P(Y)-Code Differential GPS Precision Approach System*. NAVIGATION, Vol. 45, No. 1, Spring 1998, pp. 39-50.
19. Hirning, James L. *Optimal Kalman Filter Integration of a Global Positioning System Receiver and an LN-94 Inertial Navigation System*. MS Thesis, AFIT/GE/ENG/90S-02, School of Engineering, Air Force Institute of Technology, Wright-Patterson AFB, OH, September, 1990.
20. Hong, Lang. Professor of Electrical Engineering, Wright State University, Fairborn, OH, *Course Notes from EE-717 Multisensor Data Fusion*. June 1998.
21. Huangqi, Sun, et al. "An Investigation of Airborne GPS/INS for High Accuracy Position and Velocity Determination," *Proceedings of the Institute of Navigation 1994 National Technical Meeting*, San Diego, CA, 801-809, 24-26 January 1994.
22. Jacob, Thomas. "Landing System Using GPS/IMU System Integration," *Proceedings of the Institute of Navigation 1994 National Technical Meeting*, San Diego, CA, 298-305, 24-26 January 1994.

23. Johnson, Gregory B. *Closed-Loop Performance of GPS Aided INS*. MS Thesis, AFIT/GE/ENG/89D-19, School of Engineering, Air Force Institute of Technology, Wright-Patterson AFB, OH, December 1989.
24. Kalman, R. E. "A New Approach to Linear Filtering and Prediction Problems," *Transactions ASME, Series D: Journal of Basic Engineering*, 82:34-35, 1960.
25. Kaplan, Elliott D. *Understanding GPS, Principles and Applications*. Boston: Artech House, Inc., 1996.
26. Knudsen, L. *Performance Accuracy (Truth Model/Error Budget) Analysis for the LN-93 Inertial Navigation System Inertial Navigation Unit*. Technical Report: Litton Guidance and Control Systems, January 1985. Doc. No. 469414, DID No. Di-S-21433 B/T: CDRL No. 1002.
27. Lewantowicz, Zdzislaw H. and Randall N. Paschall. "Deep Integration of GPS, INS, SAR, and Other Sensor Information," 1995.
28. Lund, Elvind J. *On-line Discrimination and Estimation in Multiple Regime Systems*. PhD Dissertation, Division of Engineering Cybernetics, The Norwegian Institute of Technology, University of Trondheim, Trondheim, Norway, June 1992.
29. Lund, Elvind J., et al. "Multiple Model Estimation with Inter-Residual Distance Feedback," *Modeling, Identification and Control*, Vol. 13, No. 3, 127-140, 1992.
30. Maybeck, Peter S. *Stochastic Models, Estimation and Control, I*. New York: Academic Press, Inc., 1982.
31. Maybeck, Peter S. *Stochastic Models, Estimation and Control, II*. New York: Academic Press, Inc., 1982.
32. Maybeck, Peter S. *Stochastic Models, Estimation and Control, III*. New York: Academic Press, Inc., 1982.
33. Miller, Mikel M. *Modified Multiple Model Adaptive Estimation (M^3AE) for Simultaneous Parameter and State Estimation*. PhD Dissertation, AFIT/GE/ENG/98-02, School of Engineering, Air Force Institute of Technology, Wright-Patterson AFB, OH, March 1998.
34. Mosle, William B. *Detection, Isolation, and Recovery of Failures in an Integrated Navigation System*. MS Thesis, AFIT/GE/ENG/93D-28, School of Engineering, Air Force Institute of Technology, Wright-Patterson AFB, OH, December 1993.
35. Musick, Stanton H. *PROFGEN - A Computer Program for Generating Flight Profiles*. Technical Report, Air Force Avionics Laboratory, Wright-Patterson AFB, OH, November 1976. AFAL-TR-76-247, DTIC ADA034993.

36. Musick, Stanton H. and Neil Carlson. *User's Manual for a Multimode Simulation for Optimal Filter Evaluation (MSOFE)*. Air Force Avionics Laboratory, Wright-Patterson AFB, OH, April 1990. AFWAL-TR-88-1138, AFWAL/AARN-2.
37. NAVSTAR GPS Joint Program Office (SMC/CZ). *NAVSTAR GPS User Equipment Introduction*. Space and Missile Systems Center, Los Angeles AFB, CA. February 1991.
38. Negast, William J. *Incorporation of Differential Global Positioning System Measurements Using an Extended Kalman Filter for Improved Reference System Performance*. MS Thesis, AFIT/GE/ENG/91D-41, School of Engineering, Air Force Institute of Technology, Wright-Patterson AFB, OH, December 1991.
39. Nielsen, Robert L. *Development of a Performance Evaluation Tool (MMSOFE) for Detection of Failures with Multiple Model Adaptive Estimation (MMAE)*. MS Thesis, Wright-Patterson AFB, OH, December 1993.
40. Nisner, Paul and John Owen. "Practical Measurements of Radio Frequency Interference to GPS Receivers and an Assessment of Interference Levels by Flight Trials in the European Regions," *Proceedings of Institute Of Navigation GPS-95, Part I*, 1373-1382, 12-15 September 1995.
41. Parkinson, Bradford W. and Per K. Enge. "Differential GPS." *Global Positioning System: Theory and Applications*., Vol. II, Ch. 1, Washington DC: American Institute of Aeronautics and Astronautics, Inc., 1996.
42. Parkinson, Bradford W., "GPS Error Analysis." *Global Positioning System: Theory and Applications*., Vol. I, Ch. 11, Washington DC: American Institute of Aeronautics and Astronautics, Inc., 1996.
43. Pinson, J. C. "Inertial Guidance for Cruise Vehicles," *Guidance and Control of Aerospace Vehicles* (C. T. Leondes, ed.). McGraw-Hill, NY, 1963.
44. Ritland, John T. "Impact of Inertial System Quality on GPS-Inertial Performance in a Jamming Environment," *Proceedings of the American Institute of Aeronautics and Astronautics*, 1459-1467, 1987.
45. Rowson, Stephen V., et al. "Performance of Category IIIB Automatic Landings Using C/A Code Tracking Differential GPS," *Proceedings of the Institute of Navigation 1994 National Technical Meeting*, San Diego, CA, 759-767, 24-26 January 1994.
46. Schiller, Gregory J. and Peter S. Maybeck. "Space Structure Control Using Multiple Model Adaptive Estimation and Control," *Proceedings of the 13th IFAC Symposium Automatic Control in Aerospace-Aerospace Control '94*, September 1994.

47. Schnedorf, Jerome G., III *Components of the Instrument Landing System*. World Wide Web, <http://home.sprynet.com/sprynet/jayschne/ILs2.htm>, 1997.
48. Sheldon, Stuart N. *An Optimal Parameter Discretization Strategy for Multiple Model Adaptive Estimation and Control*. PhD Dissertation, School of Engineering, Air Force Institute of Technology, Wright-Patterson AFB, OH, December 1989.
49. Sheldon, Stuart N. and Peter S. Maybeck. "An Optimizing Design Strategy for Multiple Model Adaptive Estimation and Control," *IEEE Transactions on Automatic Control*, Vol. 38, No. 4, 651-654, April 1993.
50. Sokol, Charles W. *Performance Evaluation of a GPS-Aided INS in a Filter-Driving-Filter Configuration*. MS Thesis, AFIT/GE/ENG/94M-02, Air Force Institute of Technology, Wright-Patterson AFB, OH, March 1994.
51. Stacey, Richard D. *A Navigation Reference System (NRS) Using Global Positioning System (GPS) and Transponder Aiding*. MS Thesis, AFIT/GE/ENG/91M-04, School of Engineering, Air Force Institute of Technology, Wright-Patterson AFB, OH, March 1991.
52. The MathWorks, Inc., 21 Elliot Street, Natick, MA 01760. *MATLAB*. December 1997. Version 5.2.
53. Vanek, Barry J. *GPS Signal Offset Detection and Noise Strength Estimation in a Parallel Kalman Filter Algorithm*. MS Thesis, AFIT/GE/ENG/99M-30, School of Engineering, Air Force Institute of Technology, Wright-Patterson AFB, OH, In Progress, March 1999.
54. Vasquez, Juan R. *Detection of Spoofing, Jamming, or Failure of a Global Positioning System (GPS)*. MS Thesis, AFIT/GE/ENG/92D-37, School of Engineering, Air Force Institute of Technology, Wright-Patterson AFB, OH, December 1992.
55. Vasquez, Juan R. *New Algorithms for Moving-Bank Multiple Model Adaptive Estimation*. PhD Dissertation, AFIT/DS/ENG/98-10, School of Engineering, Air Force Institute of Technology, Wright-Patterson AFB, OH, May 1998.
56. White, Nathan A. *MMAE Detection of Interference/Jamming and Spoofing in a DGPS-Aided INS*. MS Thesis, AFIT/GE/ENG/96D-21, School of Engineering, Air Force Institute of Technology, Wright-Patterson AFB, OH, December 1996.
57. Young, Brian J. *An Integrated Synthetic Aperture Radar / Global Positioning System / Inertial Navigation System for Target Geolocation Improvement*. MS Thesis, AFIT/GE/ENG/99M-32, School of Engineering, Air Force Institute of Technology, Wright-Patterson AFB, OH, In Progress, March 1999.

58. Zumwalt, Michel P., Maj. Test Pilot Candidate, Edwards AFB, CA. Personal Interview. October 1998.

Vita

Steve Chastain's hometown is Orlando FL. He received a Bachelor of Science degree in Electrical Engineering from Florida Atlantic University. He entered Officer Training School at Lackland AFB TX and received his commission on 22 September 1993. His first Air Force assignment was with the Space-Based Infrared System Program Office at Los Angeles AFB CA. His duties included overseeing the testing and maintenance of the infrared sensors on-board the Defense Support Program early-warning satellites. He then spent a year matrixed to the Aerospace Corporation in the Astrodynamics Department doing studies on the atmospheric effects in low earth orbit and designing a orbital simulator for *molniya* (highly eccentric) orbits. In August 1997, he assigned to attend the Guidance & Control program at the Air Force Institute of Technology at Wright-Patterson AFB OH, specializing in stochastic modeling and navigation systems. After graduating on 23 March 1999, his follow-on assignment was to the 746th Test Squadron at Holloman AFB NM.

| REPORT DOCUMENTATION PAGE | | | Form Approved OMB No. 0704-0188 | |
|---|---|--|---|---|
| Public reporting burden for this collection of information is estimated to average 1 hour per response, including the time for reviewing instructions, searching existing data sources, gathering and maintaining the data needed, and completing and reviewing the collection of information. Send comments regarding this burden estimate or any other aspect of this collection of information, including suggestions for reducing this burden, to Washington Headquarters Services, Directorate for Information Operations and Reports, 1215 Jefferson Davis Highway, Suite 1204, Arlington, VA 22202-4302, and to the Office of Management and Budget, Paperwork Reduction Project (0704-0188), Washington, DC 20503. | | | | |
| 1. AGENCY USE ONLY (Leave blank) | | 2. REPORT DATE March 1999 | | 3. REPORT TYPE AND DATES COVERED MS Thesis |
| 4. TITLE AND SUBTITLE Integrated GPS/INS Precision Approach Landing with M3AE Interference Avoidance | | | 5. FUNDING NUMBERS | |
| 6. AUTHOR(S) Stephan H. Chastain | | | | |
| 7. PERFORMING ORGANIZATION NAME(S) AND ADDRESS(ES) Air Force Institute of Technology 2950 P Street Wright-Patterson AFB OH 45433-7765 | | | 8. PERFORMING ORGANIZATION REPORT NUMBER AFIT/GE/ENG/99M-03 | |
| 9. SPONSORING/MONITORING AGENCY NAME(S) AND ADDRESS(ES) Juan Vasquez, Cpt, USAF AFRL/SNAR Bldg 620 2241 Avionics Circle Wright-Patterson AFB OH 45433-7321 937-255-5668 x4014 | | | 10. SPONSORING/MONITORING AGENCY REPORT NUMBER | |
| 11. SUPPLEMENTARY NOTES | | | | |
| 12a. DISTRIBUTION AVAILABILITY STATEMENT Distribution Unlimited | | | 12b. DISTRIBUTION CODE | |
| 13. ABSTRACT (Maximum 200 words) Several past research efforts have developed methods to take advantage of Global Positioning System (GPS) positioning and apply it to a precision landing system (PLS). There have been proposals to phase out the current Instrument Landing System (ILS) in favor of a more cost-efficient and effective system. Accomplishments have been made in detailing a system implementing an INS aided with differential GPS, a GPS pseudolite, and a radar altimeter to handle the critical PLS requirements. This research applies the newly developed Modified Multiple Model Adaptive Estimation (M3AE) architecture in an attempt to enhance the performance of a PLS in an environment involving GPS interference. The M3AE uses Multiple Model Adaptive Estimation (MMAE) and Kalman filtering techniques to estimate the levels of interference and the navigation performance of the aircraft simultaneously. In addition, in the original development of M3AE, the truth and filter model used were of the same order. This research serves as a demonstration of M3AE applied to system where the truth model is of a higher order than the filter model. | | | | |
| 14. SUBJECT TERMS Precision Approach Landing; Inertial Navigation Systems (INS); Global Positioning System (GPS); Kalman Filtering; Adaptive Filtering | | | 15. NUMBER OF PAGES 146 | |
| | | | 16. PRICE CODE | |
| 17. SECURITY CLASSIFICATION OF REPORT Unclassified | 18. SECURITY CLASSIFICATION OF THIS PAGE Unclassified | 19. SECURITY CLASSIFICATION OF ABSTRACT Unclassified | 20. LIMITATION OF ABSTRACT UL | |